N° d'ordre...../FT/UMBB/2023

People's Democratic Republic of Algeria
Ministry of Higher Education and Scientific Research
University M'Hamed Bougara of Boumerdes

Faculty of Technology

PhD DISSERTATION

PRESENTED BY:

Selma YAHIA

In Partial Fulfilment Of The Requirements For The Degree Of

DOCTORATE

Field: TELECOMMUNICATIONS
Option: Networks and Telecommunications

Improvement of VLC Technology and Deployment in the Context of Smart City

JURY MEMBERS:

Pr. Fayçal RAHMOUNE	Professor	UMBB	President
Dr. Yassine MERAIHI	MCA	UMBB	Supervisor
Dr. Leila GRAINI	MCA	8 mai 1945-Guelma University	Examiner
Dr. Khaled HARRAR	MCA	UMBB	Examiner
Dr. Noureddine MESSAOUDI	MCA	UMBB	Examiner
Pr. Dalila ACHELI	Professor	UMBB	Invited

Academic Year: 2022/2023

ACKNOWLEDGEMENTS

I would like to express my deepest gratitude to my thesis advisor, Dr Yassine MERAIHI, for his guidance, support, and encouragement throughout the entire process of this thesis. His invaluable insights and expertise have been instrumental in shaping the direction and outcome of my research. I am deeply grateful for his time and dedication, and for his constructive comments and suggestions, which helped me to improve the quality of my work. The work of this dissertation would not have been possible without his support.

I would also like to express my gratitude to Dr. Hossien who has always supported me during my years. I would like to thank him for his invaluable encouragement, support, advice, ideas and suggestions during this PhD experience. The work of this dissertation would not have been possible without his support and advice. I will never forget the support and guidance he gave me, which provided me with many opportunities to learn and grow as a researcher.

I would like to extend my heartfelt gratitude to Professor Dalila Acheli, who has played a critical role as the head of the doctoral formation program. Her unwavering support, guidance, and encouragement have been invaluable to me during my PhD journey, and I am deeply grateful for all that she has done.

I would also like to thank the members of my thesis committee, Pr. Fayçal RAHMOUNE, Dr. Leila GRAINI, Dr. Khaled HARRAR, and Pr. Dalila ACHELI for their time, constructive feedback, and valuable suggestions. Their contributions have greatly enhanced the quality of my thesis.

I would like to express my heartfelt appreciation to my parents for their unwavering love and support. Their love and encouragement has been a constant source of motivation and inspiration. This thesis would not have been possible without their constant encouragement and understanding. I would like to thank my brothers, Salah Edine and Mohcen, and my sisters, Salha and Deaa for their continuous support.

Lastly, I would also like to extend my sincere thanks to my colleagues and friends (Salima, Raouia, and Maha) for their support and encouragement throughout my studies.

I dedicate this thesis to my parents, who have always been my source of inspiration and motivation.

ABSTRACT

The demand for wireless communication systems has increased dramatically due to their ability to enable the exchange of information between various devices, offering the potential to enhance safety, manage traffic and improve convenience. Extensive research and standardization efforts in wireless communications have focused on radio frequency (RF) technologies. Nevertheless, RF technologies are susceptible to high levels of interference and channel congestion in heavily populated areas, which can adversely affect the performance of delay-sensitive applications. To mitigate such problems, researchers from academia and industry started to explore and develop new communication technologies. Visible light communication (VLC) is considered one of the promising technologies. VLC uses the visible part of the electromagnetic spectrum and offers an alternative solution to the limitations posed by RF communications.

The data transmission through VLC technology depends on the ability to modulate the intensity of the Light-Emitting-Diode (LED), enabling the dual use of LED for illumination and communication purposes. This results in a highly efficient, low-power, and low-latency communication solution, that is immune to interference from other communication technologies. VLC deploys the existing lighting infrastructures, which offers an innovative way to transmit data in widespread areas and for various applications such as indoor communication, vehicular communications, and smart cities. VLC is still new in some applications and requires extensive efforts to cope with several challenges in different aspects, including system and channel modeling, transceiver modeling and design, optimization of various system parameters, and performance analysis. This thesis provides a comprehensive study of different research topics in VLC technology. The objective is to shed light on the new applications of VLC systems, illustrating the challenges that limit the system performance and introducing novel solutions to improve such performance.

In the first part of this dissertation, we provide a comprehensive review of VLC technology, illustrating the existing research efforts on different prospects. That starts from the system and channel modeling and reaches the performance analysis and system implemen-

tation. Since channel modeling is critical for system design and performance estimation, we then focus on that and present a comprehensive study of the traditional and advanced channel modeling approaches for VLC systems. We illustrate the advantages and the capabilities of utilizing the advanced non-sequential ray tracing channel modeling approach. These include the ability to incorporate and model practical and commercial light sources with their different radiation patterns and the consideration of many reflections to provide more accurate results. Therefore, we adopt this channel modeling approach, which forms the foundation of our research, to model and evaluates the performance of different VLC applications and scenarios in the other parts of the thesis.

Our work focuses primarily on improving the performance and efficiency of VLC systems in indoor and outdoor applications. In the second part of this thesis, we consider the outdoor scenarios aiming to improve the system performance through novel receiver designs, including imaging and non-imaging receivers. Utilizing the proposed structure, we investigate the performance of both vehicle-to-vehicle (V2V) and vehicle-to-infrastructure (V2I) VLC applications.

The third part of this thesis focuses on indoor applications where a novel resource allocation scheme is proposed to enhance the performance of Massive Optical internet-of-things (IoT) systems. The proposed technique depends on an improved version of the Aquila Optimization (AO) algorithm, which integrates chaotic maps, Quasi-Opposition-Based Learning (QOBL) concept, Fitness-distance balance (FDB) selection methods, and cosine functions into the original AO algorithm to enhance its performance.

Extensive simulations and analyses are conducted to compare the system performance using the proposed designs, algorithms, and schemes with the existing literature work. The results demonstrate the effectiveness of our proposed work in improving the performance and efficiency of the VLC system in indoor and outdoor scenarios. To conclude, this dissertation provides a comprehensive study of VLC technology, offering new insights into system and channel modeling, receiver design, transmission schemes, and system optimization, paving the way for future research extensions in this area.

Keywords: Visible Light Communication (VLC), Indoor VLC, Vehicular VLC, Ray-Tracing, Channel modeling, Optimization.

RÉSUMÉ

La demande de systèmes de communication sans fil a considérablement augmenté en raison de leur capacité à permettre l'échange d'informations entre différents dispositifs, offrant ainsi le potentiel d'améliorer la sécurité, de gérer le trafic et d'améliorer la commodité. Des recherches approfondies et des efforts de normalisation en matière de communications sans fil ont porté sur les technologies radiofréquences (RF). Néanmoins, les technologies RF sont susceptibles de subir des niveaux élevés d'interférences et de congestion de canaux dans les zones fortement peuplées, ce qui peut affecter négativement les performances des applications sensibles à la latence. Pour atténuer de tels problèmes, les chercheurs du milieu universitaire et de l'industrie ont commencé à explorer et à développer de nouvelles technologies de communication. La communication par lumière visible (VLC) est considérée comme l'une des technologies prometteuses. La VLC utilise la partie visible du spectre électromagnétique et offre une solution alternative aux limites posées par les communications RF. La transmission de données par la technologie VLC dépend de la capacité à moduler l'intensité de la diode électroluminescente (LED), permettant l'utilisation double de la LED à des fins d'éclairage et de communication. Cela résulte en une solution de communication hautement efficace, à faible consommation d'énergie et à faible latence, qui est immunisée contre les interférences des autres technologies de communication. La VLC déploie les infrastructures d'éclairage existantes, ce qui offre une façon innovante de transmettre des données dans des zones étendues et pour diverses applications telles que la communication intérieure, les communications véhiculaires et les villes intelligentes. La VLC est encore nouvelle dans certaines applications et nécessite des efforts importants pour faire face à plusieurs défis dans différents aspects, notamment la modélisation des systèmes et des canaux, la modélisation et la conception des émetteurs-récepteurs, l'optimisation de divers paramètres du système et l'analyse des performances. Cette thèse offre une étude complète de différents sujets de recherche en technologie VLC. L'objectif est de mettre en lumière les nouvelles applications des systèmes VLC, d'illustrer les défis qui limitent les performances du système et d'introduire de nouvelles solutions

pour améliorer ces performances.

Dans la première partie de cette thèse, nous fournissons une revue complète de la technologie VLC, illustrant les efforts de recherche existants sur différents aspects. Cela commence par la modélisation du système et du canal et atteint l'analyse des performances et la mise en oeuvre du système. Étant donné que la modélisation de canal est critique pour la conception du système et l'estimation des performances, nous nous concentrons ensuite sur ce point et présentons une étude complète des approches traditionnelles et avancées de modélisation de canal pour les systèmes VLC. Nous illustrons les avantages et les capacités de l'utilisation de l'approche avancée de modélisation de canal à rayons non séquentiels. Celles-ci incluent la capacité à incorporer et à modéliser des sources de lumière pratiques et commerciales avec leurs différents motifs de rayonnement et la prise en compte de nombreuses réflexions pour fournir des résultats plus précis. Par conséquent, nous adoptons cette approche de modélisation de canal, qui constitue la base de nos recherches, pour modéliser et évaluer les performances de différentes applications et scénarios VLC dans les autres parties de la thèse.

Notre travail se concentre principalement sur l'amélioration des performances et de l'efficacité des systèmes VLC dans les applications intérieures et extérieures. Dans la deuxième partie de cette thèse, nous considérons les scénarios extérieurs visant à améliorer les performances du système grâce à de nouvelles conceptions de récepteurs, y compris des récepteurs d'imagerie et sans imagerie. En utilisant la structure proposée, nous étudions les performances des applications VLC de véhicule à véhicule (V2V) et de véhicule à infrastructure (V2I).

La troisième partie de cette thèse se concentre sur les applications intérieures, où un nouveau schéma d'allocation des ressources est proposé pour améliorer les performances des systèmes massifs d'Internet des objets optiques (IoT). La technique proposée dépend d'une version améliorée de l'algorithme d'optimisation Aquila (AO), qui intègre des cartes chaotiques, le concept d'apprentissage basé sur l'opposition quasi (QOBL), des méthodes de sélection d'équilibre de distance de forme physique (FDB) et des fonctions cosinus dans l'algorithme AO original pour améliorer ses performances.

Des simulations et des analyses approfondies sont menées pour comparer les performances du système à l'aide des conceptions, algorithmes et schémas proposés avec les travaux existants dans la littérature. Les résultats démontrent l'efficacité de notre travail proposé pour améliorer les performances et l'efficacité du système VLC dans les scénarios intérieurs et extérieurs. En conclusion, cette thèse fournit une étude complète de la technologie VLC, offrant de nouvelles perspectives sur la modélisation du système et du canal, la conception de récepteurs, les schémas de transmission et l'optimisation du système, ouvrant la voie à de futures extensions de recherche dans ce domaine.

Mots-clés: Communication par la lumière visible (VLC), VLC intérieure, VLC automobile, Ray-Tracing, Modélisation de canal, Optimisation.

ملخص

زاد الطلب على أنظمة الاتصالات اللاسلكية بشكل كبير بسبب قدرتها على تمكين تبادل المعلومات بين الأجهزة المختلفة ، مما يوفر إمكانية تعزيز السلامة وإدارة حركة المرور وتحسين الراحة. ركزت جهود البحث المكثفة في مجال الاتصالات اللاسلكية على تقنيات التردد اللاسلكي (RF). ومع ذلك ، فإن تقنيات التردد الراديوي عرضة لمستويات عالية من التداخل وازدحام القنوات في المناطق المكتظة بالسكان ، مما قد يؤثر سلبًا على أداء التطبيقات الحساسة للتأخير. للتخفيف من مثل هذه المشاكل ، بدأ باحثون من الأوساط الأكاديمية والصناعية في استكشاف وتطوير تقنيات اتصال جديدة. تعتبر الاتصالات الضوئية المرئية (VLC) من التقنيات الواعدة. يستخدم VLC الجزء المرئي من الطيف الكهرومغناطيسي ويقدم حلاً بديلاً للقيود التي تفرضها اتصالات التردد اللاسلكي.

يعتمد نقل البيانات من خلال تقنية VLC على القدرة على تعديل شدة الصمام الثنائي الباعث للضوء (LED)، مما يتيح الاستخدام المزدوج لمصابيح LED لأغراض الإضاءة والاتصالات. ينتج عن هذا حل اتصالات عالي الكفاءة ومنخفض الطاقة وزمن انتقال منخفض ، وهو محصن ضد التداخل من تقنيات الاتصال الأخرى. تنشر VLC البنى التحتية للإضاءة الحالية ، والتي توفر طريقة مبتكرة لنقل البيانات في مناطق واسعة النطاق وللتطبيقات المختلفة مثل الاتصالات الداخلية واتصالات المركبات والمدن الذكية. لا يزال VLC جديدًا في بعض التطبيقات ويتطلب جهودًا مكثفة للتعامل مع العديد من التحديات في جوانب مختلفة ، بما في ذلك نمذجة النظام والقناة ونمذجة جهاز الإرسال والاستقبال والتصميم وتحسين معلمات النظام المختلفة وتحليل الأداء. تقدم هذه الأطروحة دراسة شاملة لمواضيع البحث المختلفة في تكنولوجيا VLC. الهدف هو إلقاء الضوء على التطبيقات الجديدة لأنظمة VLC ، وتوضيح التحديات التي تحد من أداء النظام وتقديم حلول جديدة لتحسين هذا الأداء.

في الجزء الأول من هذه الرسالة ، نقدم مراجعة شاملة لتقنية VLC ، لتوضيح الجهود البحثية الحالية حول الآفاق المختلفة. يبدأ ذلك من نمذجة النظام والقناة ويصل إلى تحليل الأداء وتنفيذ النظام. نظرًا لأن نمذجة القنوات أمر بالغ الأهمية لتصميم النظام وتقدير الأداء ، فإننا نركز بعد ذلك على ذلك ونقدم دراسة شاملة لأساليب نمذجة القنوات التقليدية والمتقدمة لأنظمة VLC.نوضح مزايا وقدرات استخدام نهج نمذجة قناة تتبع الأشعة غير المتسلسلة المتقدمة. وتشمل هذه القدرة على دمج

ونمذجة مصادر الضوء العملية والتجارية بأنماط إشعاعها المختلفة ومراعاة العديد من الانعكاسات لتقديم نتائج أكثر دقة. لذلك ، نعتمد نهج نمذجة القنوات هذا ، والذي يشكل أساس بحثنا ، لنمذجة وتقييم أداء تطبيقات وسيناريوهات VLC المختلفة في الأجزاء الأخرى من الأطروحة.

يركز عملنا بشكل أساسي على تحسين أداء وكفاءة أنظمة VLC في التطبيقات الداخلية والخارجية. في الجزء الثاني من هذه الرسالة ، نأخذ بعين الاعتبار السيناريوهات الخارجية التي تهدف إلى تحسين أداء النظام من خلال تصميمات مستقبلات جديدة ، بما في ذلك مستقبلات التصوير وغير التصويرية. باستخدام الهيكل المقترح ، نقوم بفحص أداء كل من تطبيقات VLC من مركبة إلى أخرى (V2V) ومن مركبة إلى بنية تحتية (V2I).

يركز الجزء الثالث من هذه الأطروحة على التطبيقات الداخلية حيث تم اقتراح مخطط جديد لتخصيص الموارد لتحسين أداء أنظمة إنترنت الأشياء الضوئية (IoT). تعتمد التقنية المقترحة على نسخة محسّنة من خوارزمية تحسين Aquila (AO) ، والتي تدمج الخرائط الفوضوية ، ومفهوم التعلم شبه المعارض (QOBL)، وطرق اختيار التوازن بين اللياقة والمسافة (FDB)، ووظائف جيب التمام في AO الأصلي خوارزمية لتحسين أدائها.

يتم إجراء عمليات محاكاة وتحليلات واسعة النطاق لمقارنة أداء النظام باستخدام التصاميم والخوارزميات والخطط المقترحة مع الأعمال الأدبية الحالية. توضح النتائج فعالية عملنا المقترح في تحسين أداء وكفاءة نظام VLC في السيناريوهات الداخلية والخارجية. في الختام ، توفر هذه الرسالة دراسة شاملة لتقنية VLC ، وتقدم رؤى جديدة في نمذجة النظام والقناة ، وتصميم المستقبِل ، وخطط الإرسال ، وتحسين النظام ، مما يمهد الطريق لامتدادات بحثية مستقبلية في هذا المجال.

الكلمات المفتاحية : اتصالات الضوء المرئي (VLC)، VLC داخلي ، VLC للسيارات ، تتبع الأشعة ، نمذجة القناة ، التحسين.

CONTENTS

LIST OF FIGURES

LIST OF TABLES

LIST OF ALGORITHMS

ACRONYMS

ADR Angle Diversity Receiver

AO Aquila Optimization

AOR Angle Oriented Receiver

BER Bit Error Rate

CIR Channel Impulse Response

CSK Color Shift Keying

DLoS Direct Line of Sight

FDB Fitness-distance balance

FoV Field of View

IoT Internet of Things

LED Light-Emitting Diodes

Li-Fi Li-Fi Light Fidelity

LoS Line of Sight

NDLoS Non-Direct Line of Sight

NDNLoS Non-Direct Non Line of Sight

NON-LoS Non-Line of Sight

OOK On-Off Keying Modulation

OWC Optical Wireless Communication

PD Photodetector

PER Packet Error Ratio

QOBL Quasi-OppositionBased Learningn

RF Radio Frequency

Rx Receiver

SNR Signal to Noise Ratio

Tx Transmitter

VLC Visible Light Communication

VPPM Variable Pulse Position Modulation

GENERAL INTRODUCTION

Wireless communication technologies have become an integral part of modern society, with a wide range of applications in areas such as telecommunications, transportation, and healthcare [1]. The widespread adoption of wireless communication has brought many benefits, including improved access to information, increased productivity, and greater convenience [2]. The majority of current wireless communication systems rely on radio frequency (RF) technologies to transmit information. However, the need for wireless data is growing, driven by technological advances and the increasing number of wireless broadband services such as mobile video phones, video conferencing, and high-speed Internet access. According to the International Telecommunication Union (ITU), the number of Internet users worldwide has increased dramatically, with more than 4.5 billion people using the Internet in 2019 [3]. As a result, RF spectrum is becoming increasingly crowded and will not be sufficient for the future of wireless communications. The need for additional spectrum is therefore becoming more pressing. One of the proposed solutions is the use of optical wireless communication (OWC).

In recent years, there has been a growing interest from academia and industry in optical wireless communication (OWC) technologies. It is based on the use of light waves to transmit data over the air, instead of using radio waves like traditional wireless communication systems [4]. OWC systems use visible or infrared light to transmit data, and can provide several advantages over radio-based systems, such as higher data rates, improved security, and reduced interference. Despite these benefits, optical wireless communication has a wide range of potential applications, including satellite communication, high-speed data transfer, mobile communication, and the Internet of Things (IoT).

Visible light communication is a part of Optical wireless communication which uses light in the unlicensed visible light spectrum (between 380 THz and 790 THz) to transmit data [5]. It allows data transmission by modulating the information on the intensity of light-emitting diodes (LEDs), achieving dual functionality, i.e. lighting and data communication [6, 7]. These LEDs have attractive features over conventional light sources

(i.e., incandescent bulbs and fluorescent lamps), such as energy efficiency, long lifespan, durability, and fast switching [8, 9]. VLC has many advantages over traditional wireless communication methods, such as low power consumption, high security, immunity to electromagnetic interference, as well as the ability to transmit data in environments where radio frequency communication may be hindered. It can also be integrated with existing lighting infrastructure, making them a cost-effective solution for many applications. VLC has the potential to complement or even replace existing RF communication technologies in a variety of applications, such as: indoor communications [10], automotive and aerospace [11, 12], healthcare [13], and underwater communications [14].

This thesis focuses on several fundamental research areas in the visible light communications. For our contribution, we focused on two main applications: vehicular and indoor applications. Concerning the vehicular applications two contributions have been proposed. The first one is based on the modeling of a realistic wireless optical channel using the non-sequential ray tracing approach. The second is based on the application of different receiver structures to improve the performance of V2V VLC and V2I VLC systems. Regarding the indoor applications, in our contribution we presented an improvement version of Aquila algorithm to solve the resource allocation problem in an indoor VLC system.

The structure of this manuscript is organized into five chapters as follows:

In Chapter 1, we present a general overview of visible light communication systems. Then, we describe the architecture of the end-to-end VLC transmission system, the modulation schemes, and the advantages and disadvantages of this technology. Finally, we present the various applications of this technology.

In Chapter 2, we present the theoretical foundations of the VLC channel. We first describe the different links that can exist between the transmitter and the receiver. Then, we describe the different existing noise sources in a VLC system. After that, the different characteristics of the VLC channel is presented. Finally, we classified the different channel models existing in the literature according to the environment, and each existing approach is then defined.

In Chapter 3, we present the first contribution of this thesis which is the modeling of a realistic wireless optical channel in a V2V and V2I-VLC system. This chapter provides a comprehensive analysis of the V2V and V2I VLC systems using an angle diversity receiver and provides valuable insights into the performance of these systems, which can be useful in the design and implementation of VLC-based communication systems. The first part of the chapter discusses the V2V VLC system and uses the ray tracing channel modeling methodology to model the wireless optical channel. The performance of the V2V system is evaluated in terms of maximum achievable distance, capacity, and packet error ratio. The impact of various parameters such as receiver FoV, receiver aperture diameter, and modulation bandwidth is also investigated. The second part of Chapter 3 focuses on the

V2I VLC system, where the source cars transmit signals to the traffic light using their headlights. The performance of this system is evaluated in terms of capacity, and the impact of lateral offsets and elevation angle is also studied.

In Chapter 4, we present our second contribution, which is the application of an imaging receiver with different lens combinations to improve the performance of V2V VLC systems. We perform a realistic channel modeling study based on the non-sequential ray-tracing approach in OpticStudio®. We propose a novel optical lens combination design to correct more optical aberrations and investigate the impact of different system parameters on the overall performance of the V2V system.

In Chapter 5, we present our third contribution, which is the proposal of a new optimization scheme to solve the resource allocation problem in indoor Multi-user IoT-VLC systems. The proposed scheme is based on the integration of chaotic maps, QOBL mechanism, FDB selection method, and cosine function into the original AO algorithm.

Finally, we present the conclusion of the thesis and outline the future directions for research in the field of visible light communication.

CHAPTER 1

AN OVERVIEW OF VISIBLE LIGHT COMMUNICATIONS

1.1 Introduction

Visible Light Communication (VLC) is a form of data communication that uses visible light in the electromagnetic spectrum as a medium to transmit information. It involves modulating light emitted by LEDs or other light sources to carry data signals that can be received by a photodetector. It provides several advantages compared to traditional radio frequency (RF) communication, including higher security and privacy, lower interference, and the ability to operate in RF-restricted environments, such as aircraft cabins and medical facilities. Additionally, VLC can be integrated with existing lighting infrastructure, making it a cost-effective solution.

VLC is used in a wide range of applications, including indoor lighting, mobile communication and the Internet of Things (IoT). Its ability to provide secure, interference-free communication, combined with its cost-effectiveness, makes it an increasingly popular technology for many industries and environments.

In this chapter, we provide an overview of visible light communication (VLC), including its history, definition, and underlying principle. We also delve into the specific aspects of VLC by highlighting its benefits, limitations, and potential applications.

1.2 Brief Historical Overview of VLC

Light has always been part of the elements used by humans to communicate with each other. Since ancient times, light has been used as a means of communication in many cultures around the world, whether in the use of beacon fires or smoke signal. Thus, a functional communication systems based on visible light were recorded thousands of years ago. The Historian Polybius developed a system of information exchange using torches. To do this, an agreement was established between the sender and the receiver,

and the alphabet was represented by a set of 5 torches [15]. At the end of the 18^{th} century, semaphore telegraph was invented by Claude Chappe [16] and widely used Sweden, France or the United Kingdom. Its principle is to transfer information with visible signals using pivoting shutters and towers. Basically, this mechanism consisted of two side rods (i.e., indicators) attached to a long rod (i.e., regulator). Thus, different symbols can be created by rotating the side rods. the optical telegraphs were mounted in towers at a distance of 10 to 15 kilometers. Based on this structure and efficient coding, it was able to create up to 98 different combinations, visible for miles around.

At the end of the 19^{th} century, Alexander Graham Bell built the photo-phone using a vibrating mirror and a parabolic receiver to modulate and transmit voice signals over hundreds of meters. Specifically, the sunlight reflected in a mirror reached the surface of a thin glass, which vibrated in response to the person's voice. The light was then relayed by a second lens to the receiver, in which the light was reflected in a selenium cell via a parabolic mirror. This technology was followed in the 1960's with the invention of light amplification systems by stimulated emission of radiation (laser). Optical media communication has then gained attention in the 1970s. At that time, research has demonstrated the feasibility of wireless optical communication (in this case, infrared) in an indoor environment.

In the early 2000s, LED bulbs were first considered for experiments involving VLC. Tanaka et al. [17] used a white LED bulb for lighting and communication in an indoor environment, achieving a communication data rate of 400 Mbps. After this work, other researchers brought great innovations, such as new modulation techniques and new LED bulb technologies. For instance, in 2004, the first demonstrations of high-speed communication using LEDs were carried out in Japan using photodiodes. Thanks to the multiplication of cell phones equipped with cameras, these devices could be used as VLC receivers. Researchers have begun to use liquid crystal displays (LCDs) and other display elements as transmitters. A milestone in the history of visible light communication was reached in 2011, when Harald Haas demonstrated Li-Fi (Light Fidelity) for the first time at a TED talk. Notably, the number of studies with the keyword "Visible Light Communication" on the IEEE Xplore platform is increasing exponentially over the years.

1.3 Advantages and Drawbacks

1.3.1 Advantages

VLC communications offer several significant advantages, including:

Wide Bandwidth

The spectrum of radio frequency is limited, from 3 kHz to 300 GHz, while the spectrum of visible light is at least 10000 times larger, which is from 430 THz to 790 THz. Unlike

RF, it extends over several THz and can be used without restriction. This advantage addresses the growing problem of RF spectrum congestion, which increasingly limits the deployment of new communications devices and networks.

Unrestricted Technology

Another point is that the optical technology is robust against electromagnetic interference. The VLC technology is suitable for communications in environments with immunity to electromagnetic interference, such as hospitals, nuclear power plants and aircraft.

Security

On the other hand, it offers a high degree of security, as the optical rays do not pass through walls and obstacles. They are therefore generally confined to their environment and interception of data is thus impossible from the outside. This is a benefit that improves information security and ensures more secure communications links.

Low implementation costs and energy savings

VLC utilizes the visible light spectrum, which operates in an unlicensed portion of the electromagnetic spectrum, unlike Radio Frequency (RF) communication that operates in a regulated band and requires licensing fees. This advantage leads to a significant reduction in implementation costs for VLC. A second benefit that helps VLC reduce the cost of implementation is its ubiquitous nature. It reduces the need for additional hardware, as it utilizes existing lighting infrastructure, such as LED lights, to transmit data. This eliminates the need for extra devices and cables, reducing the overall cost of implementation. Additionally, the widespread availability of LED lights makes it easier for organizations to implement VLC technology, as there is no need for specialized hardware that may be difficult to obtain. This makes VLC a convenient and accessible solution for organizations looking to implement a new technology. Furthermore, as VLC technology is based on existing infrastructure, it is more likely to be compatible with other existing systems, reducing the need for expensive modifications and ensuring seamless integration. These benefits of VLC's ubiquitous nature make it an attractive and cost-effective solution for organizations looking to implement a new technology.

On the other hand, the use of LED lights for both lighting and data transmission, eliminating the need for additional power for communication. This reduces energy consumption and CO2 emissions compared to traditional lighting sources, making VLC an environmentally friendly technology solution.

Safe technology

In contrast, radio frequency and microwave devices can emit harmful radiation, LED lighting does not emit harmful radiation, making it a safe technology solution for both the environment and users. By using LED lighting as the foundation for VLC technology, organizations can implement a new technology that is safe and does not pose a risk to the environment or human health.

1.3.2 Drawbacks

Despite its inherent advantages over other communication systems, VLC still faces many challenges that need to be addressed.

Line of sight condition

Line of Sight (LoS) communication has the potential to maximize energy efficiency and minimize multipath distortion by providing a direct, clear path for signals to travel between the transmitter and receiver. The mandatory LoS condition can also enhance communication security by limiting interference from other receivers and reducing the risk of unauthorized interception. However, visible light signals can be reflected but do not penetrate most objects, which can limit coverage. Also, an object between the transmitter and receiver can block communication unless an alternative route is available. These limitations should be considered when deciding on the appropriate communication method for a given application.

Limited transmission range

One of the challenges facing Visible Light Communication technology is its limited transmission range, which is often shorter than that of Radio Frequency (RF) communication. However, there are various efforts underway to increase the transmission range of VLC, such as increasing the transmission power or using a more directional light beam on the transmitter side, or using narrow field-of-view receivers, optical lenses, or filtering techniques on the receiver side. These methods can help to overcome the limitations of VLC and make it a more viable option for a wider range of applications.

Susceptibility to interference

Interference is another drawback of Visible Light Communication (VLC) technology. VLC signals can be susceptible to interference from other lighting devices such as incandescent or fluorescent light sources, which can produce low-frequency noise that can be eliminated using a high-pass filter. Sunlight is another important disturbance factor in outdoor applications, as it can produce unmodulated light that introduces a strong DC component

that can be eliminated using capacitive DC filters. However, high intensity optical noise can still saturate the receiver and prevent communication. These challenges need to be taken into consideration when deploying VLC systems, and appropriate mitigation strategies must be employed to ensure reliable and robust communication.

1.4 Architecture of Visible Light Communication System

The architecture of the end-to-end VLC transmission system is illustrated in Figure 1.1. It consists of three main parts which are the transmitter (TX) front-end, the receiver (RX) front-end, and the propagation VLC channel. The characteristics of these parts have a significant impact on the VLC system. In the following, we explain each individual part highlighting its inherent components and main functions.

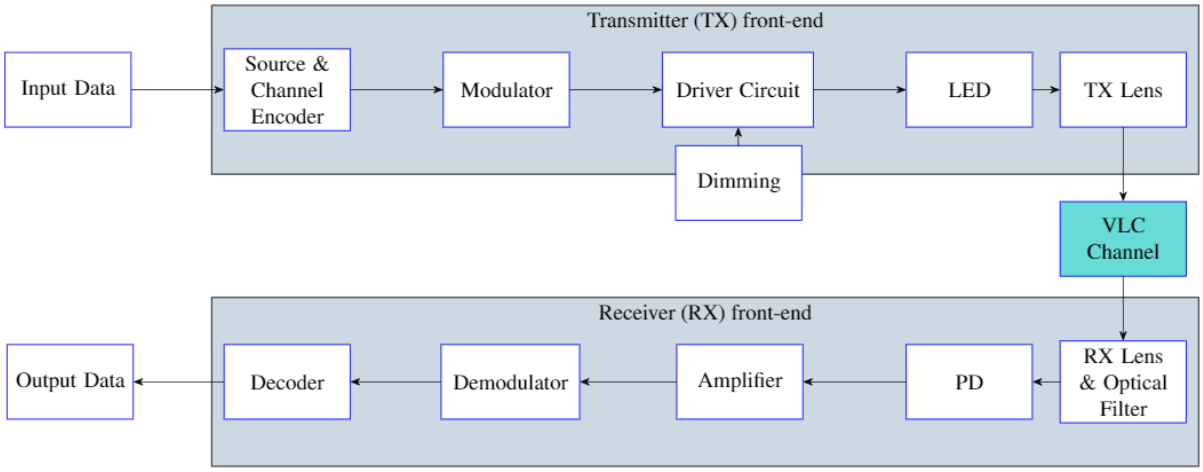

Figure 1.1: VLC system model

1.4.1 VLC Transmitter (TX) Front-end

In VLC systems, the TX front-end is the first critical part which has different components with different functions. As shown in Figure 1.1, the source analog data is firstly passed to the "Source Encoder" to be converted into digital format, i.e., stream of bits 0 and 1. In order to fix part of the errors introduced due to the channel dispersion, a redundancy in data bits is required which can be achieved by the "Channel Encoder" element. There are various encoding techniques used in VLC systems with diverse advantages (See [18] and references therein).

The encoded data is then used to modulate the intensity of the optical signal emitted from the light source with the help of the "Modulator" element. Generally, the simplest used modulation technique in the VLC system is the intensity modulation while other

modulation schemes are also possible [8]. In order to drive the current flowing through the LED and hence control its brightness, the LED "Driver Circuit" is utilized [19].

Once the electrical current flows through a light source, it generates an optical power in the form of light. Generally, LEDs are the most common light sources used in VLC systems. This is due to its inherent advantages comparing with conventional light sources such as low power consumption, long lifetime, cost-effectiveness, and fast switching.

There are four main types of LEDs with different optical characteristics which are suitable in VLC systems [20]. The first one is the Phosphor Converted LED (pc-LED) which is widely used providing low complexity and low-cost [21]. The drawback of this LED type is the limited band due to the slow phosphorus response. The second type is the Multi-Chip LED which consists of some chips to emit different light colors producing the white light [22]. Using the intensity of each chip, such LED type has the ability to control the emitted colors. The third type is the Organic LED (OLED) which consists of a group of thin organic films between the two conductors. It is commonly used in displays of smartphones and is able to construct transparent and flexible devices but with less data rates [7]. The final LED type is the ţ-LED which is higher speed comparing with the OLEDs and can be also coupled in display panels. [21, 20].

1.4.2 VLC Channel

The radiated optical signal from the LED, acting as a wireless transmitter, propagates through the optical channel where the light signal is influenced by many factors such as attenuation, interference [23], and noise [24]. It should be further noted that through the channel, the light rays can be reflected, refracted, or scattered into sub-rays. At the end, the resultant VLC signal is the sum of two main components, i.e., Line-of-Sight (LOS) and non-LOS components. In the LOS channel, the emitted signal from the LED retches the RX front-end directly without touching any objects in between. In this case, the main parameters that attenuate the transmitted signal are the propagation distance and the weather conditions (i.e., in case of outdoor VLC channel). On contrast, in the NLOS channel, the emitted signal reaches the RX after reflecting/scattering from the obstacles in the channel medium [25, 26].

1.4.3 VLC Receiver (RX) Front-end

A complete RX front-end system consists of different components including the optical filter, concentrator (RX lens), photodiode (PD), amplifier, demodulator, and decoder. As indicated in Figure 1.1, the received light after propagation through the channel is concentrated on the photodiode via an optical concentrator in order to capture the maximum amount of light required for the conversion. Then, the rays passed through an optical filter to restrict the background radiation due to the sunlight and the artificial light sources.

After that, the PD generates an electrical current proportional to the incident optical light [27] which is then amplified using trans-impedance amplifiers and processed through the demodulation and decoder stages to get the final output (i.e., information data).

1.5 Modulation Schemes for VLC Systems

There are several modulation techniques associated with wireless optical communications. In the context of VLC, the selection of a particular modulation is made according to different criteria:

- **Flickering:** Changes in the brightness of the modulated light must be made in such a way as not to cause fluctuations perceptible to humans. According to IEEE 802.15.7, switching must be done at a rate faster than 200 Hz to avoid harmful effects [28].
- **Dimming:** Different activities require different illuminances, such as 30-100 lux required for normal visual activities in public places. There is a non-linear relationship between measured light and perceived light, their relationship is given by the following equation

$$\text{Perceived Light } (\%) = 100 \times \sqrt{\frac{\text{Measured Light } (\%)}{100}} \tag{1.1}$$

In the first IEEE 802.15.7 standard [29], different types of modulations are proposed: OOK (On-Off Keying) modulation, VPPM (Variable Pulse Position Modulation) and CSK (Color Shift Keying) modulation.

OOK Modulation

On-Off Keying (OOK) is a binary modulation technique that is simple and widely used in the field of communications, especially for Intensity Modulation with Direct Detection (IM/DD) systems. As described (see Figure 1.2 [30]), it consists of only two symbols (0 or 1), each with a fixed duration T (symbol time). Symbol 0 corresponds to the absence of optical emission, while symbol 1 corresponds to the emission of an optical signal at power $2P_t$ during the same time. However, OOK can be very sensitive to flicker phenomena, as an extended sequence of '0' can be lost if the symbols are not homogeneous, or if the source is switched off for a short period of time. To overcome this issue, the IEEE 802.15.7 standard recommends the use of Manchester coding instead of Non-Return-to-Zero (NRZ) coding, which ensures that the period of the positive pulses is the same as the period of the negative pulses, but at the cost of doubling the bandwidth required for the

transmission. These trade-offs must be considered when choosing a modulation technique for a specific application.

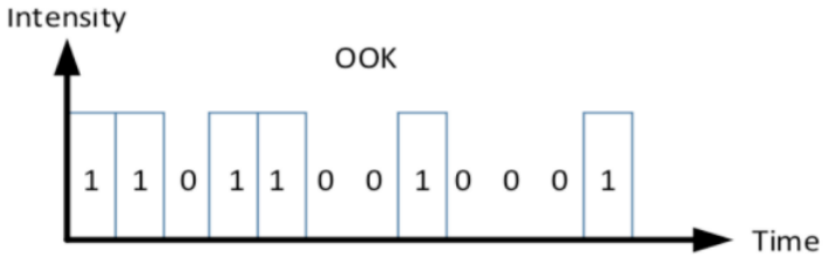

Figure 1.2: OOK modulation scheme

VPPM Modulation

VPPM (Variable Pulse Position Modulation) is a variant of Pulse Position Modulation (PPM) that has been specifically developed for Visible Light Communication (VLC). In PPM modulation, the information is represented by the position of the pulse in time. VPPM extends this by also introducing the variation of pulse width (PWM), depending on the level of light intensity (see Figure 1.3 [31]).

By combining the position of the pulse with the pulse width modulation, VPPM eliminates the flickering problems associated with traditional PPM, as long sequences of '0' symbols are removed, and the PWM technique allows for control of the light intensity [31]. This makes VPPM a promising solution for VLC systems that require higher data rates and improved immunity to interference.

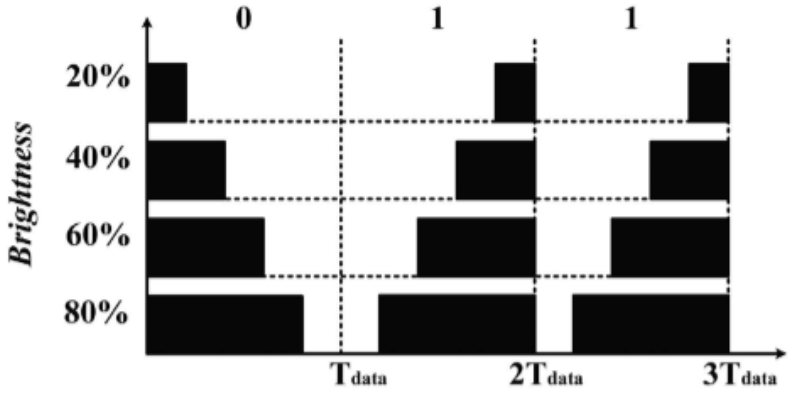

Figure 1.3: VPPM modulation scheme

CSK Modulation

Color-Shift Keying modulation was proposed in the IEEE 802.15.7 standard to improve the data rate which was low in other types of modulation. The switching capability slows

down by producing white light using yellow phosphor and blue LEDs. Therefore, another way to produce white light is to use three separate LEDs, green, blue and red. The CSK modulation depends on the chromaticity diagram of the colorimetric space. Contrary to the other modulations, the symbols are selected so that the light emission remains constant whereas the various chromatic components associated with each color vary [32]. This modulation maps all the colors perceptible to the eye on two parameters of chromaticity such as x and y. Figure 1.4 ([32]) illustrates the seven bands of wavelength visible by the eye presented in a table with their centers represented on the diagram. However, it is important to note that the color shift must be noticeable to the human eye in order to be accurately decoded by the receiver. In addition, the accuracy of the transmission can be impacted by ambient lighting conditions, which can affect the perceived chromaticity of the light source.

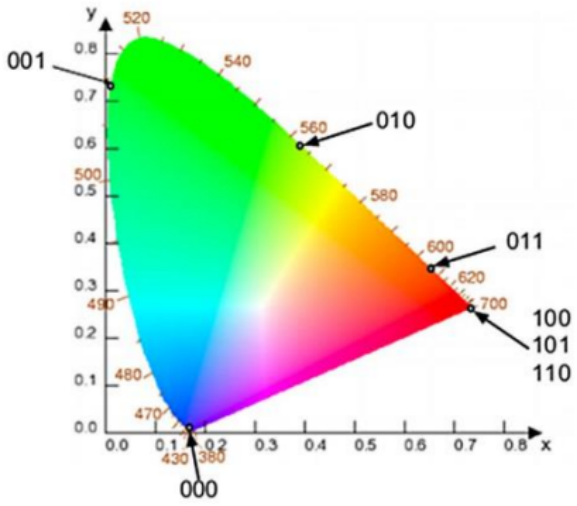

Band (nm)	Code	Center (nm)	(x, y)
380–478	000	429	(0.169, 0.007)
478–540	001	509	(0.011, 0.733)
540–588	010	564	(0.402, 0.597)
588–633	011	611	(0.669, 0.331)
633–679	100	656	(0.729, 0.271)
679–726	101	703	(0.734, 0.265)
726–780	110	753	(0.734, 0.265)

Figure 1.4: CSK modulation scheme

1.6 Applications of Visible Light Communication

Visible Light Communication technology is versatile and has a range of applications. In some cases, VLC is the preferred solution, while in others, it can be used in conjunc-

tion with radio frequency (RF) communications. The following are some of the notable applications that are being explored for VLC.

1.6.1 Indoor VLC Systems

Li-Fi

One of the most important applications envisioned for VLC is the provision of Light-Fidelity (i.e., optical Wi-Fi), proposed by Herald Haas in 2011 [33]. Li-Fi offers a networked indoor system with bidirectional support for point-to-point (P2P) and multi-point-to-point (MP2P) communications (see Figure 1.5, [34]). It also offers the possibility of multiple access points and the formation of wireless networks between them, allowing the creation of atto LiFi cells. These atto cells provide seamless transfer (i.e., handover) and full mobility to users. Li-Fi can achieves a speed of up to 10 Gbps, which is 250 times faster than the speed of ultra-fast broadband [28].

Figure 1.5: Li-Fi application

Indoor localization

In addition to Li-Fi, VLC can provide very efficient indoor location by determining the received signal strength or time of flight. In this kind of applications, VLC is particularly useful, as traditional GPS does not work inside buildings. The classical methods of triangulation, trilateration or fingerprinting associated with VLCs currently make it possible to obtain location accuracies of the order of a centimeter, whereas for example we are around a meter in Wi-Fi [35]. The use of light sources as signal emitters allows for better signal tracking and improved performance. The availability of continuous lighting sources also makes it easier to establish a signal link between different parts of the system (see Figure 1.6 [36]).

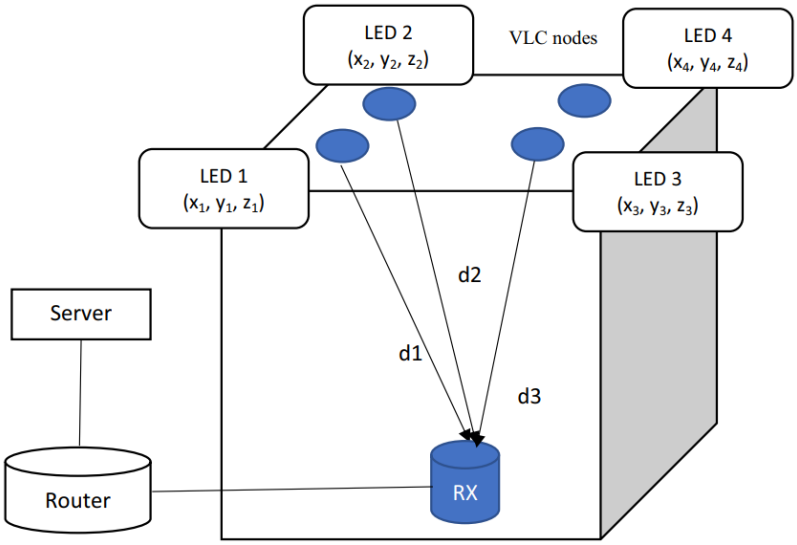

Figure 1.6: VLC indoor positioning system

The creation of intelligent places

Additionally, VLC technology can also be used in smart museum environments to provide geolocated information to visitors through indoor light. This enables visitors to receive information about exhibitions on their smartphones or tablets, enhancing the overall museum experience. The use of VLC in a museum is illustrated in figure 1.7 [34].

Figure 1.7: Illustration of VLC installed at museum

Interference zone

Visible light communication is an ideal solution for providing wireless communications in restricted areas where RF signals are not allowed. Such areas include hospitals, airplanes,

and hazardous environments with the risk of explosions such as mines, chemical plants, or oil platforms. VLC is also suitable for areas where RF signals can interfere with delicate equipment, such as scientific research labs or control rooms for critical infrastructure. Its nature of not emitting harmful electromagnetic waves makes VLC a secure and reliable alternative for communication, ensuring the safety of both people and equipment.

Figure 1.8: Application of VLC in hospital and airplane

1.6.2 Outdoor VLC systems

Intelligent Transportation Systems

Intelligent Transportation System (ITS) is one particular area where VLC could be very useful. Theses systems can take advantage of the LED-equipped lighting modules (i.e, traffic lights, headlamps, taillight, rear light) to establish secure and robust communication. Such arrangements offers a great opportunity to create a connected VLC network that facilitates communication between vehicles (V2V) and infrastructure (V2I) (see Figure 1.9 [37]. These systems create a connected VLC network that offers numerous benefits, including reducing collisions, alerting drivers of traffic lights and speed violations, and warning of roadwork and other hazards. Examples of practical applications of this technology include a system that provides the driver with the optimal speed to pass between two cars, as well as a system that can warn of work and road repair areas or the risk of a sudden slowdown or vehicle breakdown.

Underwater communication

In the underwater environment, radio frequency communication is not effective due to the good conductivity of sea water, which does not allow RF waves to propagate well. In such scenarios, visible light communication can be used to provide short-range communication between divers and with a base. Tethered Remotely Operated Vehicle (UTROV) is an application of VLC in underwater communication [28]. The various activities that can be performed using UTROV include ocean observation, maintenance, and vessel deployment

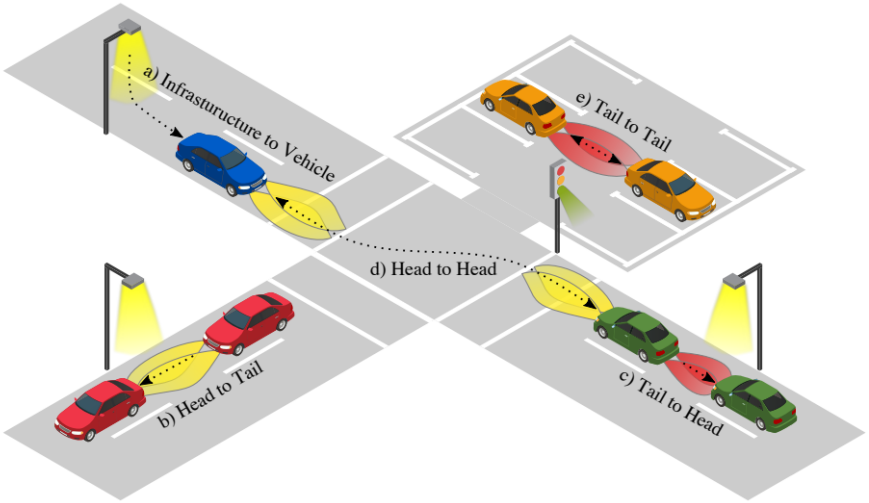

Figure 1.9: Vehicular VLC communication

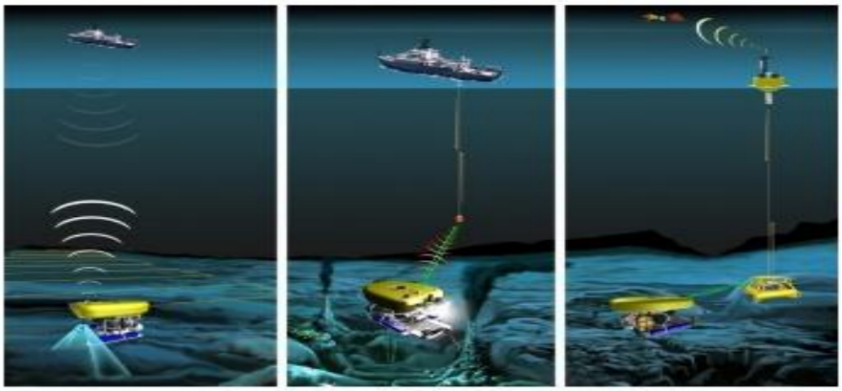

Figure 1.10: Operation of UTROV

capability. Figure 1.10 illustrates the operation of this application, the right pane shows the UTROV communication using the optical channel to a fixed infrastructure on the sea floor. In the center, the communication is realized by UTROV using the optical channel with a ship based on the relay infrastructure. The left panel shows UTROV communication using low bandwidth underwater communications.

1.7 Conclusion

In this chapter, we have discussed the essential aspects of visible light communication (VLC) technology. We began by defining VLC and discussing its key concepts. Then, we reviewed the different models of VLC transmitters and receivers and the modulation techniques used in this technology. The chapter ended by exploring the various application areas of VLC technology, providing a comprehensive understanding of this cutting-edge technology. The information presented in this chapter serves as a valuable resource for anyone interested in learning more about VLC technology and its practical applications.

Overall, the chapter provides a comprehensive overview of VLC technology, making it a valuable resource for researchers, practitioners, and students alike.

In the next chapter, we will delve into a crucial aspect of designing a VLC system: the optical channel. This chapter will provide a comprehensive overview of the theoretical foundations of the VLC channel and the various models that have been proposed in the literature.

CHAPTER 2

CHANNEL MODELING APPROACH

2.1 Introduction

In recent years, there has been a significant increase in research activities on visible light communication (VLC) in both academia and industry. The growing interest in this technology has led to numerous research studies and surveys [21, 32, 28, 38, 28, 39, 40, 20].

As any wireless communication system, the performance of a VLC system is heavily influenced by the characteristics of the propagation channel and the transmitter/receiver front-ends. Accurate channel models are therefore essential for the proper design, evaluation, and testing of VLC systems.

In this chapter, we will concentrate on the propagation channel models for visible light communication systems. The chapter will cover the classification of the various models developed in the literature according to the environment, and examine their impact on the performance of VLC systems. We will start by introducing the different channel scenarios and their key features. Then, we will delve into the different channel statistics, including channel impulse response, path loss, and channel gain. The chapter will conclude with an overview of the different channel models that have been developed in the literature, highlighting their main characteristics and the strengths and weaknesses of each model.

2.2 Channel Scenarios

There are several possible configurations for the VLC link. Firstly, they can be divided into two large families according to the presence or absence of a direct path between the transmitter (OTx) and the receiver (ORx), namely the links in direct visibility (LoS "Line of Sight") and the links in indirect visibility (non-LoS "non-Line of Sight"). Secondly, each of the two LoS and non-LoS configurations can be divided into three types of links according to the degree of directionality of the transmitter and/or receiver, i.e. directional

and non-directional links. The above mentioned link configuration classifications are illustrated in Figure 2.1 [41] .

2.2.1 Directional LoS link (DLoS)

Also known as a point-to-point link, the directional LoS link uses narrow beam transmitters and low Field of view (FoV) receivers. It maximizes energy efficiency and minimizes power consumption as the transmission is focused on the direct path. This type of link does not suffer from dispersion due to multipath because the power contributions of the reflections are often relatively very small compared to the power received from the direct path. However, this comes at the cost of limited coverage area, limited mobility, and strict link alignment [42]. The main disadvantage of DLoS links is their sensitivity to shadowing and blockage, which can greatly reduce the performance of the communication system.

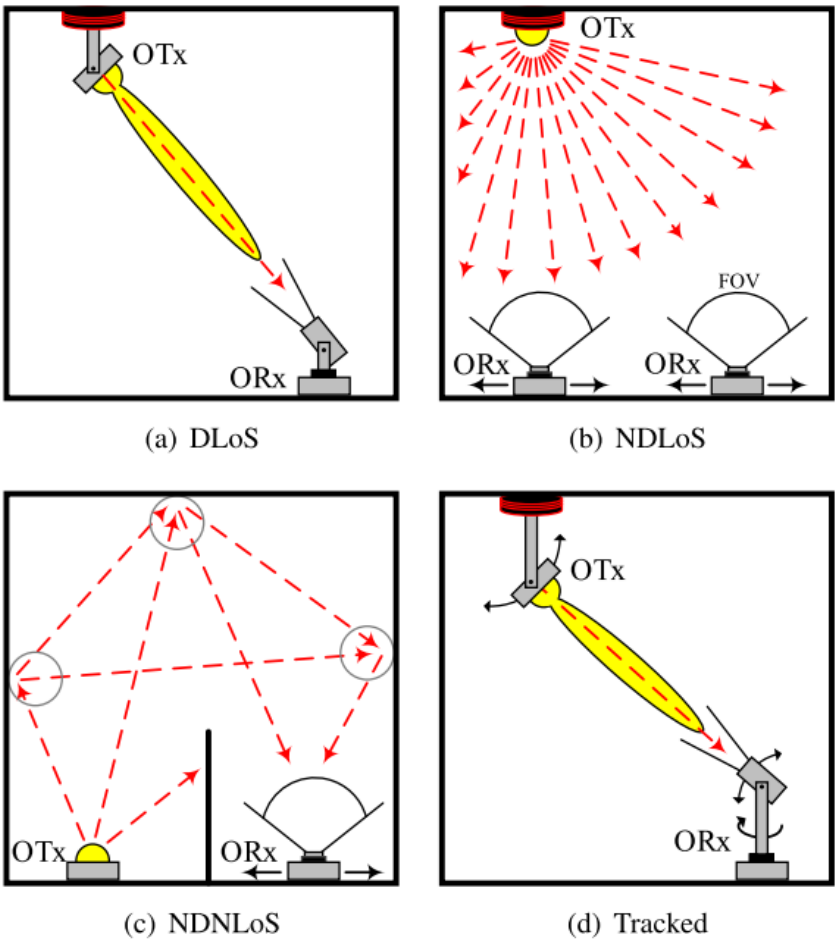

Figure 2.1: VLC channel scenarios

2.2.2 Non-Directional LoS link (NDLoS)

Non-directional Line of Sight (NDLoS) links, also known as wide LoS links [43], have a wider coverage area and offer greater flexibility compared to DLoS links [44]. Both the transmitter and receiver have a wide optical aperture, which results in a wide Field of View (FoV) for the receiver and a wide beam divergence angle for the transmitter. No alignment is required for NDLoS links, making them convenient for mobile terminal applications or point-to-multipoint broadcast systems. This scenario is commonly used for indoor and underground communication systems.

2.2.3 Non-Directional Non-LoS link (NDNLoS)

The NDNLoS link design does not require an LoS connection between the transmitter and the receiver. In this configuration, a transmitter with wide beam divergence is pointed at the ceiling and the diffuse reflections from the ceiling, walls, and objects are used to establish a link to a wide FoV receiver that also faces the ceiling (see Figure 2.1). This broadcast link maintains a sustained connection between the transmitter and receiver, providing users with a large degree of mobility and robustness against link loss due to blockage. [45].

2.2.4 Tracked

This scenario is proposed to enable user mobility, reduce multipath induced ISI, improve energy efficiency, and provide high data throughput in a single link configuration [46]. Tracking systems can be integrated into ceiling-mounted transceivers (base stations), mobile terminals or both [47]. The tracking mechanism is achieved through three main components: an acquisition unit for detecting new mobile stations in a specific area, a tracking unit for following the mobile station, and a pointing unit for directing the optical beam towards the mobile station. This allows for the optical beam to be placed parallel to or on the mobile station, maintaining the connection even when the user is moving.

2.3 Noise sources

In Visible Light Communication systems, there are several sources of noise that can affect the quality of the communication. These sources of noise can be induced by the optical channel, such as ambient optical noise from external sources like sunlight or artificial lighting, or generated locally by the receiver, mainly due to thermal noise. These sources of noise can reduce the signal-to-noise ratio (SNR) of the system, leading to decreased communication performance. It is important to understand these sources of noise and take steps to minimize their impact on the system.

2.3.1 Ambient optical noise

Ambient optical noise is considered as one of the main limitations in the field of VLC systems. This noise is characterized by disturbances from light sources other than the transmitting system that are present in the environment. As a result, the photodiode in the receiver can detect stray light in addition to the useful signal. This phenomenon is illustrated in Figure 2.2 [48], where we observe in this case that, for the visible wavelengths, the predominant sources of optical noise are related to the sun and artificial sources such as incandescent or fluorescent lamps. When we move away to the infrared, we note that the noise generated by fluorescent lamps becomes zero. The noise of the ambient light is

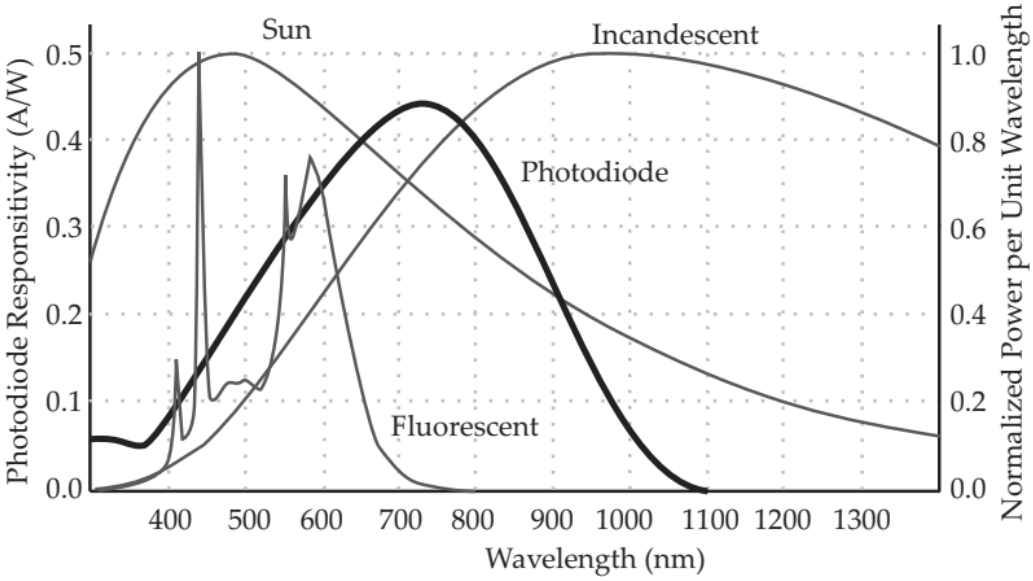

Figure 2.2: Responsitivity of a Thorlabs PDA10A Si-PIN photodiode compared to the spectral power distribution of ambient light sources.

generally modeled by a Poisson distribution. Being independent of the emitted signal, it is classically represented by a white Gaussian noise [49]. It is characterized by a photo-current I_b at the photodiode that depends on the power of the ambient light and the sensitivity of the component. The variance associated with optical noise can be expressed by :

$$\sigma^2_{shot} = 2q\,(I_r + I_b)\,B \tag{2.1}$$

where q the elementary electron charge ($\approx 1.6\times10^{-11}19$ C) and B the bandwidth of the photodiode. The value of the photo-current I_r is related to the intensity of the received signal. This corresponds to the noise that can be randomly generated by the movement of electrons during the creation of an electric current.

2.3.2 Thermal Noise

The thermal noise due to the thermal agitation of the electrons is linked to the electronics of the receiver, in particular to the type of amplifier used (typically a current/voltage or transimpedance amplifier) as well as to the associated electronic components (resistor, bipolar transistors, field effect transistors...). This noise is specific to each component, and even if it is possible to reduce it by optimizing its manufacture, it is impossible to eliminate it completely. It depends on the conductivity of the material, its temperature and is generated independently of the received signal. It is classically considered as white Gaussian noise, having a power spectral density independent of frequency. Its variance can be generalized by :

$$\sigma^2_{\text{thermal}} = \frac{4KT_eB}{R_L} \tag{2.2}$$

where K is the Boltzmann constant, T_e the absolute temperature of the system, R_L the equivalent resistance of the circuit. There are other types of noise (e.g. related to the detector capacitance) but they are mostly negligible compared to the ambient optical noise and the thermal noise. The variance of the total noise is then the sum of those of the ambient optical noise and thermal noise, both corresponding to a white Gaussian noise:

$$\sigma^2_{\text{noise}} = \sigma^2_{\text{shot}} + \sigma^2_{\text{thermal}} \tag{2.3}$$

2.4 Theoretical Foundations of VLC Channels

To evaluate the performance of VLC systems, VLC channel modeling is an essential task. The basic VLC channel can be modeled as a base-band Linear Time-Invariant (LTI) system [50] with a non-negative impulse response $h(t) > 0$ as shown in Figure 2.3. It is

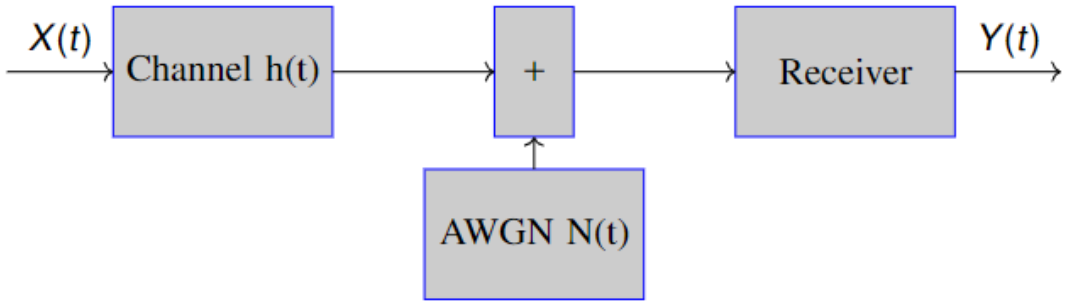

Figure 2.3: VLC channel model

expressed as follows: [27], [51]

$$Y(t) = RX(t) * h(t) + N(t). \tag{2.4}$$

where $Y(t)$ is the electrical received signal, R is the PD responsivity in (A/W), $X(t)$ is the input optical power which can not be negative ($x(t) > 0$), $h(t)$ is the base-band Channel Impulse Response (CIR), * denotes convolution, and $N(t)$ is the receiver noise, which can be modeled as Additive White Gaussian Noise (AWGN).

In order to ensure a reliable, secure, and efficient design and implementation of the VLC system, it is crucial that the main features of VLC channels must be understood. Hereafter, we describe the primary features of VLCs.

2.4.1 Channel Impulse Response h(t)

The channel impulse response (CIR) is the evolution of the received signal over the time when the infinitely of light is launched by the emitter [52]. It provides comprehensive information about the characteristics of the channel [53]. CIR is determined by the specific arrangements of the transmitter, receiver, and any reflectors involved [54].

Mathematically, for a specific light source S and receiver R, the total channel impulse response at time t is the sum of responses from LoS and all reflections from NLoS links, can be expressed as [55], [5], [56]

$$h(t, S, R) = \sum_{k=0}^{\infty} h^{(k)}(t, S, R). \tag{2.5}$$

where $h^{(0)}(t, S, R)$ is the LoS response, $h^{(k)}(t, S, R)$ is the response of the light undergoing exactly k reflections.

The LoS impulse response can be expressed as [57]

$$h^{(0)}(t, S, R) = \frac{1}{(d)^2} S(\Phi, m, \lambda) A_{eff}(\psi) \delta(t - \frac{d}{c}). \tag{2.6}$$

where $S(\Phi, m, \lambda)$ represents the emitter's radiation power as a function of the wavelength (λ), δ is a Dirac delta function, m is the radiation lobe mode number, d denotes the distance between the transmitter and the receiver, c is the speed of light ($3 \times 10^8 m/s$), $A_{eff}(\psi)$ represents the effective area of the receiver, and ψ is the angle of incidence.

2.4.2 Channel Direct Current Gain H(0)

One of the most important features of a VLC system is the Channel Direct Current (DC) gain. It returns the feasible signal-to-noise ratio for fixed transmitter power and can be expressed as [27]:

$$H(0) = \int_0^{\infty} h(t) dt. \tag{2.7}$$

Mostly, the channel DC gain amplitude value $H(0)$ is used to identify the losses in the channel, which associates the average optical power received P_r, to the transmitted one

P_t, as follows [58]:

$$P_r = H(0)P_t. \tag{2.8}$$

In LoSpath, if the emitter is modeled by a generalized Lambertian pattern, $H(0)$ can be obtained by [5]:

$$H(0) = \begin{cases} \frac{(m+1)A_{PD}}{2\pi d^2} \cos^m \Phi T_s(\psi) g(\psi) \cos\psi & , 0 \leq \psi \leq \psi_c \\ 0 & 0 \geq \psi_c \end{cases} \tag{2.9}$$

where A_{PD} represents the PD surface area, m is the Lambertian mode number, ψ_c is the receiver FOV (semi angle), Φ is the irradiance angle, and d denotes the distance from LEDs to the Rx point. Also, $T_S(\psi)$ is the optical filter gain, and $g(\psi)$ is the optical concentrator gain. In (2.9), ψ denotes the incidence angle at the PD.

2.4.3 Root Mean Square (RMS) Delay Spread

The Root Mean Square (RMS) delay spread is a measure of the dispersion of the channel over time. It is calculated as the square root of the second central moment of the CIR and provides information about the spread of the received signal over time. This information is used to quantify the degree of time dispersion and to estimate the inter-symbol interference [59]. RMS delay spread is given by the following equation [60]:

$$\tau_{RMS} = \sqrt{\frac{\int_{-\infty}^{\infty}(t-\tau_0)^2 h^2(t)dt}{\int_{-\infty}^{\infty} h^2(t)dt}}. \tag{2.10}$$

where τ_0 represents the mean excess delay and t is the propagation delay time. The mean excess delay is given as follows [60]:

$$\tau_0 = \frac{\int_{-\infty}^{\infty} t \times h^2(t)dt}{\int_{-\infty}^{\infty} h^2(t)dt}. \tag{2.11}$$

The RMS delay spread is a critical performance criterion for calculating the upper bound of reliable data transmission rate. The maximum bit rate (Rb) transmitted through the wireless optical channel can be approximated by [61]:

$$Rb \leq \frac{1}{10\tau_{RMS}}. \tag{2.12}$$

Consequently, this allows to assign the limit on the symbol length used to avoid inter-symbol interference (ISI)[58]. It should be noticed that this equation is only valid if no equalization technique is used.

2.4.4 Optical Path Loss (OPL)

The optical path loss (OPL) represents the decrease in the received optical signal power during its transmission through the environment. The OPL depends on the transceiver and environmental parameters. This includes the reflectivity of nearby objects, atmospheric scattering, weather conditions, light source's radiation pattern, and the orientation of both the transmitter and receiver. The OPL can be given by

$$OPL = -10 \log_{10} H(0). \tag{2.13}$$

2.4.5 Frequency Response H(f)

The channel frequency response $H(f)$ describes how the channel behaves for different frequency components of the signal. It is calculated by taking the Fourier Transform of the calculated impulse response $h(t)$ [62], which remains constant for a specific room setup and transmitter/receiver positions and configurations.

$$H(f) = \int_{-\infty}^{\infty} h(t) \exp^{-j2\pi ft} \, dt. \tag{2.14}$$

In practice, the -3dB frequency of the optical channel can be obtained as [63], [64], [65]:

$$|H(f_{-3dB})|^2 = 0.5|H(0)|^2. \tag{2.15}$$

The -3dB bandwidth is commonly calculated and defined as the frequency at which the amplitude of $20 \log_{10} H(\varpi)$ declines 3dB compared with that at the zero frequency or DC component [56].

2.4.6 Rician Factor

The Rician factor quantifies the power ratio between the LoSand Single Bounce (SB) components, keeping the assumption of the transmitted power as 1 W [27]. It is given by the following equation:

$$K_{rf} = \frac{P_{Los}}{P_{SB}}. \tag{2.16}$$

2.4.7 Coherence Bandwidth (B_c)

Coherence bandwidth (B_c) is defined as the range of frequencies over which the channel frequency response can be considered flat. In the literature, B_c was estimated using several approaches[66]. Based on τ_{RMS}, B_c is approximated as the bandwidth over which the frequency auto-correlation function (FCF) is above 0.5 [66]. It can be expressed as

[67]:

$$B_c(0.5) = \frac{1}{5\tau_{RMS}}. \tag{2.17}$$

2.5 Channel Models

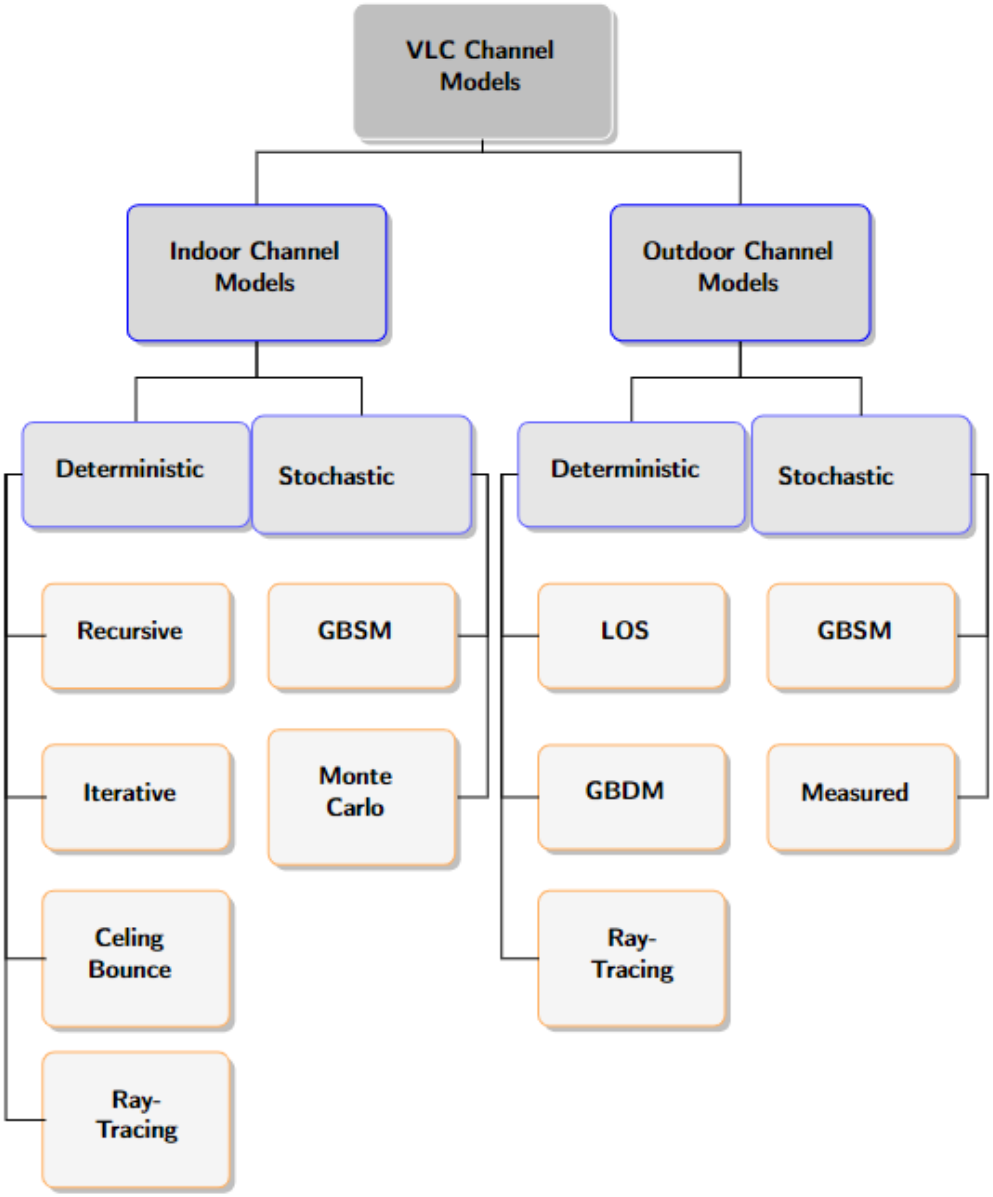

Figure 2.4: Classification of VLC Channel Techniques.

This section outlines the different channel models used in VLC systems. As illustrated in Figure 2.4, the VLC channel model can be classified by environment into deterministic and stochastic models. For example, if we consider the indoor environment, different approaches are included in the deterministic approach, for example, recursive, iterative,

ceiling bounce and ray tracing. On the other hand, the stochastic models can be classified into geometry-based stochastic models (GBSM) and Monte Carlo.

For the outdoor channel, the deterministic approaches include LoSchannel, geometry-based deterministic models (GBDM) and ray tracing. On the other hand, stochastic models can be classified into geometry-based stochastic models (GBSM) and measured channels.

2.5.1 Deterministic Models

Deterministic channel models are typically based on the precise geometry of the surroundings, including the room, transmitter, receiver, and reflectors. Below, we provide a concise overview of the various deterministic methods used in VLC systems.

Recursive Model

Recursive channel model was originally proposed by Barry et al. [57] for IR channel models, in which the reflecting surface of the room (ceiling, wall, and floor) is divided into N small reflective elements, each with its own area and reflection coefficient. In this model, the radiation intensity pattern $R(\phi)$ for a particular emitter can be modeled using a generalized Lambertian radiation pattern as follows [68]

$$R(\phi) = \frac{m+1}{2\pi}\cos^m(\phi), \phi \in [-\pi/2, \pi/2]. \tag{2.18}$$

where m is the mode number of the radiation lobe, which specifies the directivity of the optical source and ϕ is the irradiation angle. On the receiving end, the receiver is modeled as an active A_r area collecting radiation that is incident at an angle θ smaller than the FoV of the PD. For a particular optical source S and optical receiver R in a room with Lambertian reflectors, the light from the transmitter can reach the receiver through direct or multiple paths. Therefore, the CIR is the superposition of the LoSand a sum of multiple bounce components as follows

$$h(t; S, R) = h^0(t; S, R) + \sum_{k=1}^{\infty} h^k(t; S, R) \tag{2.19}$$

where $h^0(t)$ is the LoS component and $h^k(t)$ is the component undergoing exactly k reflections. The LoS component can be given as [57]

$$h^0(t) \approx \frac{(m+1)A_{\mathrm{R}}}{2\pi d^2}\cos^m(\phi)\cos(\theta)\delta(t - d/c) \tag{2.20}$$

where d is the distance between the transmitter and the receiver, c is the light speed. As we have seen before, the recursive model decomposes the reflective surfaces into many

small Lambertian reflective elements, each of them having an area Δ. Each cell acts both as an elementary receiver (ϵ^r) and as an elementary source (ϵ^s). Thus, for a higher order of reflection $k > 0$, the CIR can be calculated recursively and approximated as follows [57]

$$\begin{aligned} h^k(t;S,R) \approx & \sum_{i=1}^{N} \rho_{\epsilon_i^r} h^{(0)}\left(t;S,\epsilon_i^{\mathrm{r}}\right) \circledast h^{(k-1)}\left(t;\epsilon_i^{\mathrm{s}},R\right) \\ = & \frac{m+1}{2\pi} \sum_{i=1}^{N} \frac{\cos^m(\phi)\cos(\theta)}{d^2} \\ & \times \mathrm{rect}(2\theta/\pi) h^{(k-1)}\left(t-d/c;s_i,R\right)\Delta. \end{aligned} \tag{2.21}$$

where ρ is the cell reflectivity coefficient and s_i is the position of each cell.

Iterative Model

Iterative model was proposed initially by Carruthers and Kannan [69] for IR channel models as an alternative to the recursive models in order to reduce the computation time. These models are then extended to the VLC channel. In this method, the calculation of CIR follows the basic methodology described in [57] with extensions for an arbitrary number of boxes within the environment. The $h^0(t)$ of the LoS component can be given as (2.20), while the k-bounce response can be expressed as

$$h^k(t;S,R) \approx \sum_{i=1}^{N} \rho_{\epsilon_i^r} h^{(k-1)}\left(t;S,\epsilon_i^r\right) \circledast h^0\left(t;\varepsilon_i^s,R\right) \tag{2.22}$$

According to the iterative algorithm, (2.22) can be applied with $R = \epsilon_j^r$ to obtain

$$h^k\left(t,S,\epsilon_i^r\right) = \sum_{j=1}^{N} \mathrm{rect}(2\theta/\pi) \frac{\rho_{\epsilon_j^r} \cos^m\left(\phi_{ij}\right)\cos\left(\theta_{ij}\right)}{P^2 d_{ij}^2} h^{(k-1)}\left(t-d_{ij}/c;S,\epsilon_j^r\right) \tag{2.23}$$

where d_{ij} is the transmitter-receiver distance and P is spatial partitioning factor of cells. Also, θ_{ij} and ϕ_{ij} are the incident and irradiance angles, respectively.

Ceiling Bounce Model

Ceiling bounce models (CBMs) are originally used for IR wireless communication [54], in which a closed-form expression of the CIR is established assuming a specific geometry of the transmitter, receiver and reflectors. It can be given as follows

$$h(t,a) = H(0)\frac{6a^6}{(t+a)^7}u(t) \tag{2.24}$$

where, $u(t)$ is the unit step function and a is an environment-related parameter, $a = (2 \times H_c)/c$, here H_c is the ceiling height.

Ray Tracing Methodology

In this section, we describe the ray tracing methodology. Ray Tracing is a very useful method for the estimation of the CIR through regions with various environment specifications including geometry, transmitter/receiver specifications, and reflection characteristics. There are two modes of ray-tracing: i) sequential mode; ii) non-sequential mode. In sequential ray tracing, rays are traced through a predetermined set of surfaces where only a single hit considered on each surface. This mode is suitable for imaging systems [70].

On the other hand, in the non-sequential mode, there is no predefined set of surfaces. The ray is propagated in any order through the environment that allows the scattering and reflection of the rays back to any object they encountered [70]. The main steps of the non-sequential ray tracing can be described as the following:

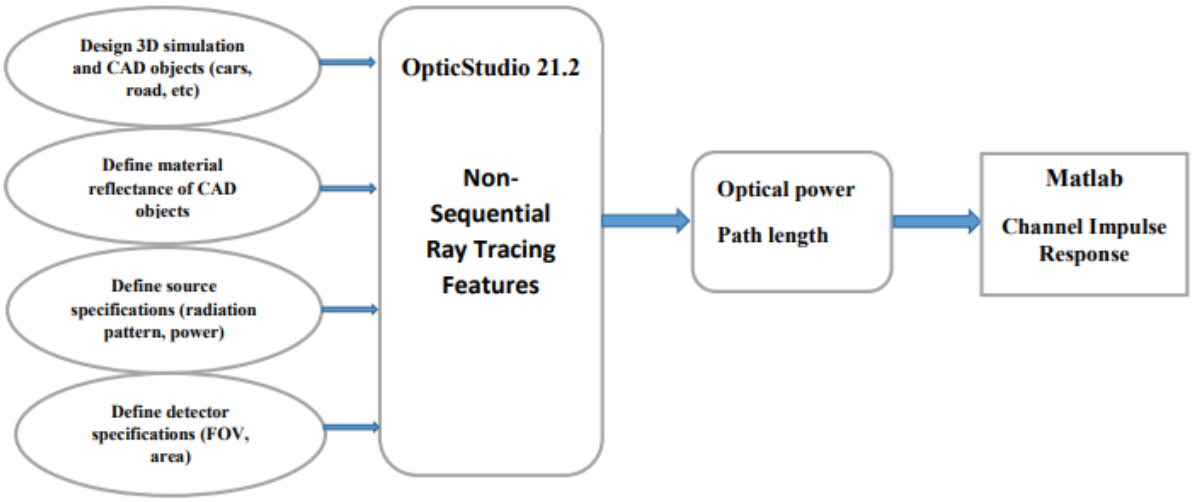

Figure 2.5: Main steps of ray tracing channel modeling.

Design:

The first step is to design a 3D simulation model of the test environment in OpticStudio. After that, we design and import the CAD models of the objects inside, i.e., furniture, people, vehicles, poles, roads, etc. As part of our CAD model generation process, OpticStudio's built-in tools such as Part Designer are used along with external software such as AutoCAD, SolidWorks, Rhino, and others, as well as importable models such as Free3D, GrabCAD, and TurboSquid.

Define:

In this step, we define the specifications of the 3D environment and its imported CAD components. In the simulation platform, the coating materials of these CAD objects can

be specified in terms of wavelength-dependent reflectance as well as scattering fractions. After that, we define the specifications of the light source such as the intensity profile, transmit optical power, spectral intensity, and orientations from the "Source Type" tool. We then define the specifications of the detector such as the field of view angle, the aperture size, and the orientations.

Analyse:

Once all definitions have been applied, we specify the ray tracing parameters which include the number of rays and the maximum number of objects the light will reach. The non-sequential ray tracing is finally executed where the detected optical powers and the path lengths are calculated for each ray arriving at the detector. Such output data is then imported into Matlab software using Ray Database viewer tool to calculate the channel impulse response, which can be given by

$$h(t) = \sum_{i=1}^{N} P_i \delta\left(t - \tau_i\right) \tag{2.25}$$

where N is the number of rays received by the phototdetector and δ is the Dirac delta function. Also, P_i and τ_i respectively denote the power and the propagation delay of the i^{th} ray received by the PD.

2.5.2 Stochastic Channel Models:

In stochastic approaches, the impulse responses of VLC channels are defined by the law of light propagation applied to a specific geometry of transmitter, receiver, and scatterer, which are stochastically predefined according to certain probability distributions. Compared to the deterministic approach, the stochastic approach offers greater flexibility and reduced computational complexity, but with lower accuracy [41].

Geometric-Based Stochastic Models (GBSM)

The Geometric-Based Stochastic Model (GBSM) is one of the most important approaches to channel modeling. It is derived from a predefined stochastic scattering distribution by applying the fundamental laws of wave propagation. This model is adapted to various scenarios by changing the shape of the scattering region [71]. GBSMs can be classified into regular shaped GBSMs (RS-GBSMs) or irregular shaped GBSMs (IS-GBSMs) depending on whether the effective scatterers are placed on regular (one/two rings, ellipse) or irregular (random) shapes.

Monte Carlo Algorithm (MCA)

The Monte Carlo algorithm (MCA) is one of the most popular alternative methods for estimating CIRs. In this approach, rays are emitted with equal optical power in directions generated with a probability density function of the Lambertian model. MCA was first applied to the IR channel and then extended to the VLC channel. Furthermore, it allows the evaluation of not only the impulse response for Lambertian reflections but also for specular reflections. The computational complexity and simulation time of the Monte Carlo approach is less compared to the recursive approach. However, the main disadvantage of the MCA is that, for a normal sized room, many more rays must be sent than that will be received. Indeed, not all the rays will be intercepted by the receivers.

2.6 Conclusion

In this chapter, we have covered the essential concepts and theories behind the optical wireless channel, including the different channel scenarios and channel statistics. We have also provided a comprehensive overview of the existing channel models in the literature, and classified them based on the communication environment. This chapter provides a solid foundation for understanding the optical wireless channel, which is a critical component in the design and performance evaluation of visible light communication systems.

In the next chapter, we will focus on the use of ray tracing as a tool to model the VLC channel and analyze the performance of Vehicle-to-Vehicle and Vehicle-to-Infrastructure VLC systems.

CHAPTER 3

PERFORMANCE EVALUATION OF VEHICULAR VISIBLE LIGHT COMMUNICATION BASED ON ANGLE-ORIENTED RECEIVER

3.1 Introduction

In this chapter, we utilize the channel modeling methodology described in Chapter 2 for modeling V2V and V2I channels. It can be noted that most of current research in V2V communication operates under the assumption that vehicles are perfectly aligned within the same lane, ignoring lateral offsets [72, 73, 74, 75]. This assumption may not reflect real-world conditions, where there is often misalignment between vehicles even if they are in the same lane. Some studies [76, 77] have considered the effect of lateral shift but only in single-lane scenarios. Due to such idealistic scenarios, they assumed the use of a single PD on the destination car [72, 74, 76, 77]. In such cases, the use of a single PD is not sufficient to ensure reliable communication and can result in communication failures especially when the cars are in different lanes [78, 79, 80, 81].

In addition to V2V links, V2I systems also relied on some unrealistic assumptions, such as perfect alignment of vehicles in the same lane without considering lateral offset [82]. This can lead to inaccurate results and a lack of reflection of real-world conditions. Another issue is the use of a single receiver, which can negatively impact the performance of the system when communication occurs across different lanes as in [83]. The rest of this chapter is organized as follow. In section 3.2 describes the V2V-VLC system and channel model. We then derive closed form expressions of the maximum achievable transmission distance for a target BER performance. The impact of the different system parameters such as the receiver FoV, the receiver aperture diameter, and the modulation bandwidth has been investigated. A comprehensive performance comparison is then conducted in terms of achieved data rates, maximum achievable distance, and packet delivery ratio for different numbers of PD. In section 3.3, we describe the V2I-VLC system. Finally, we conclude in section 3.4

3.2 V2V VLC Link

3.2.1 System and Channel Model

In this section, we describe our system and channel model under consideration. As shown in Figure 3.1, our system involves three cars (i.e., Car 1, Car 2, and Car 3) moving on a multi-lane road with a width of W_l for each lane and a total of K lanes. The cars are located in the middle of each lane with a separation distance of d_y between their centers. Each car has two headlamps that serve as transmitters and have asymmetrical radiation patterns designed to meet specific illumination requirements, different from indoor luminaries [37]. The headlamps transmit information to a destination car (Car 4) with an optical power of P_{opt}. The destination car is located at the front and in the middle of the central lane, with a longitudinal offset of d from the other vehicles. An Angle Oriented Receiver (AOR) with N PDs with different orientation angles, placed at the back of the Car 4, acts as a wireless receiver (see Figure 3.2a). In the following, we

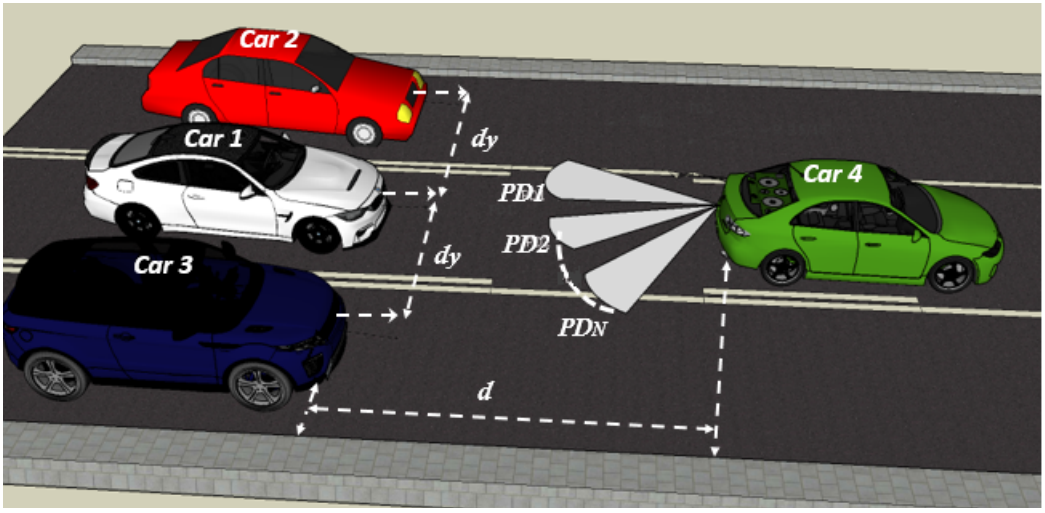

Figure 3.1: V2V-VLC system under consideration.

explain the mathematical model of the AOR under consideration. The AOR is a group of PDs in which each PD is oriented in a different direction to cover a specific area of the road. These PDs have narrow FoVs chosen to restrict the number of approved optical beams and to limit the background noise. In this work, we consider an AOR receiver with N PDs. Each of these PDs has an identical FoV denoted by ψ, an aperture diameter of D_R, and a responsivity of R. Each PD points in a specified direction which can be set by two angles, i.e., elevation angle (γ_j) and azimuth angle (ε_j). Therefore, the normal unit vector on the j^{th} PD can be defined by its position and orientation, which is represented by [84]

$$\boldsymbol{n}_{PD_j} = (x_j, y_j, z_j, \varepsilon_j, \gamma_j) \quad \text{for } 1 \leq j \leq N, \tag{3.1}$$

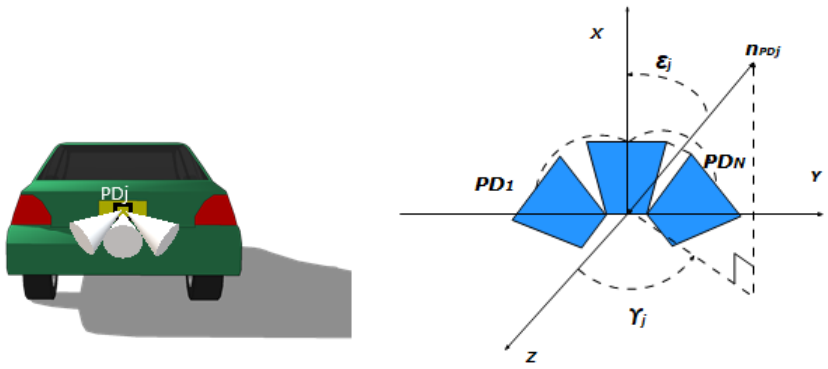

Figure 3.2: (a) Location of the AOR on the car (b) PDs coordinates.

where (x_j, y_j, z_j) are the Cartesian coordinates, ε_j, and γ_j are the angles measured from the positive x-axis, and the positive z-axis, respectively (see Figure 3.2b). They can be varied as follows:

- PDs elevation angles can be varied by $\gamma_j \in [0, \pi]$.
- PDs azimuth angles can be varied by $\varepsilon_j \in [0, 2\pi]$. Thus, ε_j will be evenly distributed, according to the following expression [84]

$$\varepsilon_j = \frac{2(j-1)\pi}{N}. \tag{3.2}$$

According to these angles and considering that all PDs are uniformly organized in a circle of radius r, the effective coordinates of the j^{th} PD can be obtained as:

$$(x_{\mathrm{PD}_j}, y_{\mathrm{PD}_j}, z_{\mathrm{PD}_j}) = (x_R + r\cos\varepsilon_j, y_R + r\sin\varepsilon_j, z_R), \tag{3.3}$$

where x_R, y_R, z_R are the coordinates of the AOR center point on the vehicle.

In the VLC system, the intensity of the LED is modulated by the information signal, then the emitted light propagates through the free space. In our study, we applied the non- sequential ray tracing features of OpticStudio simulator, described in Chapter 2 to model the vehicular VLC channel. Thus, The corresponding optical CIR can be expressed as

$$h_{i,k,j}(t) = \sum_{l=1}^{M_{i,k,j}} P_{i,k,j}(l)\delta\left(t - \tau_{i,k,j}(l)\right), \tag{3.4}$$

where $M_{i,k,j}$ is the number of rays emitted from the i^{th} headlamp of the k^{th} car and captured by the j^{th} receiver. Also, $P_{i,k,j}$, and $\tau_{i,k,j}$ are respectively denote the power and the propagation delay. Here, δ is the Dirac delta function. Based on this channel modeling approach, and to further take into account the effect of the receiver field of view,

we introduce the use of the following equation

$$Pr_{k,j} = \sum_{i=1}^{2} P_{opt}\ H_{i,k,j}\ g_c\left(\theta_{i,k,j}\right), \tag{3.5}$$

where $Pr_{k,j}$ is the received power at the j^{th} PD from the k^{th} car, $g_c\left(\theta_{i,k,j}\right)$ is the concentrator gain, $\theta_{i,k,j}$ is the incident angle, and $H_{i,k,j}$ is the channel gain between the i^{th} headlamp of the k^{th} car and the j^{th} PD, which can be expressed as (3.6)

$$H_{i,k,j} = \left(\frac{D_R\left(\cos\left(\theta_{i,k,j}\right)\right)^{1/\alpha}}{\beta\sqrt{d^2 + d_{h_{i,k,j}}^2}}\right)^2 \exp\left(-c\sqrt{d^2 + {d_{h_{i,k,j}}}^2}\left(\frac{D_R}{\beta\sqrt{d^2 + {d_{h_{i,k,j}}}^2}}\right)^{\alpha/2}\right). \tag{3.6}$$

In (3.6), $d_{h_{i,k,j}}$ is the lateral shift between the i^{th} headlamp of the k^{th} car and the j^{th} PD, c is the extinction coefficient for a particular type of weather condition, and β and α are correction coefficients.

The concentrator gain, $g_c\left(\theta_{i,k,j}\right)$, in (3.5) can be calculated as [27]

$$g_c\left(\theta_{i,k,j}\right) = \begin{cases} \frac{\eta^2}{\sin^2(\psi)} & \theta_{i,k,j} \leq \psi \\ 0 & \theta_{i,k,j} > \psi \end{cases} \tag{3.7}$$

where, η is the refractive index.

Achievable Capacity

The end to end SNR between the k^{th} car and the j^{th} PD can be expressed as follows [85]

$$\Gamma_{k,j} = \frac{R^2 Pr_{k,j}^2}{\sigma_t^2}, \tag{3.8}$$

where σ_t^2 denotes the total noise variance that affects the vehicular environment. It can be expressed as follows [73]

$$\sigma_t^2 = N_0 B, \tag{3.9}$$

where N_0 is the noise power spectral density and B is the bandwidth. The AOR configuration consists of several PDs however to maximize the system performance, we consider the use of the Equal Gain Combining scheme (EGC). This scheme differs from the Select Best Combining (SBC) scheme, in which only one PD with the highest SNR value is used. Instead, the EGC scheme takes advantage of other PDs and combines the signals from all PDs with equal weighting, resulting in an increase in the overall received SNR. Therefore,

the final SNR at the k^{th} car is given as

$$\Gamma_k = \sum_{j=1}^{N} \Gamma_{k,j}. \tag{3.10}$$

Generally, for a VLC system with Intensity Modulation and Direct Detection (IM/DD), the precise capacity equation is not yet identified. Thus, several expressions have been derived in the literature for the upper and lower bounds of the channel capacity in VLC systems [86, 87, 88, 89, 90]. For instance, the difference between the exact and lower limits for high SNR values can be ignored as shown in [90]. Therefore, the capacity can be estimated as:

$$C_k \approx \frac{B}{2\ln(2)} \ln\left(1 + \frac{\exp(1)\Gamma_k}{2\pi}\right). \tag{3.11}$$

Achievable Transmission Distance:

Based on the presented channel gain in Eq (3.6), we derive the achievable transmission distance for a targeted data rate while satisfying a target bit error rate (BER). Based on the assumption of $d \gg d_y$ and for a single receiver case, the channel gain can be given by [76]

$$H = \left(\frac{D_R}{\beta d}\right)^2 \exp\left(-cd\left(\frac{D_R}{\beta d}\right)^{\alpha/2}\right). \tag{3.12}$$

From (3.12), the communication distance d can be finally given by [76]

$$d = \left(\frac{\mathrm{W}\left(\frac{c}{4}(2-\alpha)\left(\frac{D_R}{\beta}\right)H^{\left(\frac{\alpha-2}{4}\right)}\right)}{\frac{c}{4}(2-\alpha)\left(\frac{D_R}{\beta}\right)^{\alpha/2}}\right)^{\frac{2}{2-\alpha}}, \tag{3.13}$$

where $\mathrm{W}(xe^x) = x$ represents the Lambert-W function.

On the other hand, the point-to-point bit-error-rate (BER), P_e, for on-off keying (OOK) modulation format is given by:

$$P_e = \frac{1}{2}\,\mathrm{erfc}\left(\frac{\sqrt{\Gamma}}{2\sqrt{2}}\right), \tag{3.14}$$

where $\mathrm{erfc}(x) = \frac{2}{\sqrt{\pi}} \int_x^\infty e^{-t^2} dt$ is the complementary error function, and Γ is the signal-to-noise-ratio.

Thus, the maximum achievable distance can be re-written as follows

$$d = \left(\frac{\mathrm{W}\left(\frac{c}{4}(2-\alpha)\left(\frac{D_R}{\beta}\right)\left(2\sqrt{2}\left(\sqrt{\frac{\sigma_t^2}{R^2 P_{opt}^2}}\right)\mathrm{erfc}^{-1}(2P_e)\right)^{\left(\frac{\alpha-2}{4}\right)}\right)}{\frac{c}{4}(2-\alpha)\left(\frac{D_R}{\beta}\right)^{\alpha/2}} \right)^{\frac{2}{2-\alpha}}. \tag{3.15}$$

Packet Error Ratio:

The packet delivery ratio is another metric used to evaluate the quality of our proposed system. It can be derived (assuming independent bit errors) as follows [91]

$$\Upsilon = (1 - \mathrm{P_e})^n \tag{3.16}$$

where n represents the bit length of the transmitted packet.

3.2.2 Simulation Results and Discussion:

In our simulation study, we consider $K = 3$ where the car should be able to communicate with the following cars either in the same lane or in the neighbor ones to avoid any possible crash. Also, $W_L = 2.5$ m, $R = 0.54$ A/W, $N_0 = 10^{-21}$ A^2/Hz, $d_y = 2.5$ m, and $P_{opt} = 5$ W. Different bandwidths i.e., $B = 1$ MHz, 5 MHz, 20 MHz, 35 MHz, and 50 MHz and different receiver apertures, i.e., $D_R = 1$ cm, 2.5 cm, and 4 cm, are considered. We further assume different receiver FoVs, i.e., $\psi = 5°-90°$. To investigate various AOR configurations, we consider different numbers of receivers, N= 1, 3, and 5. The elevation angles are set as follows: $\gamma_{1,3}$= 75°and $\gamma_2 = 90°$ while the azimuth angles are given by ε_1= 180°, ε_2= 0°, ε_3= -180°. All simulation parameters are listed in Table 3.1. The considered scenarios can be described as the following:

- **Scenario 1:** we consider that Car 1 is placed perfectly with respect to the destination car, i.e., $d_y = 0$ m (see Figure 3.1).
- **Scenario 2:** we consider that Car 2 is placed to the left side of the destination car with a lateral offset of $d_y = 2.5$ m (see Figure 3.1).
- **Scenario 3:** we consider that Car 3 is placed to the right side of the destination car with a lateral offset of $d_y = 2.5$ m (see Figure 3.1).

Impact of PD Numbers

In this section, we evaluate the impact of increasing the number of adopted PDs on the performance of the V2V system. Toward this, we make a comparison between a

Table 3.1: Main Simulation Parameters For V2V-VLC System

System parameters	**Values**
Road Parameters	
Lane width, W_l	2.5 m
Number of lanes, K	3
Transmitter Parameters	
Light wavelength, λ	400 nm-700 nm
Power, P_{opt}	5 W
Bit length, n	9 kB
AOR Parameters	
AOR number	1
PDs number in AOR, N	3, 5
Azimuth of PDs, ε_j	0°, 180°
Elevation of PDs, γ_j	75°, 90°
Responsivity of PDs, R	0.54 A/W
PD aperture diameter, D_R	1cm, 2.5 cm, 4 cm
FoV, ψ	5°−90°
Weather parameters	
Extinction coefficient, c	Clear weather: 0 Rainy weather: 0 Foggy weather: 0.01565
Correction coefficients, β and α	Clear weather: 0.1585 and 0.0175 Rainy weather: 0.1598 and 0.0174 Foggy weather: 0.1550 and 0.0170
Noise parameters	
Bandwidth, B	5-50 MHz
Noise power spectral density, N_0	10^{-21} A^2/Hz

V2V-VLC system without AOR (one PD receiver, $N = 1$) and another that has an AOR receiver with N PDs, where $N \in \{3, 5\}$. To make a one-to-one comparison, we assume the following assumptions for all scenarios: $\psi = 35°$, $B = 1$ MHz, and $D_R = 1$ cm. Figure 3.3 presents the SNR versus the inter-vehicle distance for different numbers of PDs assuming all scenarios under consideration. It is observed that as the number of PDs in the AOR receiver increases, the overall SNR performance improves for both the perfect alignment (see Figure 3.3a) and imperfect alignment (see Figure 3.3b) scenarios. The improvement is most noticeable at smaller distances between the transmitting car and the receiving car, where the SNR is increased significantly. This indicates that the AOR receiver with multiple PDs provides better performance in terms of receiving the signal compared to a single PD receiver. This is due to the fact that as the number of receivers increases, the amount of captured light emitted by the transmitters increases. The results also indicate that increasing the number of PDs in the AOR receiver is an effective way to improve the overall performance of the V2V VLC system. For example, consider $d = 15$ m and the

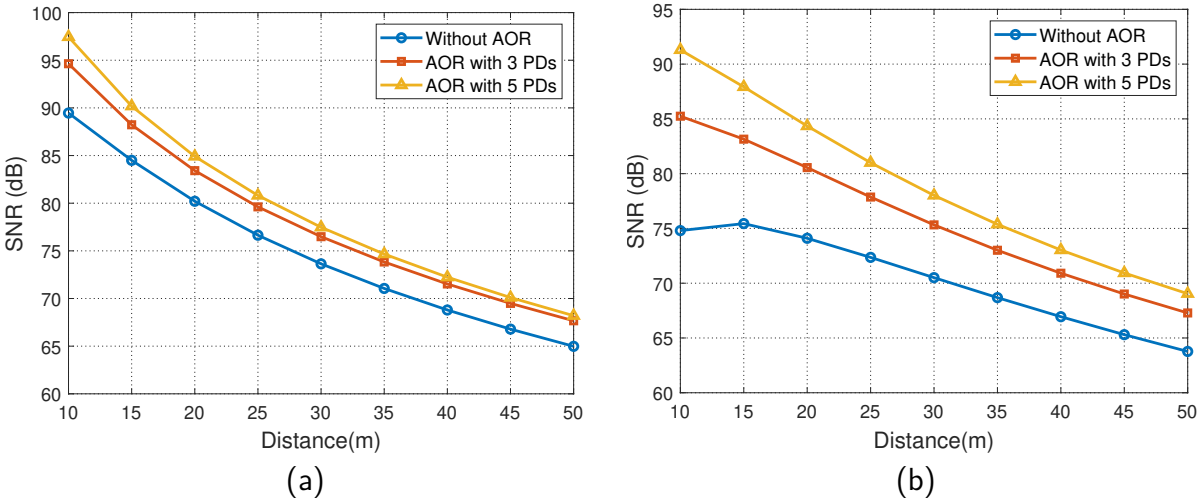

Figure 3.3: SNR versus distance for different PD numbers of AOR: (a) Car 1 (i.e., $d_y = 0$ m), (b) Car 2 and Car 3 (i.e., $d_y = 2.5$ m).

perfect alignment case (i.e., Car 1). The obtained SNR values are given as 84 dB, 88 dB, and 90 dB for N= 1, N= 3, and N= 5, respectively. It is also obvious from Fig. 3.3a that a gap of about 4 dB is existing between $N = 1$, and $N = 3$. While a gap of 2 dB is obtained between $N = 3$ and $N = 5$. Furthermore, it is observed from Figure 3.3b gaps of about 8 and 5 dB between the $N = 1$ and 3, and $N = 3$ and 5, respectively. One can notice also that the lateral offset significantly impacts the SNR performance, especially at shorter inter-vehicle distances. For example, consider $d = 10$ m and $N = 3$. The SNR is given for the perfect alignment case (i.e., lateral shift of $d_y = 0$ m) as 94 dB. This reduces to 85 dB for the lateral shift of $d_y = 2.5$ m. When the distance becomes large enough, the effect of the lateral shift decreases significantly. In other words, as the inter-vehicle distance increases, the angle of arrival at the receiver decreases, allowing more power to be collected. As an example, consider $d = 50$ m and $N = 3$. The obtained SNR values are given as 68 dB and 67 dB for $d_y = 0$ m and $d_y = 2.5$ m, respectively.

Impact of FoV Angle of the PD Receiver

In this part, we investigate the impact of varying the FoV of the receiver on the system performance. Figure 3.4 indicates the total received power versus different PD FoVs for the three scenarios under consideration. We assume that $B = 1$ MHz, $D_R = 1$ cm, $N = 3$, and $d = 20$ m. It is observed that the total received power decreases with the increase of the receiver FoV. The explanation of this behavior is that the wide FoV receiver results in more noise collection at the receiver compared to a narrow one. Hence, it significantly impacts the performance. In addition, a wide FoV corresponds to a lower concentrator gain (see Eq. (3.7)). This, in turn, leads to a reduction in the intensity collected at the receiver. For example, consider the case of perfect alignment (i.e., Car 1). The maximum

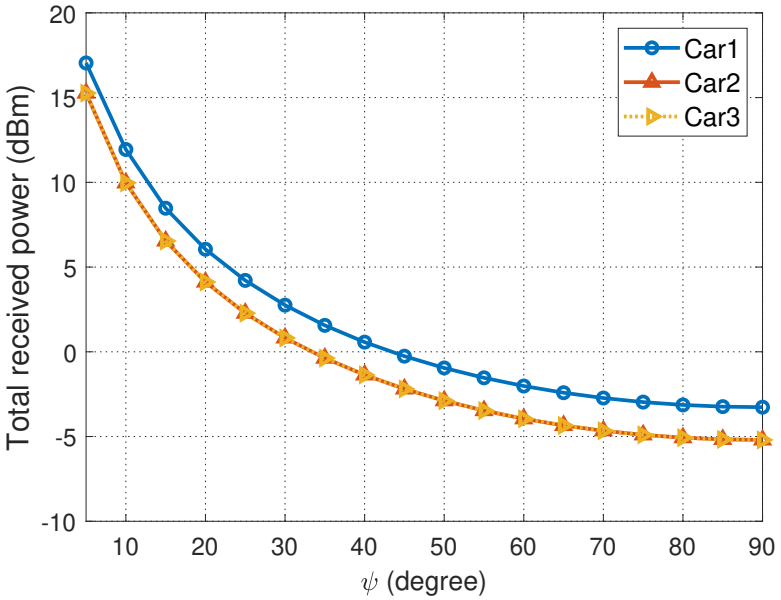

Figure 3.4: Total received power versus receiver FoVs.

Table 3.2: Received power for each PD at different receiver FoVs.

Car1	$\psi = 7°$	$\psi = 8°$	$\psi = 10°$
	P_{r_1}= – ; P_{r_2}= 11.23 dBm; P_{r_3}= – .	P_{r_1}= 6.5 dBm; P_{r_2}= 10.07 dBm; P_{r_3}= 6.5 dBm.	P_{r_1}= 4.5 dBm; P_{r_2}= 8.1 dBm; P_{r_3}= 4.5 dBm.
Car2	$\psi = 4°$	$\psi = 5°$	$\psi = 10°$
	P_{r_1}= 13.3 dBm; P_{r_2}= – ; P_{r_3}= – .	P_{r_1}= 13.7 dBm; P_{r_2}= 10 dBm; P_{r_3}= –.	P_{r_1}= 7.7 dBm; P_{r_2}= 5.1 dBm; P_{r_3}= -1.18 dBm.
Car3	$\psi = 4°$	$\psi = 5°$	$\psi = 10°$
	P_{r_1}= – ; P_{r_2}= – ; P_{r_3}= 13.3 dBm.	P_{r_1}= – ; P_{r_2}= 10 dBm; P_{r_3}= 13.7 dBm.	P_{r_1}= -1.18 dBm; P_{r_2}= 5.1 dBm; P_{r_3}= 7.7 dBm.

value of the total received power is obtained for a receiver FoV of $\psi = 5°$, i.e., 17 dBm. This reduces to -0.2 dBm and -3 dBm for $\psi = 45°$and $\psi = 90°$, respectively. Likewise, consider the imperfect alignment case (i.e., Car 2 and Car 3). The total received power values are given as 15 dBm, -2 dBm, and -5 dBm for $\psi = 5°$, $\psi = 45°$, and $\psi = 90°$, respectively.

To further clarify the effect of the receiver FoV, we quantify the contribution of each PD to the total received power for all considered scenarios.

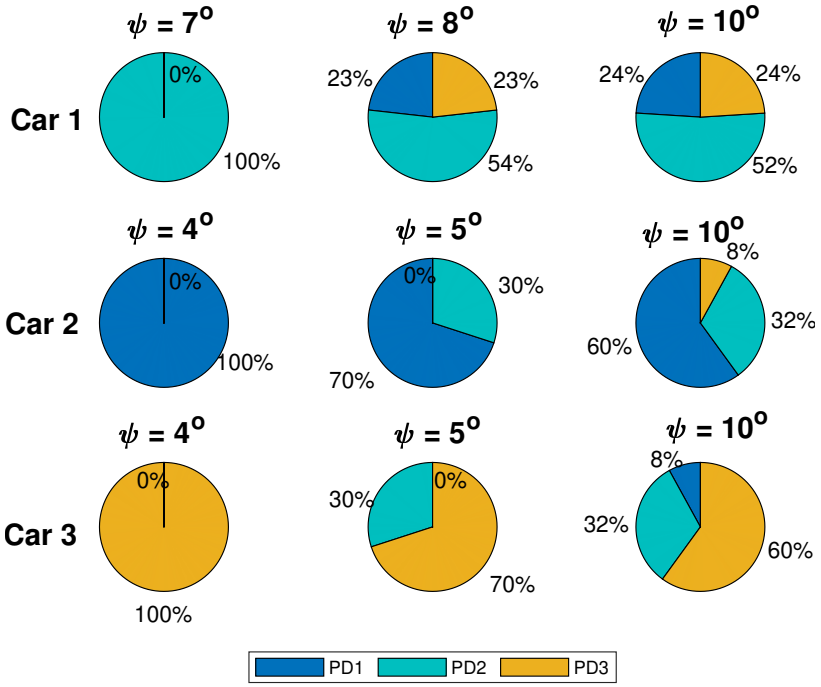

Figure 3.5: PD Contribution for the three cases at different receiver FoV.

Figure 3.5 presents the pie chart of the individual contribution of each PD at different receiver FoVs. Also, Table 3.2 shows the power received by each PD_j (i.e., PD1, PD2, and PD3), P_{r_1}, P_{r_2}, P_{r_3}, at different FoVs. We consider d = 20 m, B = 1 MHz, and D_R = 1 cm.

For the perfect alignment case (i.e., Car 1), it is observed that the total optical power is collected by PD2 at receiver FoVs of $\psi = 7°$. This is due to the proper alignment between the PD2 and Car 1. As the FoV increases, the contribution of PD1 and PD3 are more pronounced. For example, consider $\psi = 7°$. The PD2 can gather a total power of P_{r_2} = 11.23 dBm (see Table 3.2) with a percentage of 100% while PD1 and PD3 cannot receive any power (i.e., 0%). Also, consider $\psi = 8°$. The contributions of PD1, PD2, and PD3 are given as 23%, 54%, and 23% with a total received power of 6.5 dBm, 10.07 dBm, and 6.5 dBm, respectively. As an example from the practical industries, we can mention the PD: BPY 62 from OSRAM [92] whose half FoV is of the order of 8°.

For the case of Car 2 (located on the left-hand side), the total power is received by PD1 for receiver FoVs of $\psi = 4°$. This is due to its orientation on the side of Car 1 (left side). As the FoV increases to 5°, the contribution of PD2 increases. For a further increase in receiver FoV up to 10°, the contribution of PD3 is pronounced. For example, consider $\psi = 4°$. PD1 collects a total power of P_{r_1} = 13.3 dBm with a percentage of 100%, while PD2 and PD3 do not contribute (i.e. 0%). Also, consider $\psi = 5°$. The contribution of PD1, PD2, and PD3 are given as 70%, 30%, and 0%, respectively. When the FoV reaches 10 °, the contributions of PD1, PD2, and PD3 are respectively 60%, 32%, and 8% with corresponding powers of P_{r_1} = 7.7 dBm, P_{r_2} = 5.1 dBm, and P_{r_3} = -1.18 dBm.

As practical examples, we can find the models of SFH 213 from OSRAM [93] which has a half FoV in the order of 10°.

In the case of Car 3 (located on the right side) and considering $\psi = 4°$, It is observed that PD3 collects the total power since it is oriented on the same side as Car 3 (i.e., on the right side). The contribution of PD2 appeared with increasing FoV up to 5°. At $\psi = 10°$the contribution of PD1 is more pronounced. For example, consider $\psi = 4°$. PD3 collects a total power of $P_{r_3} = 13.3$ dBm (i.e., 100%), while PD2 and PD3 have no contribution (i.e., 0%). Furthermore, consider $\psi = 5°$. The contributions of PD2 and PD3 are 30% and 70% with corresponding powers of $P_{r_2} = 10$ dBm and $P_{r_3} = 13.7$ dBm, respectively. Also, consider $\psi = 10°$. The contributions of PD1, PD2 and PD3 are given respectively as 8%, 32%, and 60% with corresponding powers of P_{r_1} = -1.18 dBm, P_{r_2} = 5.1 dBm, and P_{r_3} = 7.7 dBm. Therefore, from the real industries we can find the PD model of SFH 213 FA from OSRAM [94] that operate in the half FoV order of 10°.

Impact of Bandwidth (B)

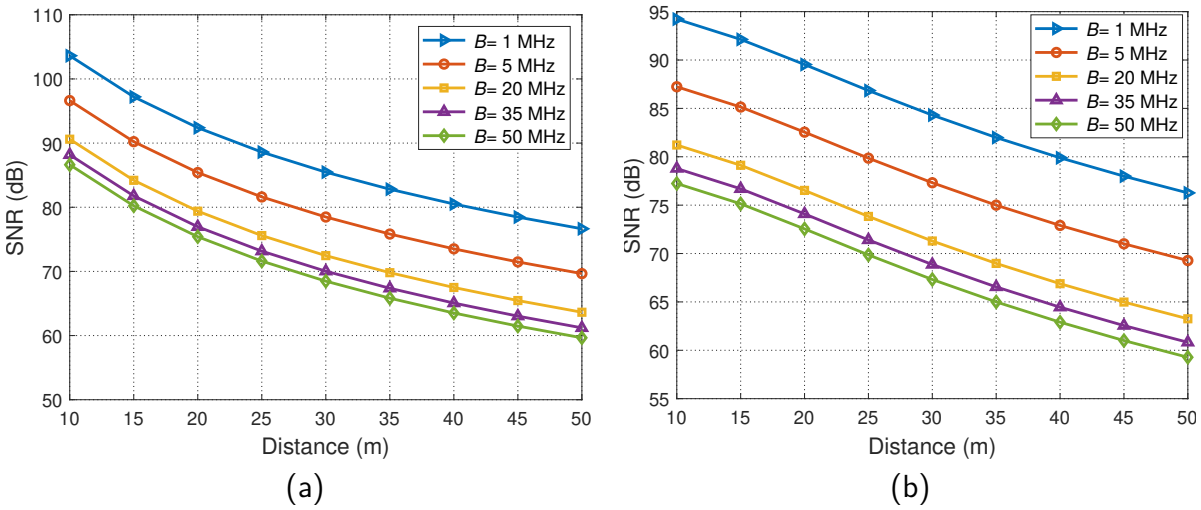

Figure 3.6: SNR versus distance for different bandwidths (a) Car 1 (b) Car 2 and Car 3.

In Figure 3.6, we present the achievable SNR versus inter-vehicle distance for a range of system bandwidths (i.e., B = 1MHz - 50MHz). We assume that $N = 3$ and the receiver FoV and aperture diameter are fixed to $\psi = 20°$and $D_R = 1$ cm, respectively. It is observed that the system bandwidth has a noticeable impact on the SNR performance. Thus, increasing the system bandwidth decreases the SNR for both perfect alignments (see Figure 3.6a) and imperfect alignment (see Figure 3.6b) cases. This is due to the fact that the higher bandwidth the greater the noise variance. For example, consider $d = 10$ m. The highest SNR values, i.e. 103.6 dB, 94 dB, and 94 dB are observed at $B = 1$ MHz for the three cases under consideration (i.e., Car 1, Car 2, and Car 3), respectively. While

the lowest values of 86.6 dB, 77 dB, and 77 dB are found at 50 MHz bandwidth for Car 1, Car 2, and Car 3 cases, respectively.

Impact of Receiver Aperture Diameter (D_R)

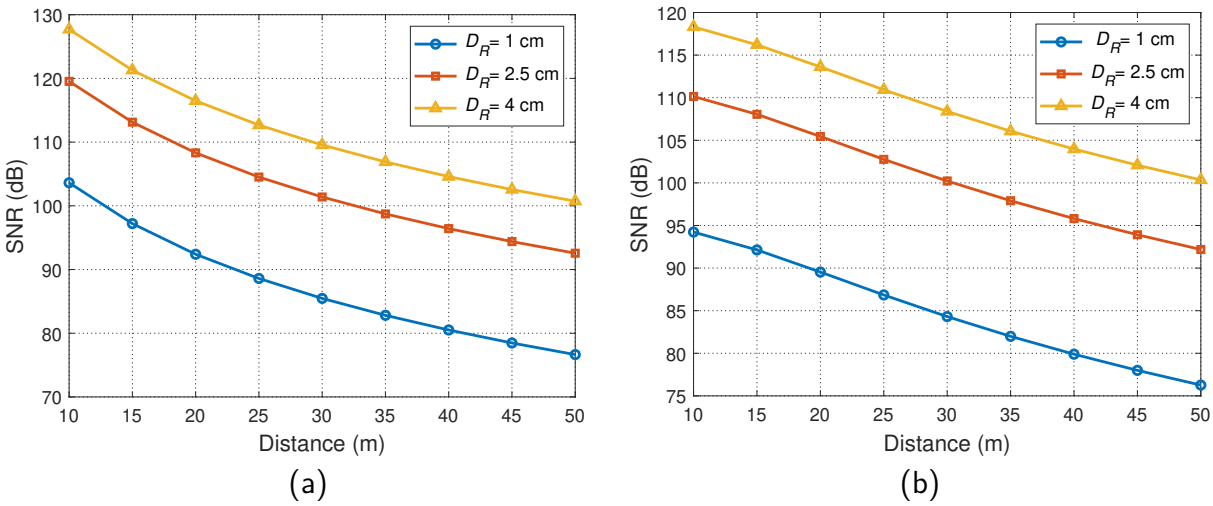

Figure 3.7: SNR versus distance for different PD aperture diameters for (a) Car 1 (b) Car 2 and Car 3.

Figure 3.7 depicts the SNR as a function of inter-vehicle distance for different receiver diameters (i.e., $D_R = 1$ cm, $D_R = 2.5$ cm, and $D_R = 4$ cm). The receiver FoV angles and the bandwidth are fixed to $\psi = 20°$ and $B = 1$ MHz, respectively. As expected, the SNR increases as the receiver diameter increases. In other words, for an increased receiver size, the maximum light intensity captured by the receiver increases. For example, consider $d = 10$ m and the perfect alignment case. The SNR values are given as 103.6 dB, 119.5 dB, and 127.6 dB for $D_R = 1$ cm, $D_R = 2.5$ cm, and $D_R = 4$ cm, respectively. Likewise, for the imperfect alignment case, the SNR values are given as 94 dB, 110 dB, and 118 dB for $D_R = 1$ cm, $D_R = 2.5$ cm, and $D_R = 4$ cm, respectively.

Channel Capacity

In this section, we present the achievable data rate based on Eq. (3.11) as a function of inter-vehicle distance for the three scenarios under consideration. We assume $B = 5$ MHz and $\psi = 20°$. It can be observed from Figure 3.8 that the data rate decreases with increasing the inter-vehicle distance. This is due to the strong attenuation of the light transmitted through the air. For example, consider Car 1 case and $N = 3$. The achieved data rate is 85 Mb/s for $d = 10$ m. This reduces to 70 Mb/s and 63 Mb/s for $d = 30$ m and $d = 50$ m, respectively. It is also observed a significant enhancement in the data rate as the number of the adopted PDs increases. For example, consider Car 2 and Car 3 cases and $d = 10$ m. The obtained data rate is given as 69 Mb/s for $N = 1$. This climbs

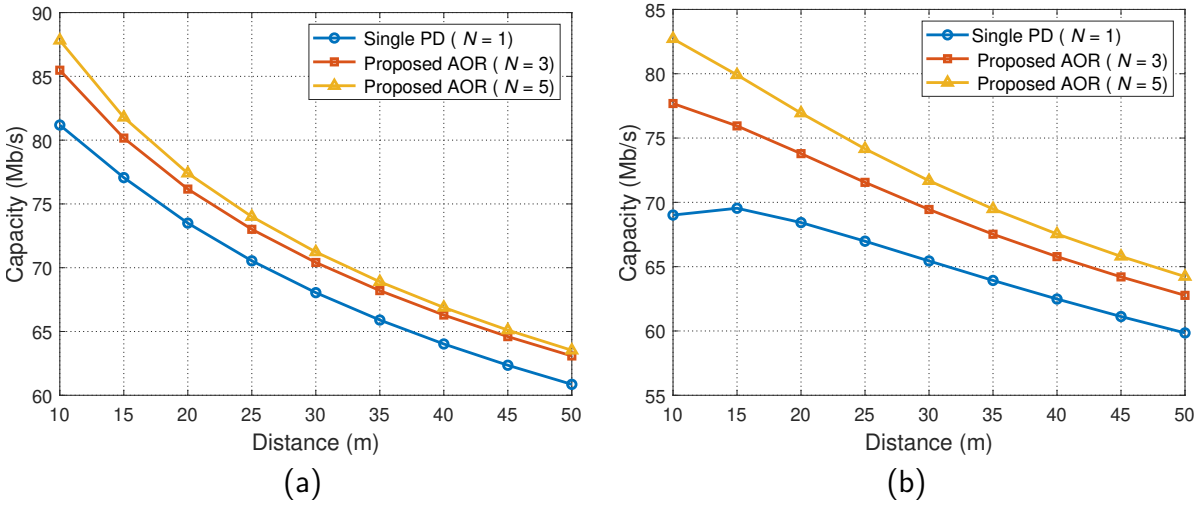

Figure 3.8: Achievable data rate versus distance for the cases of 1PD, 3PDs and 5PDs. (a) Car 1 (b) Car 2 and Car 3.

to 77 Mb/s and 83 Mb/s for $N = 3$, and $N = 5$, respectively. Likewise, consider Car 1 case. The achievable data rates are given as 81 Mb/s, 85 Mb/s, and 88 Mb/s for $N = 1$, $N = 3$, and $N = 5$, respectively. One can notice that the gap in the capacity at different receiver cases is also changed with the communication distance. For instance, consider the imperfect alignment scenario. The gap between single receiver (i.e., $N = 1$) and proposed AOR (i.e., $N = 3$) is 8 Mb/s. This increases to 14 Mb/s for $N = 5$ with respect to the single receiver. Increasing the data rate due to the deployment of the proposed AOR can ensure not only the transmission of different public safety messages, but also support other entertainment applications like video transmission for example. Besides capacity, our proposed AOR is also expected to increase vehicular communications coverage.

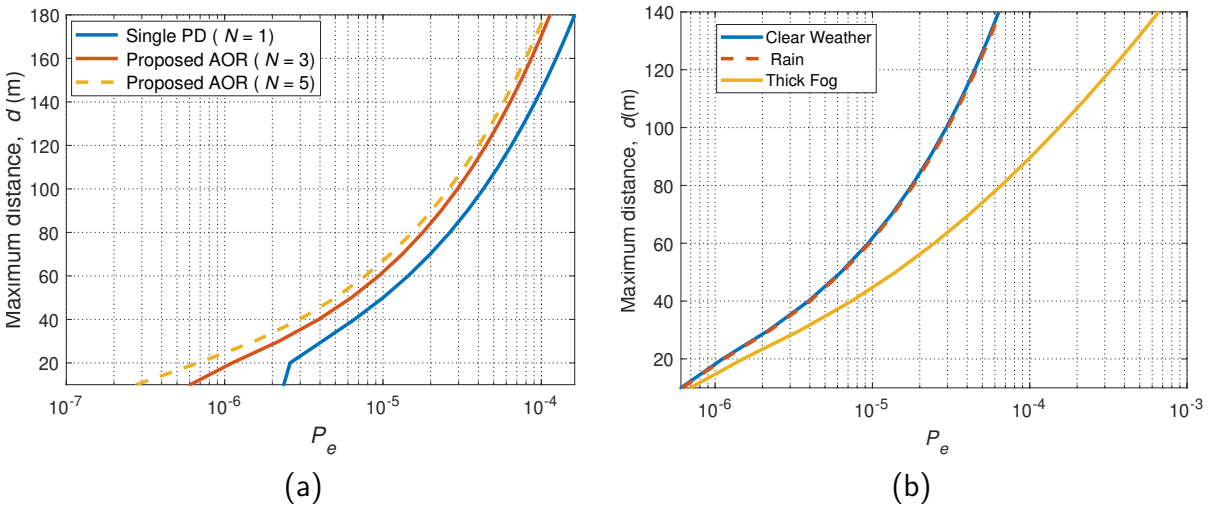

Figure 3.9: Maximum achievable distance versus BER for (a) different receiver numbers (b) different weather conditions.

Achievable Distance

In this section, we present the results of the maximum achievable distance of the V2V-VLC system under consideration. To do so, we make a comparison between a V2V-VLC system with a single receiver ($N = 1$) and a system with an AOR receiver with N PD, where $N = 3$ and $N = 5$. Figure 3.9a shows the maximum achievable distance for different numbers of PDs while satisfying a target BER assuming the imperfect alignment scenario (i.e., Car 2 and Car 3). We assume $B = 1$ MHz, $D_R = 1$ cm, and $\psi = 20°$. It is observed a significant improvement in the maximum distance as the number of deployed PDs increases. This is due to the increase in the amount of captured light emitted by the transmitters when the number of receivers increases. For example, consider a target BER of $P_e = 10^{-5}$. The maximum distance for $N = 1$ (i.e., single receiver) is given as $d = 50$ m. While with the proposed AOR deployment the transmission distance jumps to 60 m and 67 m for $N = 3$ and $N = 5$, respectively. Thus, it is clear that the proposed AOR can extend the communication distance by 17 m while ensuring the same connectivity quality of $P_e = 10^{-5}$.

It should be noted that when the distance between Car 4 and Car 2/3 becomes too tiny, the inter-communication might be too difficult or even impossible. This distance depends on the PD FoV (ψ) and the incident angle (θ).

Figure 3.9b presents the maximum attainable distance while satisfying a target BER for different weather conditions assuming the imperfect alignment scenario (i.e., Car 2 and Car 3). We assume $N = 3$, $B = 1$ MHz, $D_R = 1$ cm, and $\psi = 20°$. It is observed that the rainy weather has a small effect on the maximum transmission distance. In contrast, thick fog has a significant impact on the transmission distance. This is due to the relatively high density of water drops in fog, which reduces the amount of photons received by the receiver. For example, consider a target BER of $P_e = 10^{-6}$. The maximum distance for clear weather is given as $d = 19$ m. This reduces to $d = 18$ m and $d = 15$ m for rain and thick fog, respectively. To illustrate the effectiveness of the proposed AOR, we performed a comparison with existing works in the literature. It is observed from [95, 96] that the achieved distance for a target BER of 10^{-5} is 55 m for a single receiver. Similarly, in [97] the maximum distance reached for a target BER of 10^{-5} is 69 m. Also, [98] can obtain a maximum distance of 30 m for a target BER of 10^{-5}. The difference between these values is due to the differences in the measurement setup same as the modulation type. In our work, the maximum distance value is recorded as 50 m (see Figure 3.9), which is further improved by 17 m when our proposed AOR is deployed.

Packet Delivery Ratio (PDR)

In this section, we investigate the performance of the V2V VLC system in terms of PDR for different receiver numbers. We assume $B = 5$ MHz, $D_R = 1$ cm, and $\psi = 20°$.

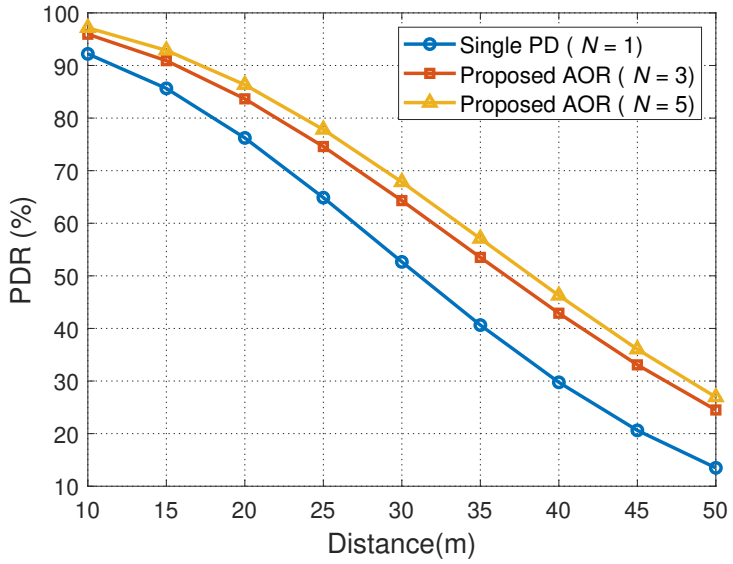

Figure 3.10: Packet delivery ratio versus distance for the cases of 1PD, 3PDs and 5PDs.

Figure 3.10 shows the probability of reception of packets transmitted by the headlight versus inter-vehicle distance for single receiver and AOR receiver ($N = 3$ and $N = 5$) cases. It can be observed from Figure 3.10 that the PDR worsens with increasing inter-vehicle distance. This is due to the strong attenuation of the light transmitted through the free space. For example, consider $N = 3$. A 90% of PDR can be obtained up to 15 m of longitudinal distance. This reduces to 65% and 24% for $d = 30$ m and $d = 50$ m, respectively. It is also observed that the transmission quality increases with the number of PDs. For example, consider $d = 25$ m. A 65% of PDR can be obtained by the single receiver case (i.e., $N = 1$). This increases to 75% and 79% for $N = 3$ and $N = 5$, respectively. It is clear that the proposed AOR with 5 PDs can improve the system quality by 14%. Thus, for wider roads, the AOR with more PDs with specific orientations and careful design can ensure higher quality of service (QoS), which is highly required by autonomous vehicle systems.

3.3 V2I VLC Link

3.3.1 System and Channel Model

As illustrated in Figure 3.11a, we consider a V2I-VLC scenario in a three-lane road with a width of W_l. We assume that three vehicles are placed in the center of each lane and separated from each other by a horizontal shift of d_y. Each of these vehicles approaches to the traffic lights pole with a separation distance of d_x. The two LED headlamps of each vehicle are adopted as wireless transmitters. On the receiver side, the traffic light located in the center lane at a height of d_z uses an Angle Diversity Receiver (ADR) with

three PDs to extract the data, as seen in Figure 3.11b. For channel modeling, we applied the non- sequential ray tracing features of OpticStudio simulator, described in Chapter 2.

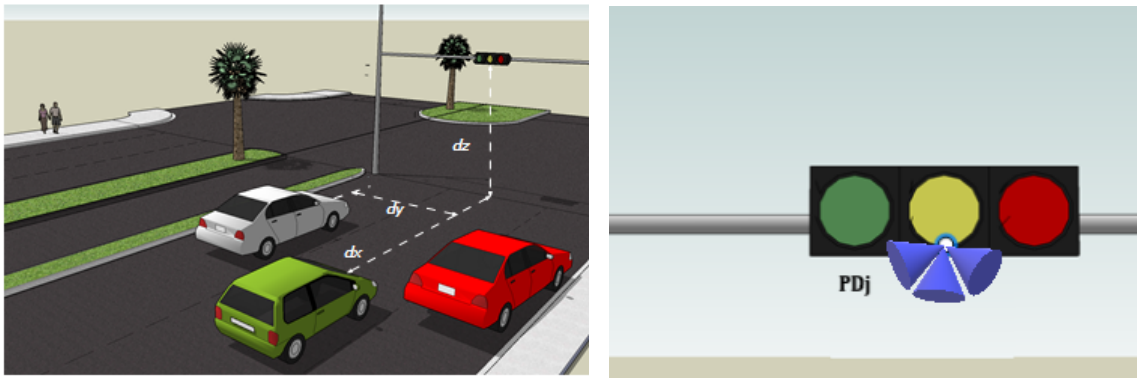

(a) (b)

Figure 3.11: (a) V2I system under consideration (b) Location of ADR receiver

In the following, we explain the proposed receiver design.

3.3.2 Receiver Model

Single Photo-detector

Generally, there are various receiver configuration types in vehicular VLC systems. A single-element detector with a wide FOV is the most widely used. The deployment of the wide FOV detector enables enhanced optical signal collection. However, huge amounts of unwanted ambient light, as in the case of direct sunlight, can also be received at an average power much higher than the required signal. In fact, it is very difficult to minimize it, even with an optical filter [99]. This reduces the signal-to-noise ratio.

ADR Receiver

Contrary to the single photo-detector receiver with a large FOV, an ADR exploits the fact that the target signal typically comes from different angles than the unwanted noise. The basic idea of the ADR is the use of multi-photodetectors (N PDs) that are pointed in different directions with different incidence angles and normal unit vectors, resulting in uncorrelated VLC channels. The narrow FOVs of these photo-detectors are intended to limit the background noise and the Co-Channel Interference (CCI).

In order to improve the system performance, it is necessary to select one of the previously discussed PD distributions. In this work, we consider the pyramid receiver which is simple and practically feasible. This distribution is referred to as pyramid since the PDs point in the directions of the normal vector of the pyramid triangular side faces, leaving the base for placement on traffic lights pole surface as we can observe in Figure 3.12a. However, it is not necessary for the physical shape of the receiver to look like a pyramid.

The N PDs are placed in the center of the side faces of the pyramid and organized uniformly in a circle of radius r_p in the horizontal plane, as shown in Figure 3.12a. So their coordinates will be defined by the hybridization of Cartesian, (x, y, z), and spherical, (α, β), coordinates. In other words, the normal vector $\boldsymbol{n}_{PD}^{j}$ of the j^{th} PD located at (x_j, y_j, z_j) is given by [100, 101]:

$$\boldsymbol{n}_{PD}^{j} = (x_j, y_j, z_j, \alpha_j, \beta_j) \quad \text{for } 1 \leq j \leq N \tag{3.17}$$

where α_j is the angle taken with respect to the positive z-axis, which calls the elevation angle with $\alpha \in [0, \pi]$; and β_j, the azimuth angle is the angle taken from the positive x-axis with $\beta \in [0, 2\pi]$.

Moreover, in order to describe the PDs orientation in the ADR, following the geometry of the pyramid. We assume that the elevation angles of all PDs are equal and identical to the elevation angle of each side of the pyramid. Therefore, $\alpha_j = \alpha_{PR}$, $\forall j \in [1, N]$, where α_{PR} is the elevation angle of the pyramid side. Besides, azimuth angles are symmetrically aligned and uniformly distributed according to the equation below [102]:

$$\beta_j = \frac{2\pi(j-1)}{N}. \tag{3.18}$$

Moreover, considering the center of the pyramid as a reference point, the coordinates of the j^{th} PD on the ADR are given by the following equation [102, 101]:

$$(x_{PD}^{j}, y_{PD}^{j}, z_{PD}^{j}) = (x_{PD_0} + r_p \cos\beta_j, y_{PD_0} + r_p \sin\beta_j, z_{PD_0}) \tag{3.19}$$

where (x_{PD_0} and y_{PD_0}) are the coordinates measured from the center of the pyramid, whereas z_{PD_0} is the ADR height and it can be given as $z_{PD_0} = \cos(\alpha_j)$ (see Figure 3.12b).

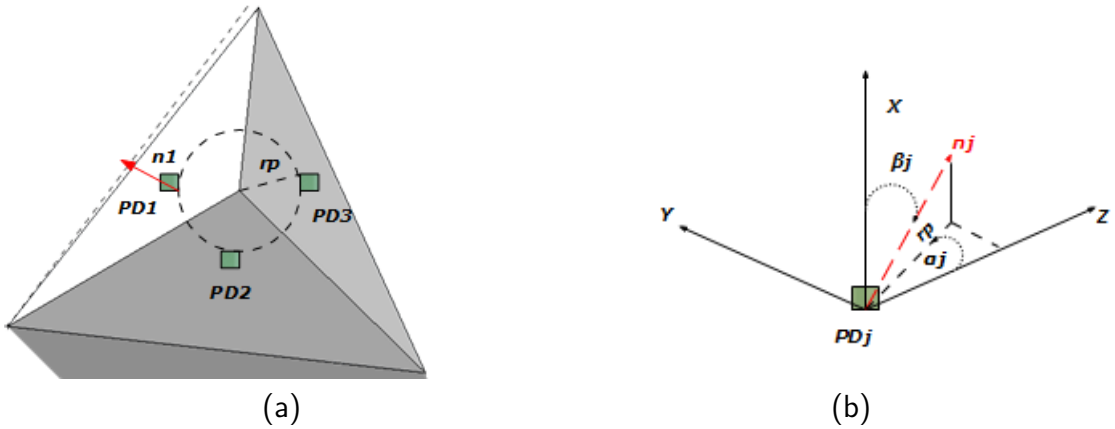

(a) (b)

Figure 3.12: General structure of the ADR receiver. (a) Top view (b) PDs coordinates.

The relation between α_j and PDj, as seen in Figure 3.12b, can be given by $r_p =$

$\sin(\alpha_j)$. Thus, the coordinate of the j^{th} PD on the ADR as a function of the orientation angles can be expressed as follows:

$$\begin{aligned}&\left(x_{PD}^{j}, y_{PD}^{j}, z_{PD}^{j}\right) = \\ &\left(x_{PD_0} + \sin(\alpha_j)\cos\left(\tfrac{2\pi(j-1)}{N}\right), y_{PD_0} + \sin(\alpha_j)\sin\left(\tfrac{2\pi(j-1)}{N}\right), \cos(\alpha_j)\right)\end{aligned} \tag{3.20}$$

3.3.3 Performance Analysis

In this section, we analyze the error rate performance of our proposed model. We consider the Signal-to-Noise Ratio (SNR) and the achievable data rate as performance metrics. Such parameters allow the assessment of the capacity and the efficiency of the V2I-VLC channel. The Shannon channel capacity for the j^{th} PD is defined in [103] as follows:

$$C^{[j]} = \log_2\left(1 + SNR^{[j]}\right) \tag{3.21}$$

where $SNR^{[j]}$ is the SNR of the j^{th} PD. Furthermore, for each i^{th} transmitter, the SNR at the j^{th} PD can be given by:

$$SNR_{i,j} = \sum_{l=1}^{3} \frac{\left(RP_{opt}H_{i,j}\right)^2}{\sigma_t^2} \tag{3.22}$$

where R, P_{opt}, and $H_{i,j}$ are the photodetectors responsivity, the average transmitted power, and the channel Direct Current (DC) gain, respectively. Also, σ_t^2 is the total noise variance. The main sources of noise are the background noise, σ_{back}^2 and the internal receiver noise including thermal noise σ_{ther}^2 and shot noise σ_{shot}^2. Thus, the total noise power can be determined as:

$$\sigma_t^2 = \sigma_{back}^2 + \sigma_{ther}^2 + \sigma_{shot}^2 \tag{3.23}$$

Therefore, based on Eq. (3.21), we need a better SNR if we want to improve $C^{[j]}$ that will, in turn, directly increase the data rate. Hence, in order to maximize the SNR of the link, the PD must be able to choose among all the Tx of the vehicle scenario the one with the best SNR. Thus, the best LED of the k_j set, T_D where $D \in [1, K_j]$, should be chosen as [102]:

$$T_D^{[j]} = \arg\max_i \left(SNR_i^{[j]}\right) \tag{3.24}$$

where i is the LED index, $SNR_i^{[j]}$ is the SNR between the i^{th} LED and j^{th}PD, which can be established as [102]:

$$SNR_{T_D,j} = \frac{\left(RP_{opt}H_{T_D,j}\right)^2}{\left(n_{R_x}\right)^2}. \tag{3.25}$$

where $H_{T_D,j}$ is the channel DC gain between the desired transmitter T_D and the j^{th} PD. Also, $n_{R_x}^2$ is the additive noise.

Furthermore, since the structure of the ADR consists of several PDs, a single signal must be obtained from the set of the received signals. Hence, signal combining schemes can be used. These techniques are characterized by the selection or combination of several PD-received signals at the ADR receiver into a single output signal.

Select Best Combining Scheme (SBC)

The SBC model was first introduced by [104]. In this model, the SNR of each PD is calculated. However, only the PD with the highest SNR, R_D, is considered to be the output of the ADR. This process allows to achieve the objective of maximizing the SNR given by the following equation:

$$\arg\max_{j} \left(SNR_j\right) \tag{3.26}$$

where the SNR of the link between the T_D and the R_D can be given by [100, 104]:

$$SNR_j^{[T_D,R_D]} = \frac{\left(RP_{opt}H_{T_D,R_D}\right)^2}{\left(\sigma_n\right)^2}. \tag{3.27}$$

In this approach, only the signal received by the PD with the highest SNR will be taken into account by the ADR. Consequently, a circuit that selects and monitors the SNR in every PD is required. However, since only one PD is selected, the combination of signals does not perform.

Equal Gain Combining Scheme (EGC)

The EGC scheme was first proposed in [104]. Unlike the SBC scheme where a single PD that achieves the highest SNR value can be used, the EGC scheme takes advantage of other PDs. It uses the direct sum of all other PD's branch signals with the same weighting, resulting in an increase in the overall received SNR. Therefore, the SNR can be expressed as follow:

$$SNR_{T_D,j} = \frac{\left(RP_{opt}\sum_{j=1}^{N_{PD}}|H_{T_D,j}|\right)^2}{\sum_{j=1}^{N_{PD}}\left(n_{PD_j}\right)^2} \tag{3.28}$$

where $H_{T_D,j}$ is the overall DC gain for the vehicular VLC system. For its physical implementation, it is necessary to perform an adder of the received signal. A simple combination circuit is therefore required. In our study, we adopt the equal gain combining scheme.

3.3.4 Simulation Results and Discussion

In this section, we evaluate the performance of the proposed V2I-VLC system, in comparison with a single PD case [105]. This performance measurement is conducted and analyzed in terms of SNR and data rate metrics. All numerical evaluations are carried out using simulations in Zemax ® and Matlab ® software.

Numerical Parameters

For the analysis of the simulations, we consider a three-lane road with a lane width of $W_l = 3.75m$ [75], where the road type R2 consisting of 60% gravel larger than 10 mm as defined in [106] is considered. We use three cars modeled as CAD objects with dimensions of Audi A8 model [107], where car 1 (green car) moves with perfect alignment with the traffic pole (i.e. $d_y = 0$ (see Figure 3.11a)). While car 2 (white car) and car 3 (red car) move on different lanes with a lateral offset of $d_y = 2m$ from the pole. The headlights of all three cars serve as wireless transmitters. They are intended to provide sufficient road lighting without inducing blindness of other road users and hence have an asymmetrical power distribution. The average optical power of all the LEDs is $P_e = 1W$.

At the receiver side, the traffic light is modeled as CAD objects with a metallic surface coating. The ADR receiver is placed in the traffic pole at a height of h=5.5m [108]. In this study, we consider an ADR receiver with 3 branches, each branch has a PD that covers a different area depending on the azimuth and elevation angles of the ADR faces. Thus, the elevation angles, α_j, of all the photodetectors are fixed at 70 °, 80°, and 90°. Whereas the azimuth angles are set as follows, $\beta_j = 10°$, $\beta_j = 20°$, and $\beta_j = 30°$.

Numerical Results and Discussions

Comparison with Single PD In the following, we evaluate the impact of using ADR on the performance of the V2I system. Toward this, we make a comparison between a V2I-VLC system without ADR (single receiver) and another that has an ADR receiver. To make a one-to-one comparison, we assume the following assumptions for the two scenarios: β=10°, α= 45°, B = 1 MHz, and D_R = 1 cm. Figure 3.13 presents the received power versus the inter-vehicle distance for two scenarios: Without ADR and With ADR. It is observed a significant improvement in received power in the ADR case compared to the single receiver. This is due to the ability of ADR to collect rays from different directions. For example, consider d= 20 m and the ADR case. The maximum received power is -56.2 dB, with an improvement of 4.8 dB compared to single receiver case.

Effect of Elevation angle

In this section, we investigate the effect of varying the elevation angle, α_j of the ADR receiver on the system performance. We assume α_j= 45°, 60°, and 75°. Figure 3.14

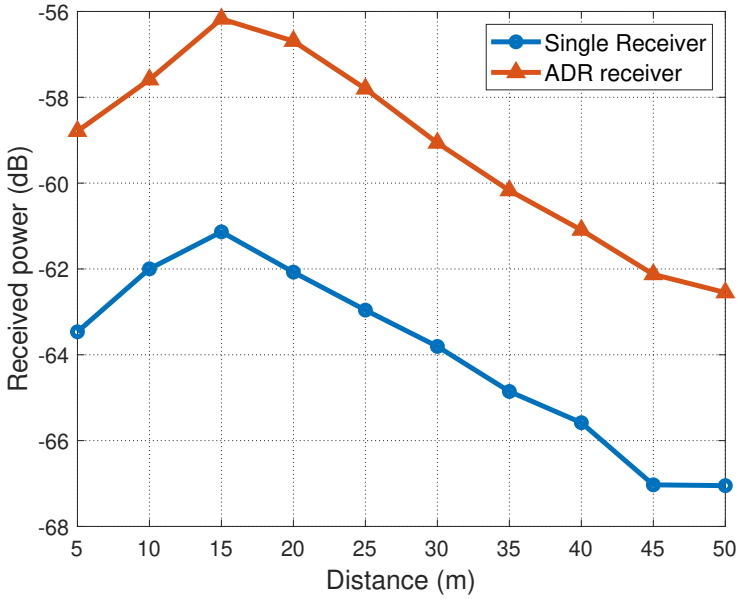

Figure 3.13: Received power versus distance for different receivers numbers.

revealed the received power versus distances at different elevation angles for the three scenarios under consideration. The azimuth angle is fixed to 10°and the distance between the transmitter and the receiver is varied from 5m to 50m. For perfect alignment scenario, i.e. Car1, as indicated in Figure 3.14a the received power first increases with the distance until it reaches the maximum value at a distance of 15m. Then, it decreases significantly by increasing the distance. It is also observed that at a distance between 5 and 8 m, the elevation angle of 45°gives the highest results. While for a distance varies from 9m to 12m the angle of elevation of 60‘°represents the best results. Finally, at distances greater than 13 m the angle of 75°is the best. For example, consider d= 5 m. The received power is set to -58.7 dB for α= 45°. This decreases to -59.3 dB and -59.5 dB for α= 60°and α= 75°, respectively.

Likewise for imperfect alignment scenario, i.e. Car2 and Car3, The 45°elevation angle achieves the highest results at short distance of 5 m. While the angle of elevation of 60°gives the best outcome for a distance ranging from 7 m to 10m. Also, the 75°angle is optimal for distances more than 10 m. For example, consider d= 20 m. The total received powers are -57.3 dB, -56.8 dB, and -56.7 dB for α= 45°, 60°and α= 75°, respectively. In summary, the small elevation angle is required for shorter distance. While the higher one is for the longueur distances.

Achievable Data rate

Figure 3.15 present the achievable data rate versus distance for three scenarios under consideration. It is observed that the data rate decreases with increasing distance. For example, consider d= 15 m and Car1 case. The maximum achievable data rate is 4.7

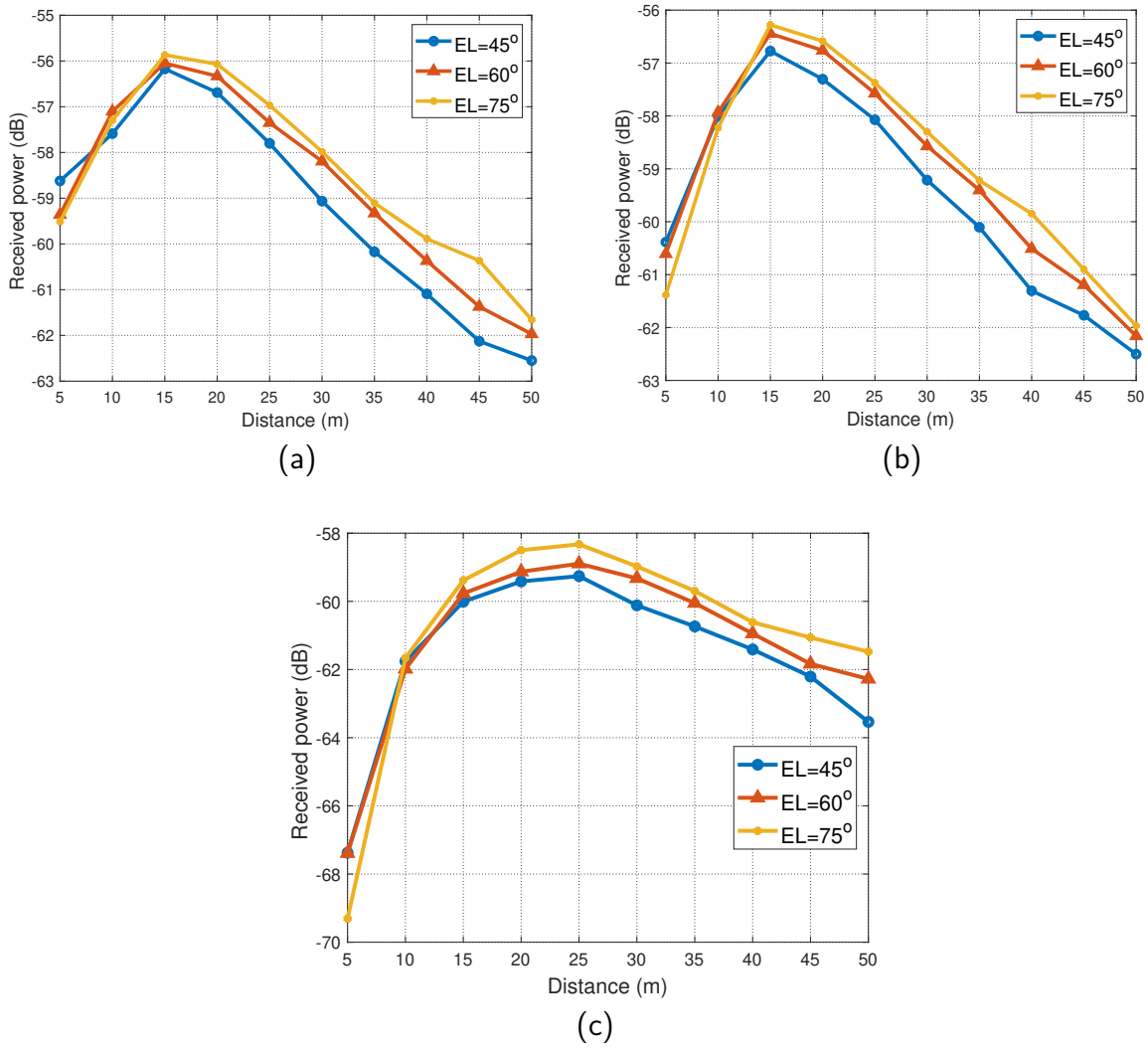

Figure 3.14: The received power versus distance for different elevation angles (a) Car1 (b) Car2 (c) Car3

Mbit/s. This reduces to 3.4 Mbit/s and 2.8 Mbit/s for d= 35 m and d= 45 m, respectively. It is also observed from figure 3.15 that the lateral offset has a significant effect on the data rate, especially at short distances. This effect is reduced as the distance increases. This is due to the change in the angle of arrival at the receiver with the lateral offset. For example, consider a short distance of d= 15 m. The maximum achievable data rate is set to 4.7 Mbit/s for perfect alignment case (Car1). This reduces to 4.5 Mbit/s and 3.5 Mbit/s for Car2 and Car3 (imperfect alignment cases), respectively. Also, consider large distance of d= 40m, the achievable data rates are 3.1 Mbit/s, 3.2 Mbit/s, and 3 Mbit/s for Car1, Car2, and Car3, respectively.

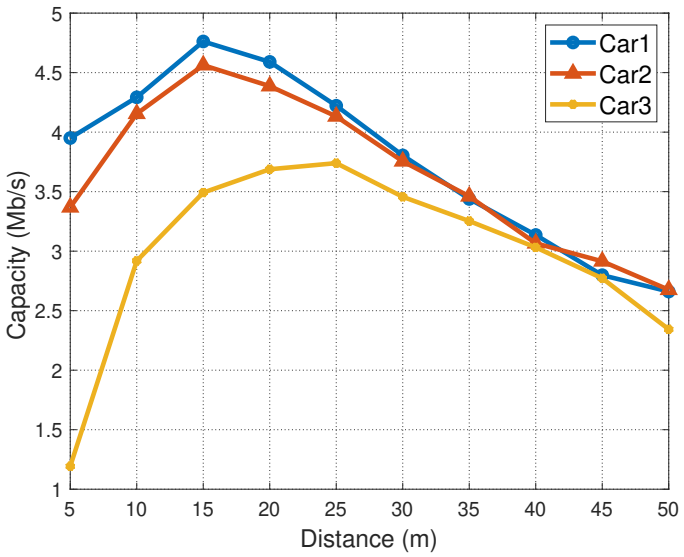

Figure 3.15: achievable data rate versus distance for three scenarios under consideration.

3.4 Conclusion

In this chapter, we adopted the non-sequential ray tracing approach to model the VLC channel. We studied the performance of the V2V-VLC and V2I-VLC system on a typical three-lane road using an angle diversity receiver. By taking different locations of the car within the road, the impact of the different system parameters such as the receiver FoV, the receiver aperture diameter, the elevation angle, and the modulation bandwidth has been investigated. A comprehensive performance comparison is then conducted in terms of achieved data rates, maximum achievable distance, and packet delivery ratio for different numbers of PDs.

In the following chapter, we will present another receiver structure to improve the performance of a V2V-VLC system. A comprehensive performance comparison is then conducted in terms of received power and packet error ratio.

CHAPTER 4

ENHANCEMENT OF VVLC USING SPHERICAL DETECTOR AND CUSTOM LENS COMBINATIONS

4.1 Introduction

As mentioned in chapter 3, most of recent research in the literature has been conducted in static conditions where the transmitter and receiver are in a straight line [72, 74, 75]. However, in real applications, the angle of the incident light and the distance between the transmitter and the receiver are usually variables. An effort to address this issue using multiple PDs is presented in [78, 81]. For instance, in the work of Cui et al. [81], three PDs were used and the one with the highest received power was selected. Also, in [78] four PDs were deployed to prevent interruptions in a V2V-VLC system when changing lanes in a two-lane road. Nevertheless, they cannot cover all directions and the receiver still has a limited view. In the previous chapter 3, we utilize an Angle Oriented Receivers to overcome these limitations [109, 110]. However, while this arrangement provides diversity and thus enhances data rates, it is bulky and difficult to scale [111]. Therefore, a more efficient solution is needed. Thus, an imaging receiver has been proposed. It consists of an array of PDs and a lens that can collect and focus light from a wide angle to a small receiving area. This can ensure a large collection of lights and hence improve the performance. Generally, different kinds of lenses can be used i.e. hemispherical, convex, and fisheye lenses. The imaging receiver is considered as a viable option to mitigate the impact of inter-symbol interference (ISI) and ensure the mobility of the VLC system. It was applied for the first time in indoor environments to improve the performance of the Multiple-Input Multiple-Output (MIMO) VLC system and reduce the channel correlation [111, 112, 113, 114, 115, 116, 117]. For example, in [112] a 68 dB improvement at a Bit Error Rate (BER) of 10^{-5} is demonstrated using a convex lens compared to a non-imaging receiver. The authors in [111, 114, 115] presented a hemispherical lens-based imaging receiver that has a wider field of view (FoV) and can

separate the signal from various LEDs. Also, an imaging receiver scheme based on a fisheye lens was proposed in [116, 117]. It can achieve omni-directional reception with ultra-wide FoV, compact size, and high image quality. However, these scenarios in outdoor environments are still relatively new and need further investigation. Thus, only few works used optics in outdoor applications. For instance, a hemispherical Lens is applied in [118] to improve the performance of a vehicular MIMO-VLC system. Also, in [80], the authors experimentally investigated the effect of the combination of different lenses on a V2V-VLC system. It is expected that the lens has a good effect in the outdoor medium. In this chapter, we investigate the performance of the V2V-VLC system using an imaging receiver with different kinds of optical lenses including Fresnel, aspherical, and combined lenses. The source vehicle uses its two headlamps as transmitters. While the receiver vehicle uses the polar detector instead of multiple PDs to collect rays from more different directions. We perform a channel modeling study based on the non-sequential ray-tracing approach in OpticStudio® (see chapter 2). We first quantify the total received power for the different assumed scenarios considering the asymmetrical radiation pattern of the headlights same as the possibility of both the horizontal and the vertical displacement between the vehicles. We further address the effect of receiver type, lateral shift, receiver diameter, and bandwidth on the performance of the considered systems. Then, the packet delivery ratio for different lateral shifts is also investigated. The remainder of this chapter is organized as follows. In section 5.2, we describe our system model, the different steps of our channel modeling approach, and the design of the optical system model. In section 5.3, we give the performance metrics. Section 5.4 presents the simulation results and discussion. Finally, we conclude in Section 5.5.

4.2 V2V-VLC System and Channel Model

In this section, we explain the system model, the different steps of our channel modeling approach, and the design of the optical system model.

4.2.1 System Model

As illustrated in Figure 4.1, we consider a V2V-VLC system in a two-lane road with a lane width of W. The source vehicle S communicates with the destination vehicle D through its headlamps (denoted by TX1 and TX2) which are separated horizontally by a distance d_c from each other. These car headlights transmit information to the destination vehicle (i.e., D) with an optical power P_t. It should be noted that, unlike the interior LEDs, the vehicle's headlamps have an asymmetrical intensity pattern that is supposed to provide full illumination from the front and sides while minimizing glare to oncoming vehicles and other road users. As an example, Figure 4.2 shows different cross-sections to illustrate the

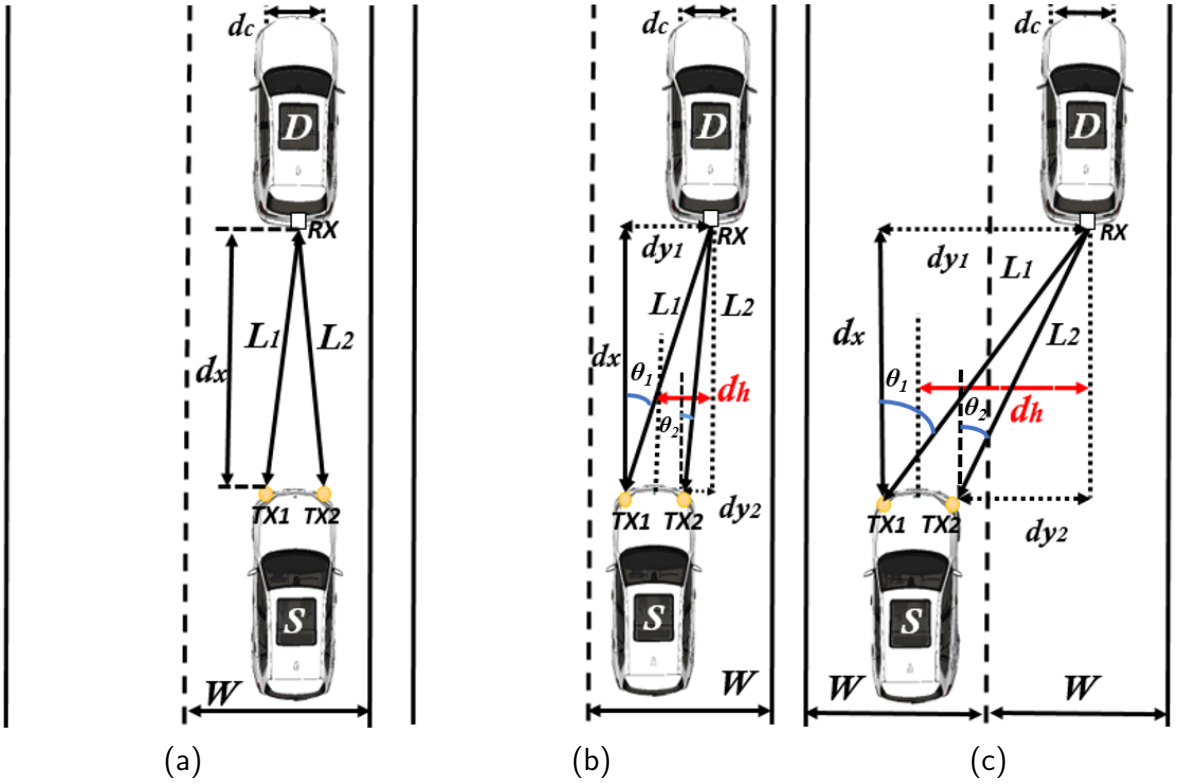

Figure 4.1: V2V-VLC scenarios under consideration.

headlamp's asymmetrical intensity pattern. The blue curve shows the headlight intensity distribution when looking from the side, while the green curve shows the same pattern when looking down from above.

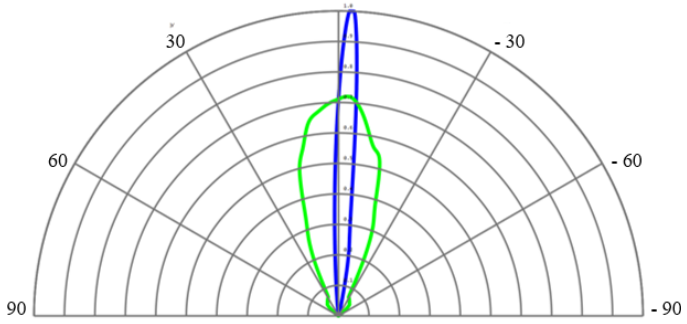

Figure 4.2: Intensity distributions of headlamp at both vertical and horizontal planes.

On the other hand, the vehicle D is equipped with an imaging receiver (PDs and lenses) to focus the light, mounted at its back, at the same height as the headlamps. Generally, one or multiple PDs, installed on the back of the destination car, are used as wireless receivers. As a more alternative to conventional PDs, the polar detector with a radius of r and a responsivity of R can be employed. The polar detector is a spherical-shaped detector that displays radiant intensity data on a polar graph (see Figure 4.3). Its polar angle ranges from 1 to 180 degrees in each cross-section (which forms a complete

sphere) [119], ensuring a large collection of rays from different directions. Thus, it will be more convenient for the mobility of the vehicles. We further define d_x and d_h which represent the vertical and the horizontal distance between S and D.

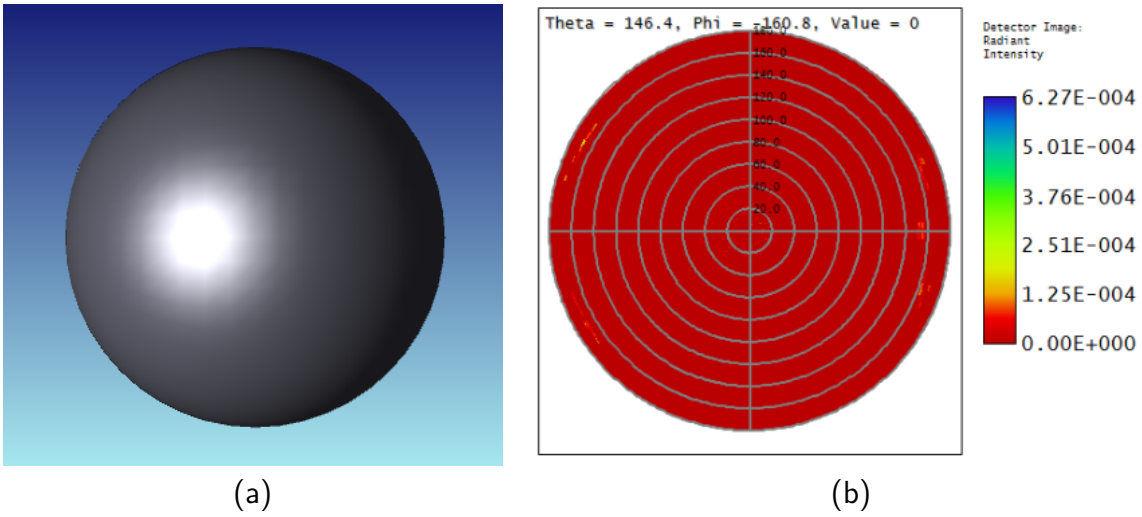

Figure 4.3: (a) 3D polar detector (b) Radiant intensity data

For channel modeling, we adopt the non-sequential ray tracing approach described in chapter 2. Thus, the received power at the detector can be given by [76]

$$Pr = P_t \times G_L \int_0^{\infty} h(t)dt, \tag{4.1}$$

where P_t is the transmitted power, G_L is the gain of the optical lens, and $h(t)$ is the channel impulse responses (CIRs) (see chapter 2). Recently, the authors in [76] proposed a channel gain model for single detector which is given by the following equation

$$H_C = \int_0^{\infty} h(t)dt = \frac{1}{2}\sum_{i=1}^{2}\left(\frac{D_R\,(d_x/L_i)^{1/\varepsilon}}{\zeta L_i}\right)^2, \tag{4.2}$$

where D_R is the receiver diameter, ε and ζ are correction coefficients, and Li denotes the transmission distance between the i^{th} transmitter and the receiver. It can be given by $Li = \sqrt{d_x^2 + d_{y_i}^2}$, where $d_{y_i} = d_h \pm d_c/2$.

In (4.1), G_L is the optical lens gain which is related to the different types of lenses used in the system. In the next section we explain the different types of lenses considered in our system.

4.2.2 Optical System Design

For optical system design, we use the Zemax OpticStudio® 21.2 software to introduce three lens design. The utilized optic design includes Fresnel, aspherical, and the proposed

design, which is a combination of double-convex with half Plano concave lenses, each with its own diameter Dr and focal length f_l. These optics are placed in front of the PD to concentrate the incident light on the sensitive area of the PD. In the following, we present the principle of each of these considered lenses.

Fresnel Lens

Fresnel lens consists of a planar surface on one side and a series of concentric grooves replicated in the plastic on the other side (see Figure 4.4a). These contours are designed to provide a variable deviation angle on the lens surface, bending parallel light rays to a common focal length f_l [120]. Fresnel lenses offer good optical performance at an affordable price, with reduced weight and thickness. Their use in receiver stages has been described in previous work, reporting achievable distances of several meters at 1 kbps in a laboratory prototype [121]. They have also been applied in indoor VLC scenarios, as in [122]. The portion of the light reflected (Fresnel reflection) from the surface of an ordinary dielectric material (such as glass) is given by [123]:

$$R = \frac{1}{2}\left[\frac{\sin^2(\theta-\theta')}{\sin^2(\theta+\theta')} + \frac{\tan^2(\theta-\theta')}{\tan^2(\theta+\theta')}\right], \tag{4.3}$$

where θ and θ' are the angles of incidence and refraction, respectively.

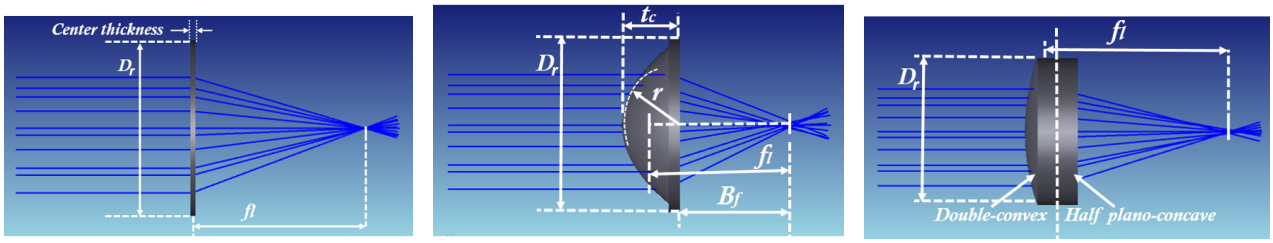

(a) (b) (c)

Figure 4.4: (a) Fresnel Lens (b) Aspherical Condenser Lens (c) Combination of Double-convex with Half Plano-concave

Aspherical Condenser Lens

Unlike the traditional lens with the spherical surface, the aspherical lens has a more complex surface whose curvature changes gradually from the center of the lens to the edge of it. It can be used to focus collimated light (condensation) into a single image element with a short focal length. This lens has an aspheric surface on one side and a plano surface on the other side, as shown in Figure 4.4b. The shape of this lens allows reducing the spherical aberration considerably, even for very low f-numbers. This lens is mainly used in condenser or lighting applications. It is also used when high light gathering power is required, for example for focusing on detectors or fibers.

For a lens with curvature radius of r and refractive index of n, the focal length can be given by [124]:

$$f_l = \frac{r}{n-1}. \tag{4.4}$$

For the non-negligible thickness of the lens, we introduce the distance between the flat surface of the lens and the focal plane of the image, called back focal length (B_f) (see Figure 4.4b). It can be given as follows:

$$B_f = f_l \left[1 - \frac{t_c(n-1)}{n \times r}\right], \tag{4.5}$$

where t_c is the center thickness.

Combined Lens

In contrast to a simple lens, a compound lens is a set of single lenses with a common axis. In our system, we proposed a combination of two lenses kept in contact with each other, which are the double-convex and the half-Plano-concave (see Figure 4.4c). The usage of these multiple lenses allows the correction of more optical aberrations, such as chromatic and spherical aberration. The common focal length f for the resulting optic can be given by [125]:

$$\frac{1}{f_l} = \frac{1}{f1} + \frac{1}{f2}, \tag{4.6}$$

where $f1$ and $f2$ are the focal lengths of the first and second lenses, respectively.

4.3 Performance Metrics

In this section, we analyze the performance of our proposed V2V-VLC model by considering the Packet error rate (PER) as performance metrics, which is given by [126]:

$$\text{PER} = 1 - (1 - P_e)^n, \tag{4.7}$$

where n denotes for the packet length and P_e is the end-to-end BER. For M-ary Pulse-Amplitude Modulation (PAM), P_e is given by [127, Chapter 3]

$$P_e = \frac{(M-1)}{M \log_2(M)} \operatorname{erfc}\left(\sqrt{\frac{3}{2(M-1)(2M-1)}\gamma}\right), \tag{4.8}$$

where $\operatorname{erfc}(x) = \frac{2}{\sqrt{\pi}} \int_x^\infty e^{-t^2} dt$, M is the modulation order, and γ is the signal-to-noise-ratio (SNR), which takes the form of

$$\gamma = \frac{R^2 (P_t H)^2}{\sigma_t^2}, \tag{4.9}$$

where, R denotes the PD responsivity, σ_t^2 is the noise variance, and $H = H_C \times G_L$ is the total channel gain between the car and the receiver. It contains the channel loss H_C (i.e. due to the geometry of transceivers and the propagation through free space) which is given by (4.2) and the gain of the optical lens system (G_L) which depends on the utilized lens system and the incident angle. Thus, by replacing (4.2) in (4.9), γ is written as follows:

$$\gamma = \frac{R^2 \left(\frac{1}{2} P_t G_L \sum_{i=1}^{2} \left(\frac{D_R \left(d_x / \sqrt{d_x^2 + d_{y_i}^2} \right)^{1/\varepsilon}}{\zeta \sqrt{d_x^2 + d_{y_i}^2}} \right)^2 \right)^2}{\sigma_t^2}. \tag{4.10}$$

From (4.10), the final expression of PER is given by (4.11)

$$\text{PER=1-}\left(1 - \left(\frac{(M-1)}{M \log_2(M)} \operatorname{erfc}\left(\sqrt{\frac{3}{2(M-1)(2M-1)} \left(\frac{R^2 \left(\frac{1}{2} P_t G_L \sum_{i=1}^{2} \left(\frac{D_R \left(d_x / \sqrt{d_x^2 + d_{y_i}^2} \right)^{1/\varepsilon}}{\zeta \sqrt{d_x^2 + d_{y_i}^2}} \right)^2 \right)^2}{\sigma_t^2} \right)} \right) \right)^n. \tag{4.11}$$

4.4 Simulation Results and Discussion

4.4.1 Scenarios under consideration

As shown in Figure 4.1, we consider a V2V scenario in a two-lane road, where the source vehicle S communicates with the destination vehicle D, assuming different positions on the road. Specifically, we consider three scenarios:

- **Scenario 1:** We assume that S and D are placed in the center of the same lane and moving in a straight line, where d_h= 0 m (see Figure 4.1a).
- **Scenario 2:** We assume that S and D are moving in the same lane, but there is a misalignment between them which results in a horizontal shift of d_h (see Figure 4.1b).
- **Scenario 3:** We assume that S and D move in neighboring lanes, forming a horizontal offset of d_h (see Figure 4.1c).

Furthermore, we investigate the V2V-VLC system with different receiver types. We assumed to use three different configurations with single PD, multiple PDs (three in this investigation), and a polar detector.

4.4.2 Simulation parameters

In this section, we present the numerical parameters of the V2V-VLC system with the presence of an imaging receiver. We consider a two-lane road with a lane width of W=

Table 4.1: Main Simulation Parameters For V2V System

System parameters	**Values**
Road Parameters	
Type	R2 [106]
Material	Asphalt
Lane width	4 m [128]
Transmitter Parameters	
Light wavelength	400 nm-700 nm
Power, P_t	1 W
Optics Parameters	
Diameter, Dr, for L1, L3 lenses, respectively. Dimension for L2	50 mm, 50 mm 63.5×63.5 mm
Focal length, f_l, for L1, L2, L3 lenses, respectively	35.7 mm, 50.8 mm, 68.6 mm
Receiver Parameters	
Radius, r	10 mm, 15 mm, and 20 mm
Noise parameters	
Bandwidth, B	5 MHz
Noise spectral density, N_0	10^{-21} A^2/Hz

4 m [128]. The road type R2 consisting of 60% gravel larger than 10 mm as defined in [106] is considered. We use a vehicle modeled as a black CAD object with the dimensions of the Audi A8 model [107]. We assume clear weather, $P_t = 1W$ and d_h= 0 m, 1 m, 2 m, 3 m, and 4 m. At the receiver side, we assume the usage of three receivers types: a single detector with responsivity of $R = 0.54$ A/W, three PDs, and a polar detector with a radius of r= 10 mm, 15 mm, and 20 mm. They are placed at the back of the vehicle D at a high of 700 mm. Besides, we utilize three optics placed above the imaging plane. Specifically, we employ three lenses system:

- **L1:** We use a commercial Aspheric Condenser Lens [129] with a Dr= 50 mm, an index of refraction of n= 1.49, and f_l= 35.7 mm.
- **L2:** We use a commercial Fresnel lens [130] with a dimension of 63.5 x 63.5 mm, and a f_l= 50.80 mm.
- **L3:** We use a combined lens with a Dr= 50 mm, and f_l= 68.6 mm.

All simulation parameters are listed in Table 4.1.

4.4.3 Results and discussion

In the following, we first present the received power as a function of distance when considering different receiver diameters, lateral offsets and lens system design for all scenarios.

Then, the PER versus the distance for different lateral shifts and different bandwidths is also investigated.

Received Power Versus Distances

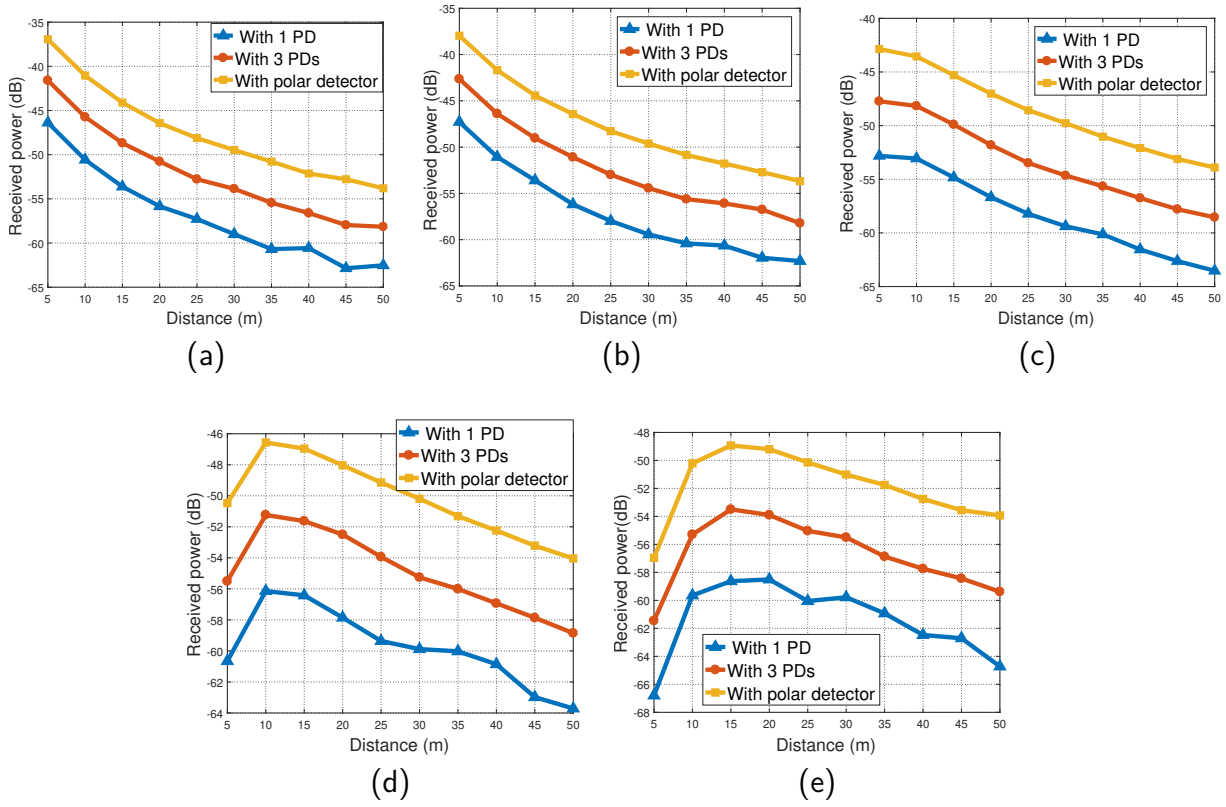

Figure 4.5: Received power for (a) d_h= 0 m (b) d_h= 1 m (c) d_h= 2 m (d) d_h= 3 m (e) d_h= 4 m for single, three, and polar detectors.

In Figure 4.5 we present the received power versus distance for different lateral shifts, d_h = 0, 1, 2, 3, and 4 m. we assumed to use these three different configurations with single PD, multiple PDs (three in this investigation), and a polar detector. Having features of a wide coverage area which enables a better collection of rays from all directions, the optics performance of the polar detector can be better than that for the single and multiple PDs cases. For example, at d_h=0 and d_x= 15 m, the total received power is -44 dB for the case of polar detector. This reduces to -49 dB and -54 dB for the three and single PD cases, respectively. It is also observed from Figure 4.5 that the lateral shift has a severe effect on the received power, particularly at shorter distances. For example, consider the case of a polar detector and d_x= 10 m, the total received power is -41 dB for d_h=0. This reduces to -41.6 dB, -43.5 dB, -46.5 dB, and -50 dB for d_h= 1 m, d_h= 2 m, d_h=3 m, and d_h= 4 m, respectively. When the distance becomes significant large, the effect of lateral offset decreases. This is due to the fact that the angle of arrival at the receiver decreases as the inter-vehicle distance increases, allowing more power to be collected. For example,

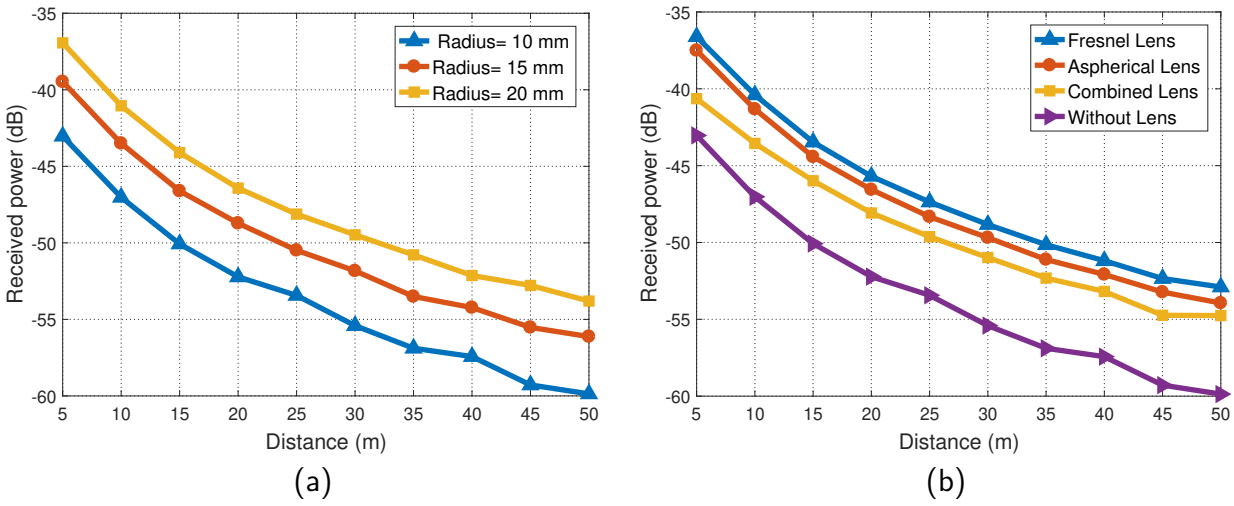

Figure 4.6: Received power for (a) different polar detector radius (without lens) (b) different lens system considering 10 mm radius

consider d_x = 50 m and polar detector case, the total received powers are given as -53.6 dB, -53.8 dB, -53.9 dB, -54 dB, and -53.9 dB for d_h= 0 m, d_h= 1 m, d_h= 2 m, d_h=3 m, and d_h= 4 m, respectively.

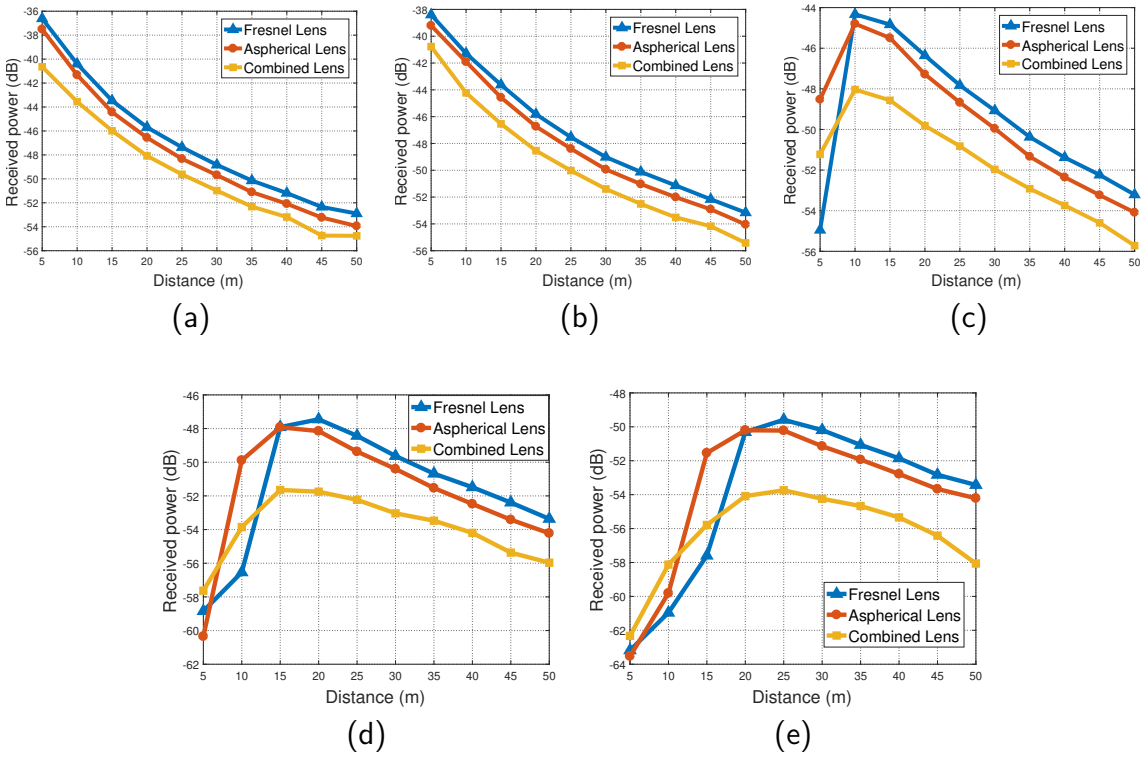

Figure 4.7: Received power for (a) d_h= 0 m (b) d_h= 1 m (c) d_h= 2 m (d) d_h= 3 m (e) d_h= 4 m for a polar detector with a radius of 10 mm.

Figure 4.6a shows the received power as a function of distance, assuming different

polar detector radius (i.e., $r = 10$ mm, $r = 15$ mm, and $r = 20$ mm). We consider that the two cars are perfectly aligned ($d_h = 0$ m) and no lenses are used. It is observed that the total received power increases with the increase of the radius of the polar detector. This is due to the fact that increasing the radius increases the diameter of the detector, which in turn increases the overall detector collection area. Thus, for an increased detector area, the maximum light intensity captured by the receiver increases. This is expected because the intensity captured by the receiver is proportional to its collection area. For example, consider $d_x = 10$ m, the total received power is -47 dB. This claims to -43 dB and -41 dB for $r = 15$ mm and $r = 20$ mm, respectively.

In the following, we evaluate the effect of lens usage on the performance of the V2V system under consideration. Toward this, we perform a comparison between a V2V-VLC system without a lens and the one that has different types of lenses (i.e., Fresnel lens, Aspherical Lens, and combined lens). To make a one-to-one comparison, we assume the following assumptions for all scenarios: $r = 10$ mm, $d_h = 0$ m, and the usage of polar detector.

Figure 4.6b presents the total received power versus distance for all lens design cases. It is observed that the addition of optics in the considered system can improve the performance for both short and long distances. This is due to the ability of the lenses to collect rays from different directions that the detector cannot reach (which means increasing the number of collected rays) and focus them on the PD sensitivity area. For example, consider $d_x = 15$ m and the case of L2 lens. An improvement of 7 dB of the received power is obtained compared to the case without lens. Similarly, improvements of 6 dB and 4 dB are recorded at a distance of $d_x = 10$ m, using the L1 and L3 lenses, respectively, compared to the case without lens.

In the following, we investigate the effect of the lateral shift on the received power for all lens systems under consideration, assuming a radius of r= 10 mm.

In Figure 4.7a, we present the received power versus distances for different lens systems. We assume that the two cars are perfectly aligned (i.e., d_h= 0 m). It is observed that the L2 lens gives good performances for all distances. This is because the L2 lens focuses the rays from the emitter into a single focus, better than the L3 and L1 lenses where the incoming light rays converge at different focal points due to spherical aberration along the optical axis (see Figure 4.4). For example, consider d_x= 10 m and $r = 10$ m, the total received power is recorded as -40 dB using L2 lens. It reduces to -41.3 dB and -43.3 dB for L1 and L3 lenses, respectively.

In Figure 4.7b, we consider the case of misalignment where d_h= 1 m. It is clear that the L2 lens still gives the best results for all distances, resulting in a good performance with an improvement of 1 dB and 3 dB at a distance of d_x= 20 m compared to the case with L1 and L3 lenses, respectively.

Figure 4.7c indicates the total received power versus distance assuming d_h= 2 m. It is

observed that for short distances from 5 m to 9 m, the L1 lens gives good results compared to the other types of lenses (i.e., L2 and L3). Beyond this distance, the L2 lens becomes the best. This behavior is explained by the fact that at short distances and misalignment cases, the incidence angle of transmitted rays is large and the L1 lens has a wide-angle of view (from 1 to 180^o) that is oriented in all directions in contrast to the L2 lens that has a small angle of view. This allows the L1 lens to capture more rays than the L2 lens and the L3 lenses. On the other hand, at long distance, the angle of incidence is reduced, and therefore the L2 lens gives the best performance. For instance, consider a short distance of d_x= 8 m, the received power is 47 dB for the case of L1 lens. This reduces to -49 dB and -50 dB for L2 and L3 lenses cases. Also, consider d_x= 30 m, the total received power is -49 dB for L2 lens, which reduces to -50 dB and -52 dB for L1 and L3 lenses. In Figure 4.7d, we present the received power versus distance, considering d_h= 3 m. It is observed that the better performances are obtained using the L3 lens at a short distance of d_x= 5 m. After that, the L1 lens become the best for a range of distance from 6 m to 15 m. Beyond this distance, the L2 is the best. For example, consider d_x= 5 m, the total received power is -57 dB, -58, and -60 dB for L3, L2, and L1 lenses. Also, consider d_x= 10 m, the received power become -50 dB, -54 dB, and -57 dB for L1, L3, and L2 lenses case, respectively. In addition, consider d_x= 25 m, the received power is given as -48 dB, -49 dB, and -52 for L2, L1, and L3 lenses, respectively.

Figure 4.7e shows the received power versus distance, assuming d_h= 4 m. It is observed that for short distances from 5 m to 10 m, the L3 lens gives the best performance. While for the ranges d_x of 11 m to 20 m, the L1 lens offers the best performance. Beyond that, the L2 lens is the best. In particular, received powers of -58 dB, -59 dB, and -60 dB are obtained at d_x= 10 m using L3, L1, and L2 lenses, respectively. Also, consider d_x= 15 m and the cases of L1, L3 and L2 lenses, the total received powers are -51.5 dB, -55.7 dB, and -57.5 dB, respectively. Finally, for d_x= 30 m, the received powers are -50 dB, -51 dB, and -54 dB using L2, L1, and L3 lenses, respectively.

Packet Error Ratio Versus Distance

In this section, we investigate the PER performance of all considered scenarios. Fig. 4.8 presents the PER versus distance for all scenarios under consideration. We consider d_h = 0 m and r = 10 mm. It is clear that an error-free communication is remarkably achieved up to 15 m for the case without lens. While in the lens case, a remarkable error-free communication is achieved up to 30 m with an improvement of 15 m compared to the case without lens. Beyond that, a degradation of performance is observed. For example, consider d_x = 25 m, the PER is set to 1.5 $\times$ 10^{-7} for the case without lens. While it refers to zero for all considered lens systems.

In the following, we address the effect of lateral shift (i.e., d_h = 0 m, d_h = 2 m, and d_h = 4 m) on the performance of the V2V VLC systems under consideration.

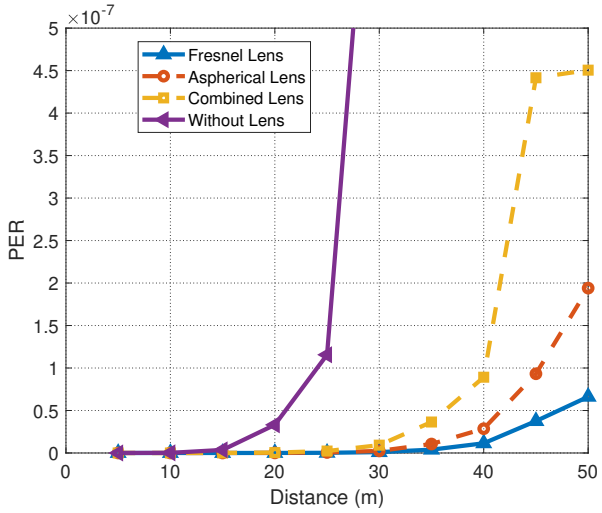

Figure 4.8: PER versus distance for all considered scenarios.

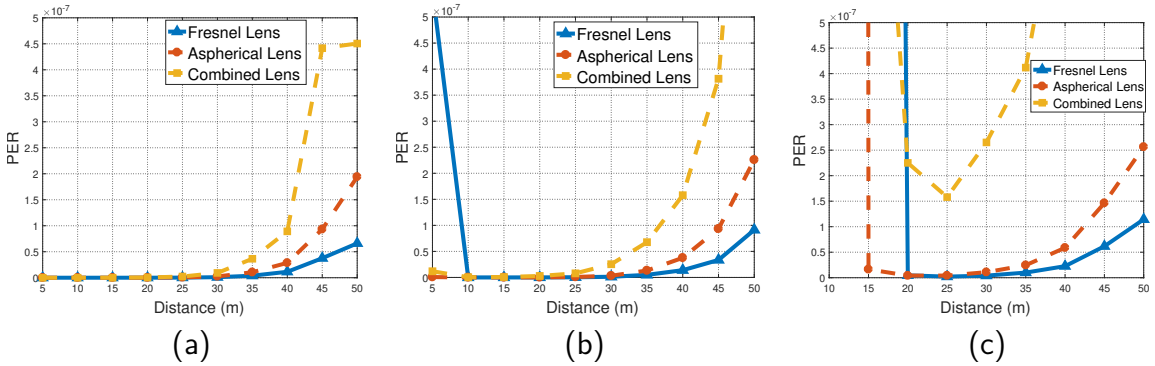

Figure 4.9: PER versus distance for (a) d_h= 0 m (b) d_h= 2 m (c) d_h= 4 m.

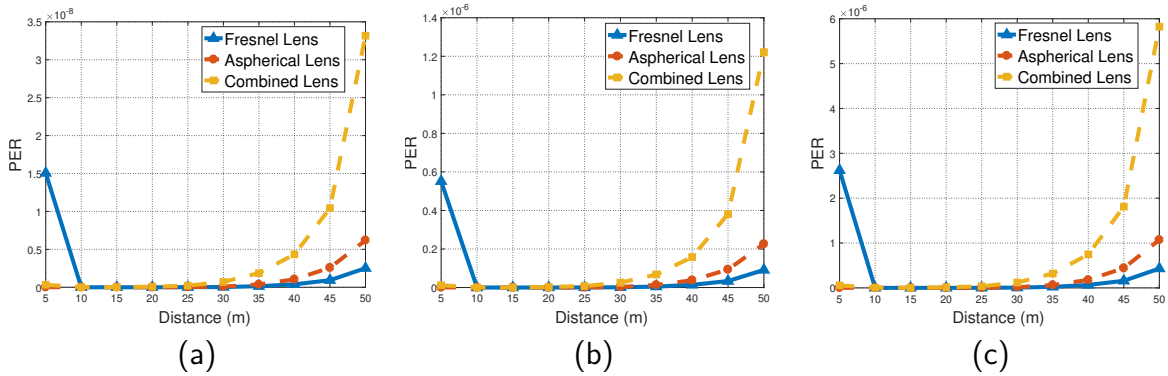

Figure 4.10: PER versus distance for (a) $B = 1$ MHz (b) $B = 5$ MHz (c) $B = 10$ MHz.

In Figure 4.9, we present the PER versus distance for different lens systems, considering different lateral offsets. We assume d_h= 0 m, 2 m, and 4 m. It is observed from Figure 4.9a (i.e., d_h= 0 m) that an error-free communication is remarkably achieved up to 30 m with all lenses. Beyond that, a degradation in performance is observed up to 50 m, where the L2 lens shows the best performance compared to other lens systems. For

example, consider d_x= 20 m, the PER refers to zero for all considered lens systems. Also, consider d_x= 40 m, the PER values are 0.2 × 10^{-7}, 0.4 × 10^{-7}, and 0.9 × 10^{-7} for L2, L1, and L3 lenses, respectively.

In the case of misalignment (i.e., d_h= 2 m) (Figure 4.9b), the three lenses still grant a nearly error-free link in the entire 10−29 m range. Beyond this range, the L2 lens suffers from worse performances at short distances ($d_x < 10$ m) due to it lower view angle. Also, at long distances $d_x \geq 30$ m, the performance servery degraded and the L2 lens is the best compared to other lenses. For example, consider d_x= 45 m, the obtained PER values are 0.4 ×10^{-7}, 0.9 × 10^{-7}, and 3.7 ×10^{-7} for L2, L1, and L3 lenses, respectively.

In Figure 4.9c, we present the PER versus distance, assuming d_h= 4 m. It is observed that an error-free communication is achieved in the distance range of 20−30 m. Outside this range, the performance deteriorates significantly, where the L1 lens gives the best results for short distances (15−20 m) and the L2 lens is the best for long distances (31−50 m).

In Figure 4.10, we present the PER versus distance for different bandwidth. We assume B= 1 MHz, 5 MHz, and 10 MHz. It is observed that the error rate increases with increasing values of the bandwidth. This is because the higher the bandwidth, the higher the noise variance. For example, consider the combined lens case and d_x= 45 m, the obtained values of PER are 10^{-8}, 0.4 × 10^{-6}, and 1.8 × 10^{-6} for $B = 1$ MHz, $B = 5$ MHz, and $B = 10$ MHz, respectively.

In the following, in order to generalize the lens selection during the car mobility, we analyze the choice of the suitable optical lens according to the angle of incidence of the incoming beam from the two headlamps (i.e. θ_1 and θ_2).

Table 4.2 and 4.3 show the best lens selection for a range of incident angles (i.e., θ_1 and θ_2). Table 4.2 shows the selection of the best lens selection to θ_1. It is observed that for a small angle of incidence, the Fresnel lens may be the better choice. While for medium and large angle of incidence, the aspherical lens and the combination lens are the best, respectively. For example, consider θ_1= 1.69°, the Fresnel lens is the best. Also, consider θ_1= 15.44°and θ_1= 44.42°, the aspherical lens and the combination lens are respectively the best choice.

In Table 4.3, we select the top lenses based on incident angle of the rays coming from TX2 (θ_2). It is observed that for small and medium angles of incidence, Fresnel and aspherical lenses may be the best choice. While for large angles of incidence, the combined lens may be the best. For example, consider θ_2= -1.69°, θ_2= 7.06°, and θ_2= 31.79°, the most appropriate lenses are respectively Fresnel, aspherical and combined lenses.

Table 4.2: Lens selection according to incident angle (θ_1)

Incident angle, θ_1	Fresnel Lens	Aspherical Lens	Combined Lens
1.03°-1.69°	✓		
1.70°-13.13°	✓	✓	✓
13.14°-15.43°		✓	✓
15.44°-20.65°		✓	
20.66°-30.11°		✓	✓
30.12°-44.42°			✓

Table 4.3: Lens selection according to incident angle (θ_2)

Incident angle, θ_2	Fresnel Lens	Aspherical Lens	Combined Lens
[-10.2°– -1.70°]	✓	✓	✓
[-1.69°– 0.18°]	✓		
[0.19°– 2.50°]	✓	✓	✓
[2.51°–3.54°]		✓	✓
[3.55°–5.71°]	✓	✓	✓
[5.72°–6.27°]	✓		
[6.28°–6.79°]	✓	✓	
[6.8°–7.06°]		✓	
[7.07°–8.39°]	✓	✓	
[8.40°–13.40°]		✓	
[13.41°–31.79°]			✓

4.5 Conclusion

In this chapter, we have investigated the performance of the V2V-VLC system using an imaging receiver with different kinds of lenses including Fresnel, Aspherical, and combined lenses. We have conduct a realistic channel modeling approach, based on a non-sequential ray-tracing approach, which takes into account the effect of headlight asymmetrical intensity profiles. The effect of the lens types, receiver types, receiver diameters, and bandwidth were further investigated. A comprehensive performance comparison is then conducted in terms of PER for different kinds of lenses. Our results reveal that with a carefully chosen system and lens parameters, an enhancement of 7 dB in total received power can be achieved. The results also reveal that the Fresnel lens is a good choice for improving performance, especially at long distances.

In the following chapter, we will present a optimization problem encountered in an indoor Visible Light Communication system and propose an efficient algorithm to solve it.

CHAPTER 5

RESOURCE ALLOCATION OF MASSIVE OPTICAL IOT SYSTEM BASED ON AN ENHANCED AQUILA OPTIMIZER ALGORITHM

5.1 Introduction

The Internet of Things (IoT) is an emerging and promising technology that tends to revolutionize the global world through connected physical objects and realizing smart manufacturing, smart grid, and smart cities [131, 132]. The concept of IoT has garnered a great deal of attention from the research community and industries with the goal of ensuring that tablets, sensors, smart transportation systems, smart phones, and other entities are connected to a common interface and can communicate with each other [133]. IoT is expected to create a conducive environment that will affect many aspects of daily life and business applications and contribute to the growth of the global economy, through the massive IoT. Massive IoT applications require connecting a huge number of smart devices, which can be deployed in shipping environments, smart homes (buildings) and cities, etc. to the cloud with low end-to-end cost [131].

Most IoT wireless access networks currently deployed use Radio Frequency (RF) communication technologies [134]. However, RF has extremely crowded spectrum and relatively limited bandwidth, so conventional RF femtocells will fail to support the massive connectivity in IoT networks and significantly increase the cost of IoT deployment. Therefore, Visible Light Communication (VLC) is one of the viable solutions. It is based on the use of Light-Emitting Diodes (LEDs) as wireless transmitters, in addition to their basic function as lighting devices. This dual functionality allows these components to be used as access points (APs) to provide internet and wireless access to multiple users. Despite the aforementioned benefits, IoT-VLC systems suffer from performance degrading factors such as limited LED coverage, as it requires a line of sight between the transmitter and receiver. This problem can be solved by using multi-user architectures (MU) in which multiple access points that handle users in their respective lighting zones can be used.

However, inter-symbol interference (ISI) resulting from multipath reflections can significantly degrade the performance of MU-IoT-VLC networks. Therefore, resource allocation schemes among different users are required to mitigate such interference.

The optimization of resources in a VLC system is a vital activity. Up to now, there have been some studies focusing on optimizing the resource in VLC system [135, 136, 137, 138, 139, 140]. In [135], a resource allocation problem for a VLC system is formulated based on convex optimization techniques to achieve proportional fairness under delay requirements. In [136], the authors investigated the problem of allocating subcarriers to maximize VLC channel capacity based on binary cuckoo search and genetic algorithms. The results showed that binary cuckoo search outperforms genetic algorithms in handling the proposed optimization problem. Also, Seguel et al. used a cuckoo search (CS) algorithm for a resource allocation problem for an indoor downlink VLC system. The optimization problem is formulated in the case where a centralized intelligent coordinator allocates each transmitter to a particular user at each time slot while maximizing the network throughput. In [137], a heuristic optimization algorithm is used for multi-user sum throughput maximization in indoor user-centric VLC (UC-VLC) systems. This problem is formulated through power allocation, user selection, and bit loading (i.e., modulation size selection). The authors in [138], applied the Particle Swarm Optimization (PSO) meta-heuristic algorithm for resource allocation in direct current-biased optical orthogonal frequency division multiple access (DCO-OFDM) systems to maximize the throughput and user satisfaction. Also, a resource allocation method for the uplink VLC system is proposed in [141], which is based on Genetic Algorithms (GA) to maximize the system data rate. The results proved the effectiveness of GA compared to the exhaustive optimization method. In [140], the authors applied simulated annealing (SA) algorithm for resource allocation problem in a multi-user DC-OFDM based VLC system to maximize the average user satisfaction index.

On the other hand, there are few attempts to address the optimization of the resource allocation problem in IoT-VLC systems. For example, a coordinated resource allocation problem is formulated in [142] for indoor IoT visible light communication and positioning multi-cell integrated (VLCP) systems. This proposal aims to maximize the sum rate while ensuring minimum data rates and device positioning accuracy requirements using the sequential quadratic programming (SQP) method. Similarly, the authors of [143], applied the Markov decision process (MDP) to solve a dynamic resource allocation problem for an indoor IoT-VLC scenario. The proposed approach aims to maximize the total user throughput and decreases the user packet loss rate. The simulation results show the performance gain compared to the conventional Round-robin method. The work in [144], proposed an optimization problem for an indoor IoT-VLC scenario that aims to minimize the total energy consumption of multiple LEDs while satisfying some quality of service (QoS) requirements. It should be further emphasized that the aforementioned works

[142, 143, 144] are limited to user numbers and do not consider the fairness between users which is vital in the real scenarios. For example, maintaining only the maximum sum rate might cause performance degradation or even dis-connectivity for the users located at the room corners.

In this chapter, we first present a resource allocation problem for an indoor IoT-VLC scenario. Then, this problem is solved based on an improved Aquila optimizer with the goal of maximizing capacity while considering fairness among users. The main contributions of this paper are listed below

- We consider an indoor IoT-VLC system with multiple LED transmit antennas and multiple users having multiple receive antennas. To reduce the inter-symbol and co-channel interferences while reducing the power consumption of the users' charging battery, we consider switching ON the most suitable PDs. The selection of such PDs is made to maximize both the capacity and the fairness for all users.

- To obtain the optimal PDs of each user, we propose an Enhanced Chaotic Quasi-Opposition-based Aquila Optimizer (ECQO-AO) scheme. The proposed ECQO-AO integrates four strategies including chaotic map mechanism, Quasi-Opposition-Based Learning (QOBL) concept, Fitness-distance balance (FDB) selection method, and cosine function to improve the optimization performance of AO algorithm.

- Different user distribution scenarios are considered and the effect of the number of users and the number of PDs on the performance is examined for all considered scenarios.

- The performance of the proposed algorithm is compared with other state-of-the-art algorithms such as GA, PSO, BBO, GWO, MFO, SCA, HHO, WOA, and AO in terms of capacity, fairness index, and fitness.

The remainder of this chapter is organized as follows. Section 5.2 presents the system model and the formulation of the resource allocation problem. Section 5.3 describes the concepts of AO, chaotic map, QOBL, FDB strategy and the cosine function techniques. Section 5.4 proposes the ECLO-MFO algorithm to solve the resource allocation problem. Section 5.5 gives the simulation results and analysis of the proposed ECQO-AO considering different scenarios in comparison with other works in the literature. Finally, we conclude the paper and suggest some future directions in Section 5.6.

5.2 Multi-User IoT-VLC System Model and Problem Formulation

5.2.1 IoT-VLC System Model

As illustrated in Figure 5.1, we consider an indoor multi-user IoT-VLC system in a room of dimension $R \times W \times H$ (see Figure 5.1a). This room is divided into 100 cells [145] as shown in Figure 5.1b and equipped with L light-emitting diodes (LEDs) placed on the ceiling to serve as optical IoT transmitters with an optical power of P_t. We assume that N receiving users are distributed in each cell inside this room. Each user is equipped with M photodetectors (PDs) that are evenly distributed on the user's cell phone as shown in Figure 5.1c. Each of them has an aperture diameter D_r and a responsivity R.

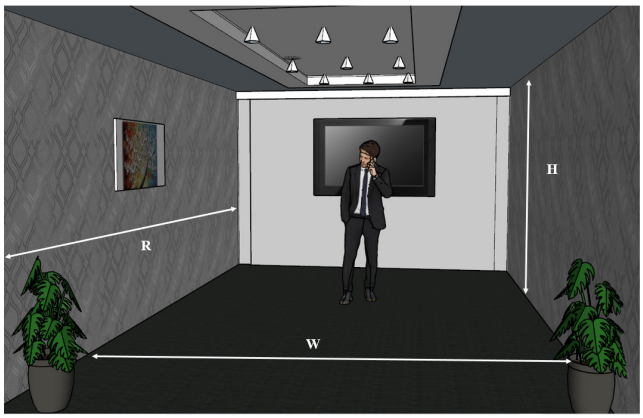

(a)

91	92	93	94	95	96	97	98	99	100
81	82	83	84	85	86	87	88	89	90
71	72	73	74	75	76	77	78	79	80
61	62	63	64	65	66	67	68	69	70
51	52	53	54	55	56	57	58	59	60
41	42	43	44	45	46	47	48	49	50
31	32	33	34	35	36	37	38	39	40
21	22	23	24	25	26	27	28	29	30
11	12	13	14	15	16	17	18	19	20
1	2	3	4	5	6	7	8	9	10

(b)

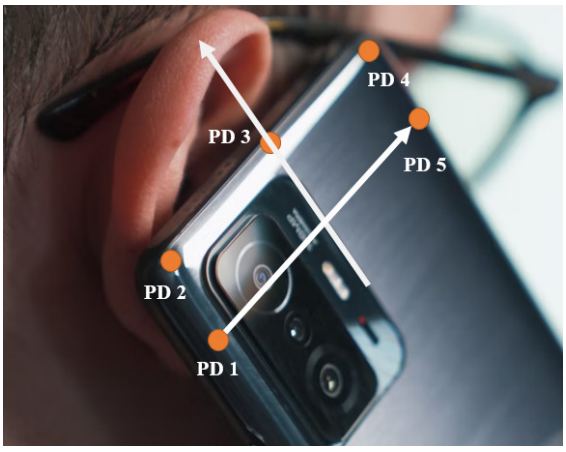

(c)

Figure 5.1: Location of PDs on the users cell phone.

For channel modeling, we follow the IEEE VLC channel modeling reference [145] by deploying the non-sequential ray-tracing modeling approach of OpticStudio software®,described in Chapter 2.

5.2.2 Problem Formulation

The considered indoor multi-users IoT-VLC system consists of multiple users where each has multiple PDs. In order to reduce the dimension of the optimization and decrease the energy consumption to conserve the battery charge of the users' device for a long time, we choose only the optimal PDs to be ON while the rest PDs are switched OFF. We further consider two cases as the following:

- **Case 1:** Only one of the PDs is assumed to be ON (active) at a time t and the remaining (M - 1) PDs are off. The allocation (assignment) of operating PDs for different users is done to reduce the battery consumption load and improve the overall network performance. In general, the activation and deactivation states of all PDs associated with different users are summarized in the following assignment matrix A ($N \times M$):

$$A = \begin{pmatrix} a_{11} & a_{12} & \cdots & a_{1M} \\ a_{21} & a_{22} & \cdots & a_{2M} \\ : & \ddots & : & : \\ a_{N1} & a_{N2} & \cdots & a_{NM} \end{pmatrix} \tag{5.1}$$

  where a_{lk} is a binary allocation variable associated with the k^{th} PD of the l^{th} user. The value of this variable is equal to 1 when the PD is activated and 0 otherwise. Since only one of the PDs is turned ON at a time t, the sum of the allocation variables associated with l^{th} user is equal to one. In other words, $\left(\sum_{k=1}^{M} a_{lk} = 1\right), \forall l \in \{1, 2, \cdots, N\}$. We further define $\bar{a}$ the vector that represents the active PD index for each user which is written as $\bar{a} = [\acute{a_1}, \acute{a_2}, ..., \acute{a_M}]$, where $\acute{a_l} \in \{1, 2, \ldots, M\}$ is the index of the activated PD for the l^{th} user at allocation vector $\bar{a}$. Thus, the binary variables a_{lk} values can be given as follows

$$a_{lk} = \begin{cases} 1, & k = \acute{a_l} \\ 0, & \text{otherwise} \end{cases} \tag{5.2}$$

  The Signal-to-Noise Ratio (SNR) of the l^{th} user can be expressed as follows:

$$\Gamma_l(\bar{a}) = \frac{R^2 \left(\sum_{k=1}^{M} P_t H_{k,l} a_{lk}\right)^2}{\sigma_t^2}, \tag{5.3}$$

  where R is the PD responsivity, $H_{k,l}$ is the channel gain at the k^{th} PD of the l^{th} user, and σ_t^2 denotes the total noise variance which can be given by $\sigma_t^2 = N_0 B$, where N_0 is the noise power spectral density and B is the bandwidth. It should be noted that to obtain reliable communication, the bit-error-rate (BER) obtained must be lower than a BER threshold, BER_{th}. In other words, $BER \leq BER_{th}$

Based on (5.3), the capacity can be estimated as [105]:

$$C_l(\bar{a}) \approx \frac{B}{2\ln(2)} \ln\left(1 + \frac{\exp(1)\Gamma_l(\bar{a})}{2\pi}\right). \tag{5.4}$$

In our study, two main objectives are needed to be optimized:

– The total capacity: for an allocation vector $\bar{a}$, the total achievable capacity is given by

$$C(\bar{a}) = \left(\sum_{l=1}^{N} C_l(\bar{a})\right). \tag{5.5}$$

– The Fairness: for an allocation vector $\bar{a}$, the maximum Jain fairness Index (JFI) is given as follows [146]

$$JFI(\bar{a}) = \frac{\left(\sum_{l-1}^{N} C_l(\bar{a})\right)^2}{N\sum_{l-1}^{N} C_l(\bar{a})^2} \tag{5.6}$$

Therefore, the problem under consideration can be stated as a maximization optimization problem which can be formulated as follows:

$$\begin{aligned} &\max_{\bar{a}} \left(C(\bar{a})\right) \\ &\max_{\bar{a}} \left(JFI(\bar{a})\right) \end{aligned} \tag{5.7}$$

s.t

$$\mathbf{C1:}\ \ a_{lk} = \begin{cases} 1, & k = \acute{a}_l \\ 0, & \text{otherwise} \end{cases} \quad \forall l, k \tag{5.8a}$$

$$\sum_{k-1}^{M} a_{lk} = 1, \forall l$$

$$\begin{aligned} &\mathbf{C2:}\ \ BER \leq BER_{th} \\ &l \in \{1, 2, \cdots, N\}, k \in \{1, 2, \cdots, M\}, \\ &\acute{a}_l \in \{1, 2, \ldots, M\} \end{aligned} \tag{5.8b}$$

- **Case 2:** Two PDs are assumed to be on (active) at a time t and the remaining (M - 2) PDs are off. Thus, the sum of the allocation variables associated with each user is equal to two. In other words, $\left(\sum_{k=1}^{M} a_{lk} = 2\right), \forall l \in \{1, 2, \cdots, N\}$. On the other hand, this assumption is applied while satisfying that the total energy consumption, P_c, of the activated PDs is below a power threshold (i.e. P_{th}). In other words, $\sum_{k=1}^{M} P_c \leq P_{th}$.

Therefore, the problem under consideration can be stat- ed as a maximization optimization problem which can be formulated as follows:

$$\begin{aligned} &\max_{\bar{a}} \left(C(\bar{a})\right) \\ &\max_{\bar{a}} \left(JFI(\bar{a})\right) \end{aligned} \tag{5.9}$$

s.t

$$\mathbf{C1:}\ \ a_{lk} = \begin{cases} 1, & k = \acute{a}_l \\ 0, & \text{otherwise} \end{cases} \quad \forall l, k \tag{5.10a}$$

$$\sum_{k-1}^{M} a_{lk} = 2, \forall l$$

$$\mathbf{C2:}\ \ \sum_{k-1}^{M} P_c \leq P_{th} \tag{5.10b}$$

$$\begin{aligned} &\mathbf{C3:}\ \ BER \leq BER_{th} \\ &l \in \{1, 2, \cdots, N\}, k \in \{1, 2, \cdots, M\}, \\ &\acute{a}_l \in \{1, 2, \ldots, M\} \end{aligned} \tag{5.10c}$$

5.3 Preliminaries

5.3.1 Aquila Optimizer Algorithm

Aquila Optimizer algorithm (AO), introduced by Abualigah et al. [147] in 2021, is a novel nature-inspired meta-heuristic algorithm that can be applied to solve different optimization problems. The main idea of AO is inspired by the behavior of Aquila in hunting and catching the prey based on four strategies expressed as follows [147]:

a . *High soar with a vertical stoop*: In this strategy, the Aquila flies at high altitude to explore the prey area. When it notices a prey, it increases its speed towards it, keeps its wings and tails closed and pushes its feet to catch it. This behavior is mathematically formulated as follows:

$$S_i{}^{(t+1)} = S_{best}^t \times \left(1 - \frac{t}{T}\right) + \left(S_m^t - S_{best}^t \times rand\right) \tag{5.11}$$

where $S_i{}^{(t+1)}$ denotes the position of the current individual i at iteration $t+1$. S_{best}^t is the current best solution obtained at the t^{th} iteration. $rand$ is a random number in the range of $[0, 1]$ generated using the Gaussian distribution and T represents the maximum number of iterations. S_m^t is the mean location value of the solution at

the current iteration t, which is calculated as follows:

$$S_m^t = \frac{1}{Ns} \sum_{i=1}^{Ns} S_i^t \tag{5.12}$$

where Ns is the number of population size.

b . *Contour flight with short glide attack*: In this strategy, the Aquila prepares for its instinctive predatory behavior by switching from high flight to hovering over its prey's head. This solution update can be expressed as follows:

$$S_i{}^{(t+1)} = S_{best}^t \times Levy(D) + S_R^t + (y - x) \times rand \tag{5.13}$$

where D is the dimension of the problem, S_R^t is the random position of Aquila, and $Levy$ expresses the $Levy$ flight distribution function which is formulated as follows:

$$Levy(D) = 0.01 \times \frac{U \times \gamma}{V^{\frac{1}{\beta}}} \tag{5.14}$$

where U and V are random vectors uniformly distributed in the range of $[0, 1]$, β is a constant of 1.5, and γ represents the mathematical gamma function calculated as follows:

$$\gamma = \frac{\Gamma(1 + \beta) \times \sin\left(\frac{\pi\beta}{2}\right)}{\Gamma\left(\frac{1+\beta}{2}\right) \times \beta \times 2^{\left(\frac{\beta-1}{2}\right)}} \tag{5.15}$$

where

$$\Gamma(x) = \int_0^\infty t^{x-1} e^{-x} dt \tag{5.16}$$

x and y denote the shape of the search, which can be given by:

$$\begin{cases} x = (r_1 + L \times D_1) \times \sin\left(-\omega \times D_1 + \frac{3\times\pi}{2}\right) \\ y = (r_1 + L \times D_1) \times \cos\left(-\omega \times D_1 + \frac{3\times\pi}{2}\right) \end{cases} \tag{5.17}$$

where r_1 is the number of search cycles which takes a value from 1 to 20, L is a small value set to 0.00565, D_1 is a random integer between 1 and the dimension D, and ω is a constant of 0.005.

c . *Low flight with slow descent attack*: In this strategy, the Aquila Initially discovers and identifies the approximate position of the prey, then it descends vertically on the prey and grabs it by the neck and back. The preliminary attack is formulated as follows:

$$\begin{aligned} S_i{}^{(t+1)} = \left(S_{best}^t - S_m^t\right) \times \alpha - rand \\ + ((UB - LB) \times rand + LB) \times \delta \end{aligned} \tag{5.18}$$

where δ and α are adjustment parameters during the development process set in

this paper to 0.1. Also, LB and UB are the lower and upper bounds of the given problem, respectively.

d . *Walking and grab prey*: Aquila goes on land to follow the escape path of its prey, and tries to pull its prey. Here, and finally, Aquila attacks the prey at the last position. This behavior is mathematically shown in the following equation:

$$\begin{aligned} S_i^{(t+1)} =& QF \times S_{best}^t - (G_1 \times S(t) \times rand) \\ & - G_2 \times Levy(D) + rand \times G_1 \end{aligned} \tag{5.19}$$

where QF denotes the quality function for balancing search's strategies, G_1 is the random motion parameter of the Aquila in the tracking process, and G_2 is the flight slope formed by the Aquila to follow the prey. They are given by the following equations:

$$QF = t^{\frac{2\times rand-1}{(1-T)^2}} \tag{5.20}$$

$$G_1 = 2 \times rand - 1 \tag{5.21}$$

$$G_2 = 2 \times (1 - \frac{t}{T}) \tag{5.22}$$

The pseudo-code of the AO Algorithm is illustrated in Algorithm 1 and the flowchart is presented in Figure 5.2.

It should be noted that the AO algorithm has high efficiency and strong global exploration capability, but its local exploitation capability is insufficient, so it is easy to fall into local optima. Thus, some improvements of the AO algorithm have been made in the literature [148, 149, 150]. For example, in [148], the authors proposed a hybridization of HHO and AO algorithms, namely IHAOHHO to improve the performance of AO algorithm. They integrate the exploitation strategy of HHO into AO algorithm to improve the exploitation phase of AO algorithm. The results show that IHAOHHO performs significantly better than other state-of-the-art algorithms. Also, a new improvement hybridizing Arithmetic Optimization Algorithm (AOA) and AO algorithm, called AOAAO has been proposed in [149]. Simulation results proved the efficiency of the new proposed algorithm compared to Salp Swarm Algorithm (SSA) and Whale Optimization Algorithm (WOA). A simplified Improved AO (IAO) algorithm is introduced in [150], where the equation controlling the exploitation procedure has been removed.

5.3.2 Chaotic Map

Chaos is a deterministic method used to analyze the behavior of nonlinear and dynamic systems. Naturally, chaos has the property of randomness, ergodicity, non-repetition, regularity, and stochastic. These characteristics have been transformed into various mathematical equations called chaotic maps. To date, many meta-heuristic algorithms contain

Algorithm 1 The pseudo-code of the Aquila Optimizer Algorithm

Initialize the population of Aquila individuals $S_i(i = 1, 2, ..., N)$
Initialize AO parameters
while $t \leq T$ **do**
    Calculate the fitness of each Aquila $f(S_i)$
    Determinate the best solution obtained S_{best}
    for $i = 1, 2, ..., N$ **do**
        Update the mean value of the current solution S_m using equation (5.12)
        Update $Levy(D), x, y, QF, G_1$, G_2, etc.
        if $t \leq \frac{2}{3} \times T$ **then**
            if $rand_1 \leq 0.5$ **then**
                Update the current solution S using equation (5.11)
            else
                Update the current solution S using equation (5.13)
            end if
        else
            if $rand_2 \leq 0.5$ **then**
                Update the current solution S using equation (5.18)
            else
                Update the current solution S using equation (5.19)
            end if
        end if
        if $f(S^{(t+1)}) < f(S^t)$ **then**
            $S^t = S^{(t+1)}$
        end if
    end for
    t=t+1
end while
Return The best solution S_{best}

random elements or specific parameters that need to be adjusted. However, parameter tuning is a difficult task because it can vary with different datasets. Chaos can therefore be an efficient way to solve this problem. The main idea is to replace random initialization variables with chaotic map variables. Therefore, this can improve the convergence rate and prevent the algorithm from being trapped into the local optimum. A variety of different chaotic maps are available in the optimization field. The ten well-known chaotic maps are Logistic map, Tent map, Sine map, Gauss map, Sinusoidal map, Chebyshev map, Piecewise map, Iterative map, Singer map, and Circle map. Tent map is one of the most representative chaotic maps generating a more uniform initial value between [0, 1] (see Figure 5.3), which improves the optimization speed of the algorithm. So, we adopted this chaotic map to replace the Aquila positions random variables. The formula of the

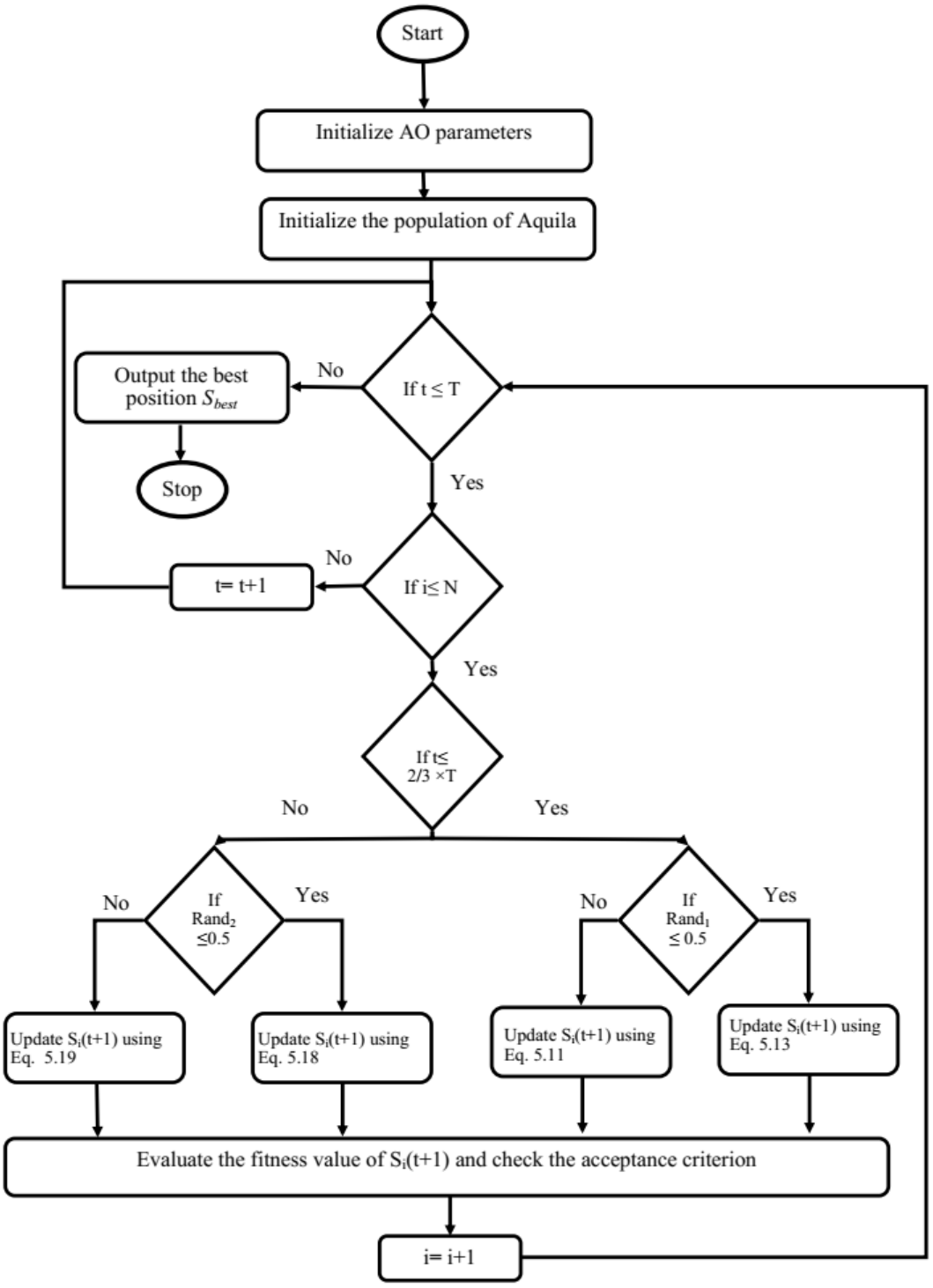

Figure 5.2: Flowchart of AO algorithm

Tent map can be given as follows:

$$Tm^{t+1} = \begin{cases} \frac{Tm^t}{u}, 0 \leq Tm^t < u \\ \frac{1-Tm^t}{1-u}, u \leq Tm^t \leq 1 \end{cases} \tag{5.23}$$

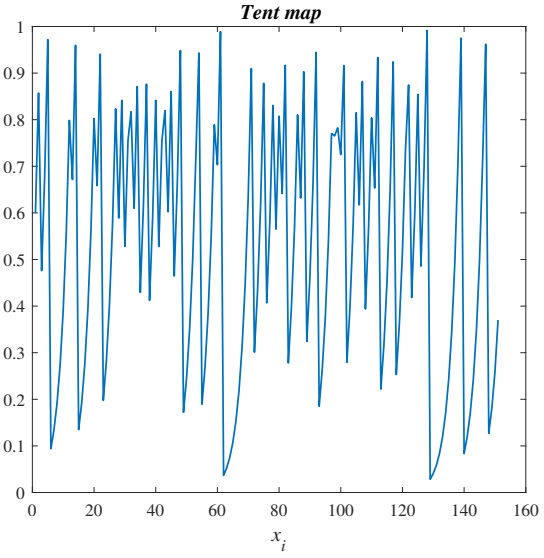

Figure 5.3: Chaotic value distributions during 160 iterations

where, Tm^t is the tent chaotic map value at the t^{th} iteration. In this study, we set u= 1/2 to ensure the best uniformity of the tent map and obtain a more evenly distributed sequence [151]. Thus, (5.23) can be re-written as follows

$$Tm^{t+1} = \begin{cases} 2Tm^t, & Tm^t < 0.5 \\ 2\left(1 - Tm^t\right), & Tm^t > 0.5 \end{cases} \tag{5.24}$$

5.3.3 Quasi Opposition-Based Learning

The Opposition-Based Learning (OBL) strategy proposed originally by Tizhoosh [152] is a well-regarded scheme in the field of machine learning and computational intelligence. It was first used to improve learning and back propagation in neural networks, and then combined successfully with meta-heuristic algorithms such as particle swarm optimization [153], genetic algorithm [154], grey wolf optimizer [155], and many others to enhance their convergence speed and explore the search space effectively. The main concept of OBL is the simultaneous evaluation of the current candidate solution and its corresponding opposite to choose the best one. OBL states that the opposite value of the current candidate is closer to the optimal solution than the random values. This allows the search process to become fast and accelerates the convergence speed. Consider S a real candidate solution in one dimension space, where $S \in [\mathrm{UB}, \mathrm{LB}]$. The opposite value S^o is defined as:

$$S^o = \mathrm{LB} + \mathrm{UB} - S \tag{5.25}$$

This definition can be generalized to d dimension using the following equation

$$S_i^o = \mathrm{LB}_i + \mathrm{UB}_i - S_i, \quad i \in 1, 2, \ldots, d. \tag{5.26}$$

where $S_i \in R$ and $S_i \in [\mathrm{LB}_i, \mathrm{UB}_i], \forall i \in 1, 2, \ldots, d$.

In the year of 2007, Rahnamayan et al. [156] introduced a new variant of OBL called Quasi-Opposition-Based Learning (QOBL). It is proven that the use of QOBL is more effective than OBL in finding the global optimal solution. The idea is to generate a random point between the center point C and the opposite point of S (i.e., S^o) as follows:

$$S^{qo} = \mathrm{rand}\,(C, S^o) \tag{5.27}$$

where C is the center of the interval $[\mathrm{LB}, \mathrm{UB}]$ which can be calculated as $C = \frac{LB+UB}{2}$. $\mathrm{rand}\,(C, S^o)$ is a random number uniformly distributed between C and S^o. Figure 5.4 illustrates a point S, its opposition S^o, and its quasi-opposition S^{qo} in one dimension space. Similarly, the quasi-opposite number can also be extended to d-dimensional space

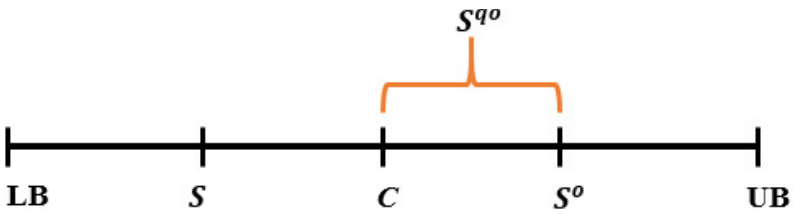

Figure 5.4: The point S, its opposition, S^o, and its quasi-opposition, S^{qo} in one dimension space.

using the following equation:

$$S_i^{qo} = \mathrm{rand}\left(\frac{\mathrm{LB}_i + \mathrm{UB}_i}{2}, S_i^o\right). \tag{5.28}$$

Generally, QOBL is applied in two aspects to improve the performance of meta-heuristic algorithms. The first one consists in applying it in the initialization of the population to obtain a more appropriate initial population value. The second one is to use it to make the algorithm generating dynamic leaps in the position update process, which enhance the exploration capability of the algorithm and prevent it from falling into the local optimum. In our study, we applied the second aspect to the ECQO-AO algorithm. We combined the quasi-opposition technique in the second part of its iterative process to guarantee the exploration capability of the algorithm and help it get out the local optimal solution.

5.3.4 Fitness Distance Balance (FDB)

The Fitness Distance Balance (FDB) selection method was recently proposed by Kahraman et al. in 2020 [157]. It is used to improve the search process performance of meta-heuristics such as Stochastic Fractal Search (SFS) [158], Symbiotic Organism Search (SOS) Algorithm [157], Coyote Optimization Algorithm (COA) [159], and Adaptive Guided Differential Evolution (AGDE) Algorithm [160]. The purpose of this method

is to identify the strongest individuals with characteristics that will be referred to in determining the future state of the population and that can effectively guide the search process. In this context, score values are calculated in the FDB selection method to indicate the contribution of solution candidates to the search process. The fitness values of the candidate solutions and the distance to the best candidate solution in the population are taken into account in the score calculation process. This ensures that the candidate solution with a high fitness value is chosen and prevents the selection of a candidate solution that is extremely close to the best solution. The steps of applying the FDB method are given as follows:

- For $P-$population composed of Ns design variables and m candidate solutions, the fitness values FV is calculated based on the objective function. Thus, the $P-$population vectors and the fitness values of the solution candidates are given by

$$P \equiv \begin{bmatrix} S_{11} & \cdots & S_{1N} \\ \vdots & \ddots & \vdots \\ S_{m1} & \cdots & S_{mN} \end{bmatrix}, FV \equiv \begin{bmatrix} f_1 \\ \vdots \\ f_m \end{bmatrix} \tag{5.29}$$

- Suppose that S_b is the best solution in the $P-$ population. The Euclidean distance between the i^{th} solution candidate S_i $(i \in 1, 2, ..., m)$ and the best solution S_b is calculated as follows:

$$D_{S_i} = \sqrt{\left(S_{1[i]} - S_{1[\mathrm{b}]}\right)^2 + \left(S_{2[i]} - S_{2[\mathrm{b}]}\right)^2 + \cdots + \left(S_{N[i]} - S_{N[\mathrm{b}]}\right)^2} \tag{5.30}$$

- The distance vector D_S for $P-$population can be given as follows:

$$D_S \equiv \begin{bmatrix} d_1 \\ . \\ . \\ d_m \end{bmatrix}_{m \times 1} \tag{5.31}$$

- Based on the fitness values given in (5.29) and the distance calculated in (5.30), the FDB score can be expressed as follows

$$\overset{m}{_{i=1}}\forall S_i, \quad C_{S_i} = w * \mathrm{norm}FV_i + (1 - w) * \mathrm{norm}D_{S_i} \tag{5.32}$$

where $\mathrm{norm}FV_i$ and $\mathrm{norm}D_{S_i}$ are the normalized fitness and distance values, respectively. They must be normalized so that they do not dominate each other in the score calculation. Also, w is the weighting coefficient.

- Finally, the m-dimensional C_S vector that represents the FDB scores of individuals in the P- population is given by

$$C_S \equiv \begin{bmatrix} c_1 \\ . \\ . \\ . \\ c_m \end{bmatrix}_{m \times 1} \tag{5.33}$$

The steps of the FDB selection method are given in Algorithm 2

Algorithm 2 The pseudo-code of the FDB method

```
begin
Select a distance metric
Generate a random number in the interval [0.4, 0.6] for the weighting coefficient w
for i = 1, 2, ..., m do
    Compute the distance between S_i and S_b using Eq.(5.30)
    Create or update the distance vector D_S as Eq.(5.31)
end for
for i = 1, 2, ..., m do
    Normalize the distance and fitness vectors in the interval [0, 1]
    Compute the score C_{S_i} for each candidate solution as Eq.(5.32)
    Create an FDB score vector using Eq.(5.33)
end for
Select solution candidates to include in the search process based on their scores (C_S)
end
```

5.3.5 Cosine Function

Previous works [161, 162, 163] have used trigonometric functions to bridge the gap between the exploration and the exploitation phases. In this study, we use the cosine function proposed in [164] to improve the performance of the Aquila algorithm in the exploration phase. The mathematical formulation of this function can be given as follows:

$$CF = \left(\cos^2\left(\frac{\alpha}{2}\right)\right)$$

where (5.34)

$$\alpha = \pi \times \frac{\text{Current Iteration}}{\text{Maximum Iteration}}$$

5.4 The proposed ECQO-AO algorithm for solving the problem

In this section, we describe the structure of our proposed ECQO-AO algorithm in detail. The core idea of ECQO-AO algorithm is the integration of four strategies including chaotic map, QOBL concept, FDB selection method, and cosine function into the original AO algorithm to improve its optimization performance.

Firstly, the chaotic sequence generated by Tent map according to (Eq.5.24) are used in three cases as described below:

- The first case entails replacing the random numbers in the range [0 1], involved in the definition of control parameters $G1$ and QF by the Tent chaotic map Tm_1, according to equations (5.35) and (5.36), respectively.

$$G_1 = 2 \times Tm_1 \tag{5.35}$$

$$QF = t^{\frac{2 \times Tm_1 - 1}{(1-T)^2}} \tag{5.36}$$

  These parameters are integrated in the calculation of the new position during the walking and grab prey strategy.

- In the second case, the random number in the range [0 1] used to determine the position updating strategy is replaced by Tent map Tm_2. Again, Tm_2 was integrated in the calculation of the opposite value of S based on the OBL technique, called S^o, as described below:

$$S^o = Tm_2 \times (\mathrm{LB} + \mathrm{UB}) - S \tag{5.37}$$

- In the last scenario, we also use Tent map Tm_3 to update the position instead of a random number for both high soars with a vertical stoop and low flight with slow descent attack phases.

Secondly, the FDB method is used for the efficient selection of reference positions that guide the AO search process. Therefore, the selection of candidate solutions by the FDB method can free the AO algorithm from the traps of local solutions. In our research, FDB is used to guide the search in both high soap with vertical stoop and low soap with slow descent attack strategies.

Third, the cosine function is used to fill the gap between the exploitation and exploration phases of the AO algorithm. Consequently, in our study, the cosine function is combined with FDB and Tent map to generate the new position in both high soap with vertical stoop and low flight with slow descend attack strategies. Specifically, if the Tent

sequence (Tm_3) is less than 0.25, the new position are updated according to Equations (5.38) and (5.39), respectively. In another case, if Tm_3 is either more or equal to 0.25 and less than 0.5, the new positions are updated according to equations (5.40) and (5.41) as shown below:

$$\begin{aligned} S_i^{(t+1)} = FDB^t \times \left(1 - \frac{t}{T}\right) \\ + \left(S_m^t - FDB^t \times Tm_3 + CF\right) \end{aligned} \tag{5.38}$$

$$\begin{aligned} S_i^{(t+1)} = (FDB^t - S_m^t) + CF \times \alpha - Tm_3 \\ + ((UB - LB) \times Tm_3 + LB) \times \delta \end{aligned} \tag{5.39}$$

$$S_i^{(t+1)} = FDB^t \times \left(1 - \frac{t}{T}\right) + \left(S_m^t - FDB^t \times rand\right) \tag{5.40}$$

$$\begin{aligned} S_i^{(t+1)} = \left(FDB^t - S_m^t\right) \times \alpha - rand \\ + ((UB - LB) \times rand + LB) \times \delta \end{aligned} \tag{5.41}$$

where CF is a real number in the range [0 1] generated using cosine function according to equation (5.34). FDB represents the leader of the population, generated based on the FDB selection method, following the steps illustrated in 2.

Fourth, quasi-oppositional based learning is used for better exploration of the search space. During the update phase, the positions are updated using the improved AO based on chaotic map, FDB, and cos functions strategies, and a new population is generated. Then, QOBL is applied to calculate the quasi-opposition of each solution ${S_i}^{qo}$ in the population using Eq.(5.27). The fitness values of the two populations are calculated and compared, and the best individuals from each are chosen as the next initial population. This mechanism is repeated until the maximum number of iterations is reached.

The pseudo-code of the Enhanced Aquila Optimizer Algorithm and the flowchart are shown in Algorithm 3 and Figure 5.5.

5.4.1 Objective function

Our proposed approach aims to maximize simultaneously the capacity and fairness metrics. These metrics are involved to define the fitness function f used to assess the quality of solutions. The objective function is given as follows:

$$f(S_i) = \lambda \times \frac{C(\bar{a})}{N \times C_{max}} + (1 - \lambda) \times JFI(\bar{a}) \tag{5.42}$$

where λ is a floating parameter in the range $[0, 1]$ which is used to control the importance of metrics. C_{max} is the maximum total capacity that can be achieved.

The original AO algorithm proposed by Abualigah et al. [147] was defined for mini-

Algorithm 3 The pseudo-code of the Enhanced Aquila Optimizer Algorithm

Input:
N: Number of users, M: Number of PDs
Ns: Population size, LB: Lower bound
UB: Upper bound, T: Maximum number of iterations
Output:
S_{best}: The best solution
$f(S_{best})$: The objective function of the best solution

begin
Initialize the population of the Aquila S_i
Initialize AO parameters
Initialize the value of the chaotic map
while $t \leq T$ **do**
    Calculate the fitness of each Aquila $f(S_i)$
    Determinate the best solution obtained S_b
    for i = 1 to Ns **do**
        Update the mean value of the current solution S_m using equation (5.12)
        Update $Levy(D)$, x, y, QF, G_1, G_2, etc.
        if $(t \leq \frac{2}{3} \times T)$ **then**
            Tm_3 generated in the range [0,1] by using Tent map
            if $(Tm_3 < 0.25)$ **then**
                Update the current solution (S) using equation (5.38)
            else if $0.25 \leq Tm_3 < 0.5$ **then**
                Update (S) using equation (5.40)
            else
                Update (S) using equation (5.13)
            end if
        else
            if $(Tm_3 < 0.25)$ **then**
                Update (S) using equation (5.39)
            else if $(0.25 \leq Tm_3 < 0.5)$ **then**
                Update (S) using equation (5.41)
            else
                Update (S) using equation (5.19)
            end if
        end if
        Applying QOBL using Eq.(5.27)
        if $(f(S(t+1)) < f(S(t)))$ **then**
            $(S(t) = S(t+1))$
        end if
    end for
    t=t+1
end while
return The best solution (S_{best})

mization problem. Thus, we need to transform our objective function into a minimization

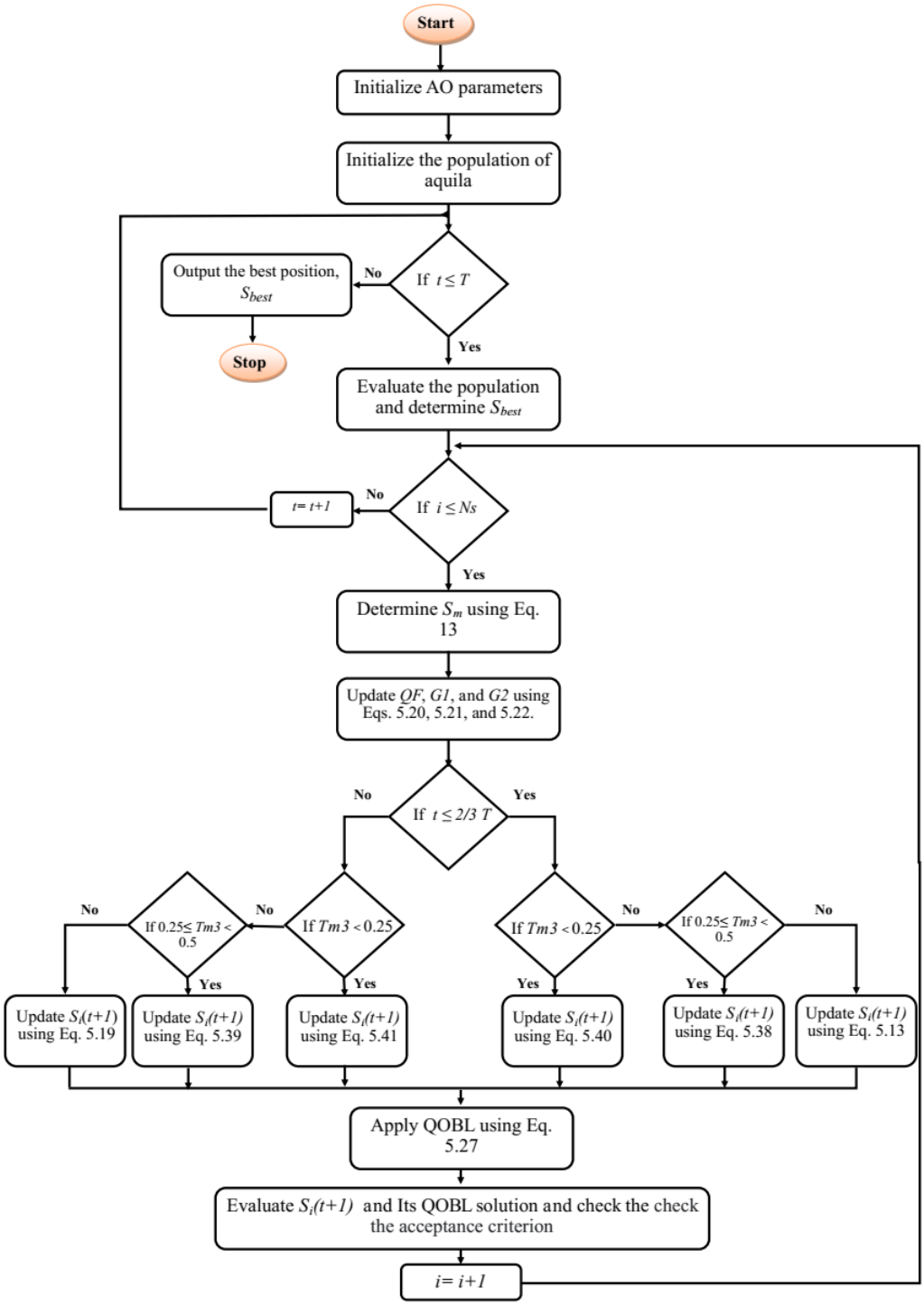

Figure 5.5: Flowchart of ECQO-AO algorithm

function. Consequently, we have defined a new function g as follows:

$$g = 1 - f(S_i) \tag{5.43}$$

Table 5.1: Main Simulation Parameters

	System Parameters	**Values**
Room	Dimension	10×10×3
Transmitter	Optical power, P_t	11 W
Receiver	Aperture diameter, D_r	1 cm
	Responsivity, R	0.54 A/W

5.5 Simulation Results

In this section, we present the numerical results of our proposed model. We first obtain the channel gain values at all users utilizing the reference IEEE channel model in [145]. The performance analysis is then made based on this and the effect of different system parameters are investigated. First, we investigate the impact of varying the number of users for the two scenarios under consideration. Then, we perform a comparative study with eight well-known algorithms in terms of capacity, fairness, and fitness.

5.5.1 Numerical Parameters

In our simulation, we consider a room of dimension 10×10×3, $L = 9$, $M = 5$, $R = 0.54$ A/W, and $D_r = 1$ cm. We further assume N_0= 10^{-21} A^2/Hz, $B = 1$ MHz, and BER_{th} = 10^{-6}. Different users number, i.e., $N = 20$, 30, 40, 50, 60, 70, 80, 90, and 100 are considered. All simulations are performed in Matlab software with a total number of iterations of 1000 and an average of 30 executions to relieve the effects of randomness by obtaining average result values. The simulation parameters are listed in Table 5.1 and the algorithm parameters are described in Table 5.2.

5.5.2 Effect of varying the number of users

In this section, we investigate the effect of varying the number of users on the performance of our proposed approach in terms of capacity, fairness, and fitness. Toward that, we perform a comparison study with AO, GA, PSO, BBO, GWO, MFO, SCA, HHO, and WOA algorithms to show the effectiveness of our proposed approach. We consider the case of only one PD on and N varies from 20 to 100 users. The Complete results of our simulations can be found in the Appendix. Figure 5.6 and Table 5.3 show the effect of varying the number of users on the total capacity. It is observed that the proposed ECQO-AO algorithm achieves a higher capacity compared to other algorithms (see Figure 5.6a). For example, consider $N = 90$ users and ECQO-AO algorithm. The achieved capacity is 1322 Mbit/s with an improvement of 12 Mbit/s, 18 Mbit/s, 80 Mbit/s, 20 Mbit/s,

Table 5.2: Algorithms parameters

Parameter	**Value**
ECQO-AO	
Exploitation adjustment parameter α	0.1
Exploitation adjustment parameter β	0.1
Weighting coefficient w	0.75
Control parameter Tm^0	0.8
AO	
Exploitation adjustment parameter α	0.1
Exploitation adjustment parameter β	0.1
GA	
Crossover probability p_c	0.8
Mutation probability p_m	0.2
Elitism probability	0.2
WOA	
Control parameter a_{min}	0
Control parameter a_{max}	2
PSO	
Inertia maximum weight ω_{Max}	0.9
Inertia minimum weight ω_{Min}	0.4
Parameter $c1$ in updating velocity	2
Parameter $c2$ in updating velocity	2
BBO	
Keep Rate	0.2
Mutation probability Pm	0.1
GWO	
Control parameter a_{min}	0
Control parameter a_{max}	2
MFO	
Control parameter b	1
Control parameter a_{min}	-2
Control parameter a_{max}	-1
HHO	
Control parameter a_{min}	0
Control parameter a_{max}	2
SCA	
Control parameter a_{min}	0
Control parameter a_{max}	2

14 Mbit/s, 37 Mbit/s, 37 Mbit/s, 5 Mbit/s, and 15 Mbit/s compared to AO, GA, PSO, BBO, GWO, MFO, SCA, HHO, WOA, respectively (see Table 5.3). It is also observed that the total capacity increases as the number of users increases (see Figure 5.6b). For

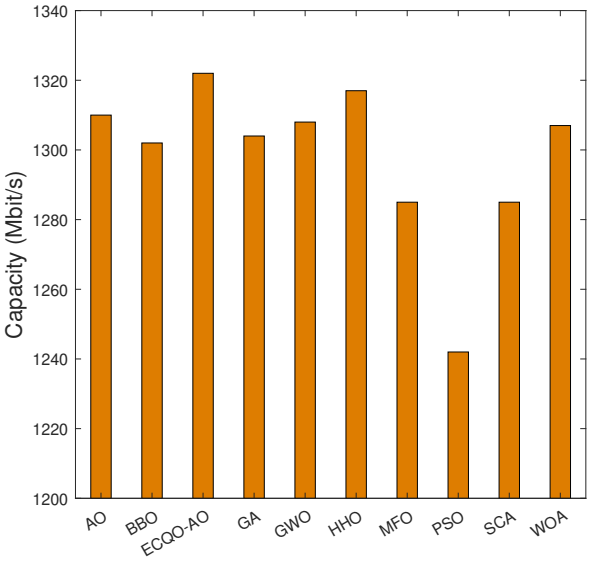

(a)

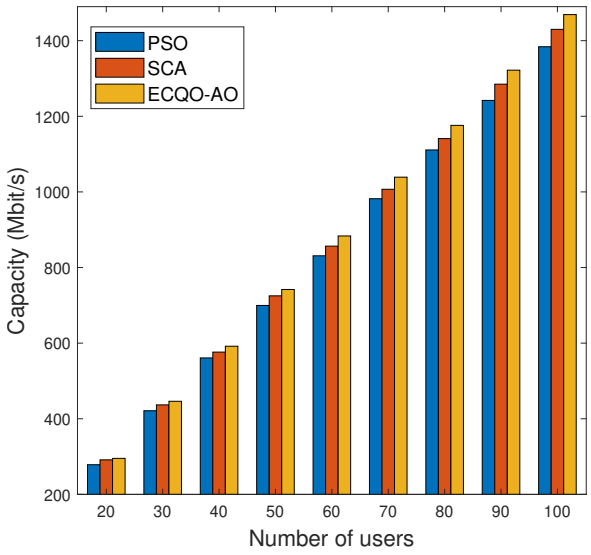

(b)

Figure 5.6: Capacity under various numbers of users considering case 1.

example, consider $N = 20$ users and the PSO algorithm. The total capacity reached is set to 278.4 Mbit/s. This increases to 421.2 Mbit/s, 560.9 Mbit/s, 699.7 Mbit/s, 831 Mbit/s, 982 Mbit/s, 1111 Mbit/s, 1242 Mbit/s, 1384 Mbit/s for $N = 30$, $N = 40$, $N = 50$, $N = 60$, $N = 70$, $N = 80$ $N = 90$ and $N = 100$ users, respectively.

In Figure 5.7, we present the Jains fairness achieved versus number of users for all considered algorithms. It is observed that the ECQO-AO scheme has noticeable higher bit-rate fairness than other algorithms for any number of users. Numerically, consider $N = 70$ users. ECQO-AO algorithm achieves a fairness index of 0.9979. This reduces to 0.9974, 0.9977, 0.9944, 0.9973, 0.9975, 0.9957, 0.9965, 0.9973, 0.9972 for AO, GA, PSO,

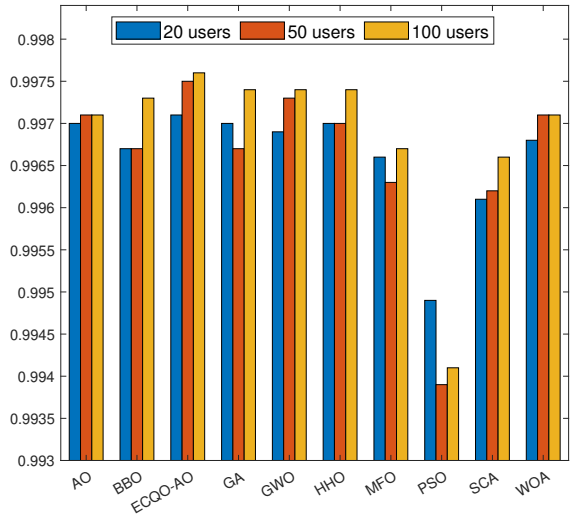

Figure 5.7: Fairness under various numbers of users considering case 1.

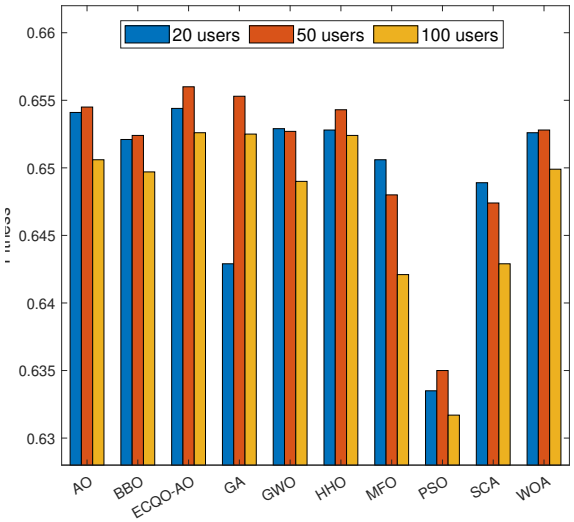

Figure 5.8: Fitness under various numbers of users considering case 1.

BBO, GWO, MFO, SCA, HHO, and WOA, respectively.

In Figure 5.8, we present the fitness as function of number of users for the different algorithms. Figure 5.8 shows the effectiveness of the proposed algorithm in achieving a better fitness for all considered scenarios. For example, consider $N = 30$ users. The values of obtained fitness are given as 0.6572, 0.6565, 0.6568, 0.6357, 0.6534, 0.6554, 0.6517, 0.6509, 0.6558, 0.6549 for ECQO-AO, AO, GA, PSO, BBO, GWO, MFO, SCA, HHO, and WOA, respectively. In the following, we demonstrate the effectiveness of our proposed approach in terms of the number of outage users that do not satisfy the performance requirements of our network. Thus, in Figure 5.9 we present the number of blocked users for different algorithms considering different scenarios (i.e., different numbers of users). We assume a threshold BER, $BER_{th} = 10^{-6}$. It is observed that our proposed algorithm

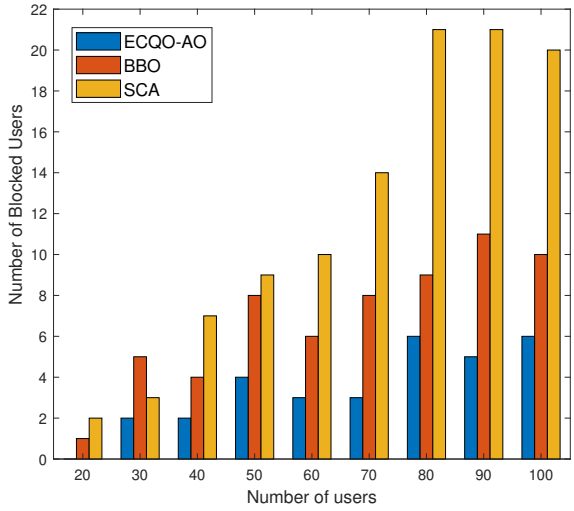

Figure 5.9: Number of blocked users for different algorithms considering $BER_{th} \leq 10^{-6}$.

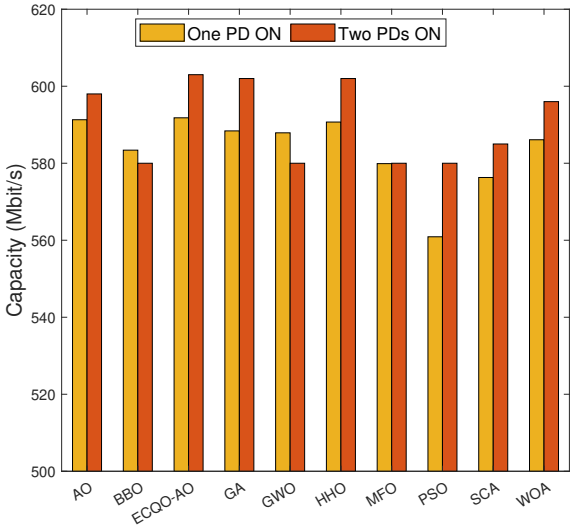

Figure 5.10: Capacity under various numbers of PDs.

has the minimum number of blocked users for all considered scenarios compared to the BBO and SCA algorithms. For example, consider $N = 70$. The number of blocked users is set to 3 for the case of the proposed ECQO-AO. This increases to 8 and 14 for the case of BBO and SCA algorithms, respectively. Also, consider $N = 40$. The numbers of blocked users are 2, 4 , and 7 for the cases of ECQO-AO, BBO and SCA algorithms, respectively.

5.5.3 Effect of varying the number of PDs

In this section, we evaluate the impact of increasing the number of adopted PDs (i.e., PD on) on the performance of the proposed approach. We conduct a performance comparison with other algorithms existing in the literature

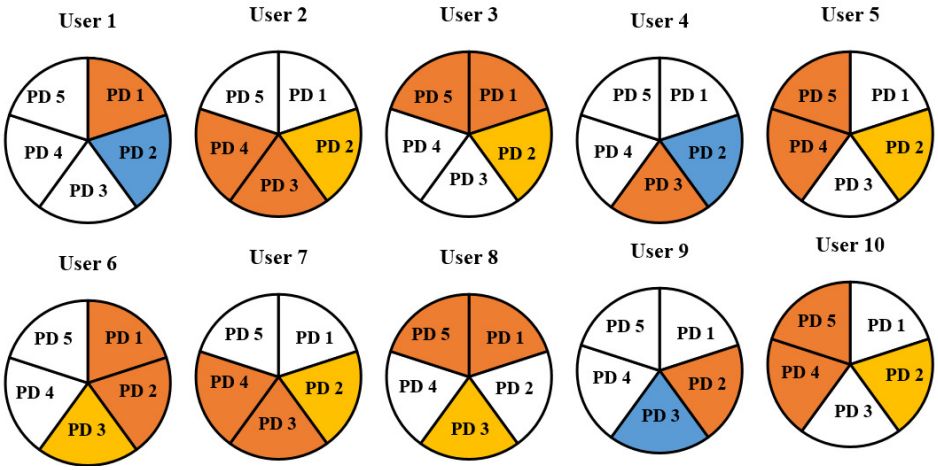

Figure 5.11: The selection of PDs activated of the first ten users by the BBO algorithm. The yellow color corresponds to the case where only one PD is activated. The orange color corresponds to the case where two PDs are activated. The blue color corresponds to the case where the same PD is activated in both cases.

In Figure 5.10, we present the capacity for the two cases under consideration (i.e., one PD on and two PDs on), considering all algorithms. It is observed that the capacity increases with the increase of the number of PDs activated for most of the considered algorithms. This is due to the fact that as the number of receivers increases, the amount of captured light emitted by the transmitters increases. For example, consider $N = 40$, GA algorithm, and the case of only one activated PD. The capacity reached is fixed at 588.4 Mbit/s. This claims to 602 Mbit/s for the case of two switched-on PDs. Also, consider $N = 40$ and AO algorithm. The obtained capacities are 591.3 Mbit/s and 598 Mbit/s for the cases of a single activated PD and two activated PDs, respectively. On the other hand, in order to understand why in some cases one PD performs better while in other cases two PDs perform better, we will present additional results. In Figure 5.11, we present a pie chart of the PDs selected for the first 10 users by the BBO algorithm considering both cases (one PD enabled and two PDs enabled). It is observed that there is a difference in the selected PDs between the users in both cases (only 3 users can activate the same PD in both cases). In addition, due to the difference in channel gain values between the PDs, the algorithm can select the two PDs with the lower channel gain values. This explains why the one PD case may perform better than the two PDs case. For example, consider user 2 and the BBO algorithm. The selected PD is PD2 for case 1. While in case 2, the selected PDs are PD3 and PD4. The table in the appendix also contains the activated PDs of each user for the proposed algorithm considering the two cases under consideration.

Figure 5.12 indicates the obtained fairness for the two cases under consideration. It is observed that in most of the cases it is better to use one PD rather than two. This is due to the difference between the PDs selected by the algorithms for the two cases.

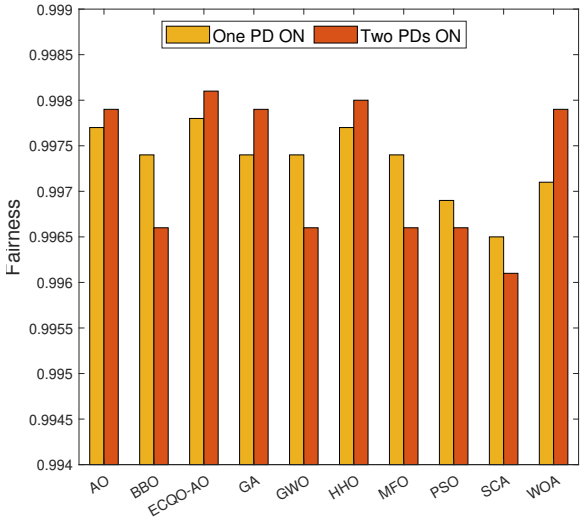

Figure 5.12: Fairness under various numbers of PDs.

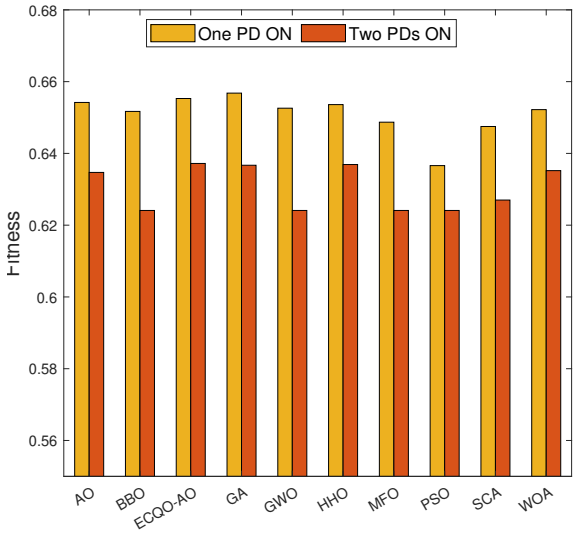

Figure 5.13: Fitness under various numbers of PDs.

For example, consider $N = 40$, BBO algorithm, and the case of only one PD activated. The achieved fairness level is about 0.9974. This decreases to 0.9966 when two PDs are activated. Likewise, consider the GWO algorithm. The achieved fairness index is 0.9974 and 0.9966 for the cases of one and two activated PDs, respectively.

Figure 5.13 shows the achieved fitness for the two considered cases (i.e., only one activated PD and two activated PD). It is observed that the case when one PD is activated is much better than the case of two activated PD. This is due to the ability of the algorithms to find the best solution for case 1 better and faster than for case 2. For example, consider $N = 40$ and ECQO-AO algorithm. The obtained fitness level is given as 0.6553 for the case of only one activated PD. This reduces to 0.6372 for two activated PDs cases. Also, consider the HHO algorithm. The achieved fitness levels are 0.6536 and

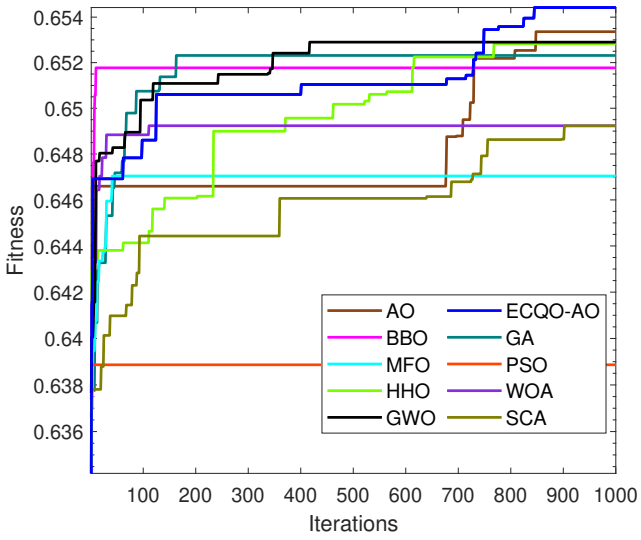

Figure 5.14: Convergence analysis considering 20 users.

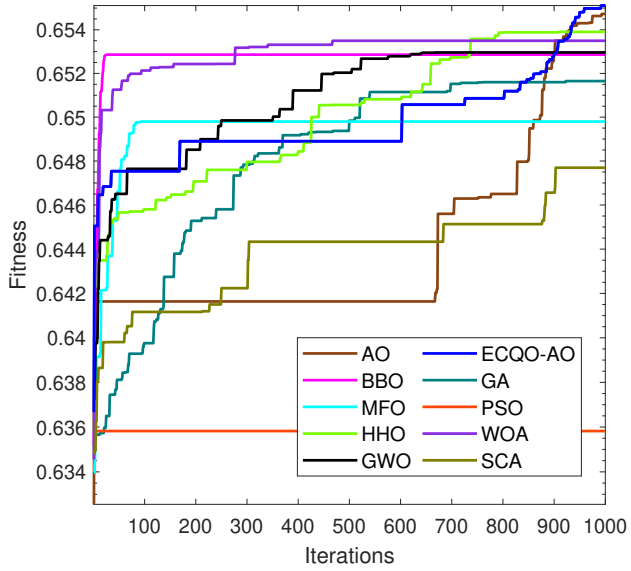

Figure 5.15: Convergence analysis considering 50 users.

0.6369 for one and two activated PDs cases, respectively.

5.5.4 Convergence Analysis

In this section, we analyze the convergence of the different considered algorithms. The convergence process is based on two parameters: the convergence speed and the convergence efficiency (fitness value). Each result obtained is an average of 30 executions.

Figures 5.14, 5.15, and 5.16 illustrate the best solutions obtained as a function of the number of iterations for all the considered algorithms. In terms of convergence efficiency, we observe the superiority of the proposed ECQO-AO compared to other state-of-the-art

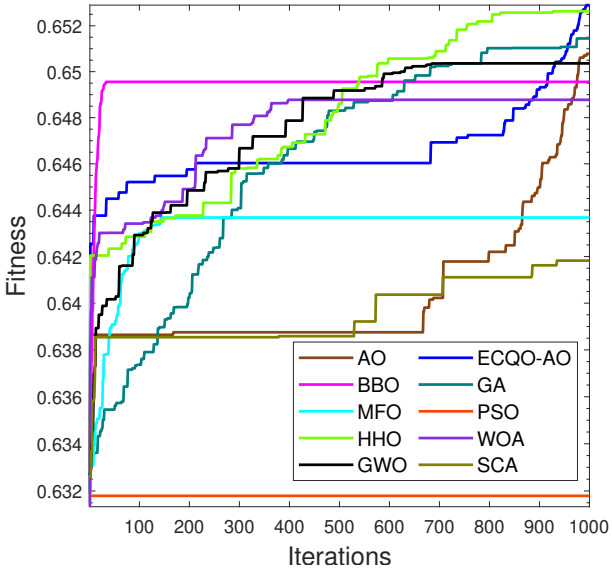

Figure 5.16: Convergence analysis considering 100 users.

algorithms. In terms of convergence speed, It is observed that ECQO-AO presents three different convergence behaviors during optimization processes. The first behavior is the extremely fast convergence speed, where the proposed ECQO-AO algorithm can find the optimum at an extremely fast speed in 20 iterations. Secondly, ECQO-AO algorithm gradually converges to the optimal values. The last behavior shows the ability to avoid the local optimum, where the ECQO-AO algorithm jumps out of the local optimum after several stagnation times. It is also observed that the number of iterations that the ECQO-AO algorithm requires for convergence does not increase with the number of users. This means that the ECQO-AO method is able to converge regardless of the number of users. It should be noted that the results show that the proposed ECQO-AO algorithm needs more iterations to achieve the global optimum. However, the fitness achieved by ECQO-AO is the best in most cases.

5.6 Conclusion

In this chapter, we have proposed an efficient optimization scheme named Enhanced Chaotic Quasi-Opposition-based AO (ECQO-AO) to solve the resource allocation problem in the indoor Multi-user IoT-VLC system. The proposed ECQO-AO is based on the integration of four concepts (i.e., chaotic map, QOBL mechanism, FDB selection method, and cosine function) into the original AO. The performance of ECQO-AO has been assessed considering different numbers of users and PDs. The obtained results demonstrated the superiority and the effectiveness of proposed ECQO-AO scheme over other optimization algorithms such as GA, PSO, BBO, GWO, MFO, SCA, HHO, and AO in terms of capacity, fairness, and fitness. While we tested the proposed ECQO-AO scheme in indoor

Table 5.3: Capacity, fairness, and fitness under various user numbers for case 1

	N	**20**	**30**	**40**	**50**	**60**	**70**	**80**	**90**	**100**
Capacity (Mbit/s)	ECQO-AO	**295.2**	**446.2**	**591.8**	**741.9**	**883.5**	**1039**	**1176**	**1322**	**1469**
	AO	295.1	444.2	591.3	737.5	877.4	1033	1163	1310	1463
	GA	294.4	438.9	588.4	735.2	877.7	1029	1164	1304	1462
	PSO	278.4	421.2	560.9	699.7	831	982	1111	1242	1384
	BBO	294	439.4	583.4	731.3	873.6	1021	1162	1302	1454
	GWO	294.1	443.5	587.9	735.3	871.7	1026	1157	1308	1454
	MFO	291.6	438.4	579.9	729.7	857.4	1009	1141	1285	1435
	SCA	291.3	436.7	576.3	725.1	856.6	1007	1141	1285	1430
	HHO	294.6	442.9	590.7	737.5	879.7	1032	1172	1317	1465
	WOA	294.6	443.7	586.1	733.5	876.6	1026	1161	1307	1460
Fairness	ECQO-AO	**0.9971**	**0.9982**	**0.9978**	**0.9975**	**0.9979**	**0.9979**	**0.9976**	**0.9978**	**0.9976**
	AO	0.9970	0.9980	0.9977	0.9971	0.9976	0.9974	0.9972	0.9973	0.9971
	GA	0.9970	0.9975	0.9974	0.9967	0.9975	0.9977	0.9967	0.9969	0.9974
	PSO	0.9949	0.9928	0.9969	0.9939	0.9957	0.9944	0.9950	0.9940	0.9948
	BBO	0.9967	0.9974	0.9974	0.9967	0.9975	0.9973	0.9972	0.9975	0.9973
	GWO	0.9969	0.9981	0.9974	0.9973	0.9973	0.9975	0.9971	0.9975	0.9974
	MFO	0.9966	0.9980	0.9974	0.9963	0.9967	0.9957	0.9958	0.9967	0.9967
	SCA	0.9961	0.9980	0.9965	0.9962	0.9973	0.9965	0.9968	0.9965	0.9966
	HHO	0.9970	0.9978	0.9977	0.9970	0.9978	0.9973	0.9973	0.9978	0.9974
	WOA	0.9968	0.9977	0.9971	0.9971	0.9975	0.9972	0.9964	0.9975	0.9971
Fitness	ECQO-AO	**0.6544**	**0.6572**	**0.6553**	**0.6560**	**0.6536**	**0.6560**	**0.6533**	**0.6526**	**0.6526**
	AO	0.6541	0.6565	0.6542	0.6545	0.6516	0.6541	0.6502	0.6497	0.6506
	GA	0.6429	0.6568	0.6546	0.6553	0.6535	0.6457	0.6513	0.6484	0.6525
	PSO	0.6335	0.6357	0.6366	0.6350	0.6320	0.6361	0.6327	0.6304	0.6317
	BBO	0.6521	0.6534	0.6517	0.6524	0.6493	0.6519	0.6489	0.6481	0.6497
	GWO	0.6529	0.6554	0.6526	0.6527	0.6494	0.6522	0.6484	0.6484	0.6490
	MFO	0.6506	0.6517	0.6487	0.6480	0.6437	0.6457	0.6422	0.6416	0.6421
	SCA	0.6489	0.6509	0.6475	0.6474	0.6436	0.6464	0.6422	0.6422	0.6429
	HHO	0.6528	0.6558	0.6536	0.6543	0.6521	0.6548	0.6509	0.6514	0.6524
	WOA	0.6526	0.6549	0.6522	0.6528	0.6513	0.6528	0.6489	0.6484	0.6499

IoT VLC system, while we believe that its applications can be extended for outdoor IoT VLC systems which would be considered as a future work.

.1 Appendix

In this appendix, we present the detailed results of the simulation. Table 5.3 and 5.4 show the results of capacity, fairness, and fitness for different considered algorithms considering case 1 and 2, respectively. Table 5.5 and 5.6 shows the index of the different activated PDs of each user for the proposed algorithm considering the two cases under consideration.

Table 5.4: Capacity, fairness, and fitness under various user numbers for case 2

	N	**20**	**30**	**40**	**50**	**60**	**70**	**80**	**90**	**100**
Capacity (Mbit/s)	ECQO-AO	**302**	**454**	**603**	**753**	894	1051	**1191**	1338	**1493**
	AO	300	452	598	742	883	1034	1165	1304	1457
	GA	300	453	602	750	892	1050	1186	1331	1483
	PSO	283	432	580	722	863	1019	1152	1294	1441
	BBO	283	432	580	722	863	1019	1152	1294	1441
	GWO	283	432	580	722	863	1019	1152	1294	1441
	MFO	283	432	580	722	863	1019	1152	1294	1441
	SCA	298	447	585	722	863	1019	1152	1294	1441
	HHO	301	453	602	752	**896**	**1053**	1191	**1339**	1492
	WOA	300	452	596	747	890	1049	1186	1332	1484
Fairness	ECQO-AO	**0.9985**	**0.9986**	**0.9981**	**0.9977**	**0.9983**	**0.9982**	**0.9981**	**0.9982**	**0.9982**
	AO	0.9983	0.9985	0.9979	0.9976	0.9981	0.9977	0.9978	0.9976	0.9975
	GA	0.9983	**0.9986**	0.9979	0.9975	0.9981	0.9980	0.9977	0.9978	0.9978
	PSO	0.9974	0.9969	0.9966	0.9969	0.9977	0.9974	0.9976	0.9974	0.9973
	BBO	0.9974	0.9969	0.9966	0.9969	0.9977	0.9974	0.9976	0.9974	0.9973
	GWO	0.9974	0.9969	0.9966	0.9969	0.9977	0.9974	0.9976	0.9974	0.9973
	MFO	0.9974	0.9969	0.9966	0.9969	0.9977	0.9974	0.9976	0.9974	0.9973
	SCA	0.9984	0.9980	0.9961	0.9969	0.9977	0.9974	0.9976	0.9974	0.9973
	HHO	0.9984	0.9985	0.9980	**0.9977**	0.9979	0.9979	0.9977	0.9980	0.9979
	WOA	0.9983	0.9985	0.9979	0.9974	0.9980	0.9977	0.9979	0.9976	0.9980
Fitness	ECQO-AO	**0.6376**	**0.6388**	**0.6372**	**0.6369**	0.6340	0.6362	**0.6332**	0.6327	**0.6341**
	AO	0.6372	0.6375	0.6347	0.6332	0.6298	0.6306	0.6273	0.6262	0.6267
	GA	0.6367	0.6384	0.6367	0.6358	0.6328	0.6361	0.6321	0.6316	0.6321
	PSO	0.6169	0.6220	0.6241	0.6229	0.6219	0.6258	0.6220	0.6217	0.6222
	BBO	0.6169	0.6220	0.6241	0.6229	0.6219	0.6258	0.6220	0.6217	0.6222
	GWO	0.6169	0.6220	0.6241	0.6229	0.6219	0.6258	0.6220	0.6217	0.6222
	MFO	0.6169	0.6220	0.6241	0.6229	0.6219	0.6258	0.6220	0.6217	0.6222
	SCA	0.6338	0.6339	0.6270	0.6229	0.6219	0.6258	0.6220	0.6217	0.6222
	HHO	0.6373	0.6386	0.6369	0.6365	**0.6347**	**0.6365**	0.6330	**0.6329**	0.6338
	WOA	0.6368	0.6372	0.6352	0.6348	0.6326	0.6355	0.6318	0.6316	0.6326

Table 5.5: PDs ON for the case 1 under consideration

Algorithm	**One PD ON**	
ECQO-AO	20 users	1, 2, 2, 2, 2, 2, 2, 3, 3, 2, 2, 3, 2, 3, 3, 2, 2, 2, 3, 4.
	30 users	1, 2, 2, 1, 2, 2, 3, 2, 2, 3, 3, 2, 1, 2, 2, 3, 2, 2, 3, 3, 1, 1, 2, 2, 1, 2, 2, 3, 3, 4.
	40 users	2, 1, 2, 1, 2, 2, 2, 2, 2, 3, 2, 2, 2, 3, 3, 2, 2, 3, 2, 2, 3, 2, 3, 3, 2, 2, 1, 3, 3, 1, 2, 2, 2, 2, 1, 2, 3, 3, 3, 4.
	50 users	1, 2, 2, 2, 1, 2, 2, 2, 2, 2, 2, 1, 3, 3, 2, 2, 2, 2, 2, 2, 2, 2, 2, 3, 1, 3, 2, 2, 2, 3, 3, 3, 3, 3, 3, 3, 2, 2, 1, 2, 2, 1, 2, 2, 2, 3, 3, 4, 3, 3.
	60 users	3, 2, 2, 2, 3, 2, 2, 2, 3, 2, 3, 3, 2, 3, 3, 3, 2, 3, 1, 3, 1, 2, 2, 2, 2, 2, 2, 2, 2, 2, 3, 2, 2, 3, 1, 3, 2, 2, 2, 2, 3, 3, 3, 3, 3, 3, 3, 3, 3, 3, 1, 2, 2, 2, 2, 2, 2, 2, 2, 2.
	70 users	2, 2, 1, 1, 2, 2, 1, 2, 2, 2, 2, 2, 2, 2, 2, 2, 2, 3, 2, 2, 3, 1, 3, 2, 3, 1, 3, 1, 2, 2, 2, 2, 2, 2, 2, 2, 1, 2, 2, 3, 1, 3, 2, 2, 2, 2, 3, 3, 1, 3, 3, 3, 3, 3, 3, 3, 3, 1, 2, 2, 2, 2, 1, 2, 2, 2, 2, 1, 3, 4.
	80 users	3, 2, 2, 2, 3, 2, 2, 2, 3, 2, 3, 3, 2, 3, 3, 3, 4, 3, 3, 3, 1, 2, 2, 2, 2, 2, 2, 2, 2, 2, 3, 2, 2, 3, 2, 3, 2, 2, 2, 2, 3, 3, 3, 3, 3, 3, 5, 3, 3, 3, 1, 2, 2, 2, 2, 2, 2, 2, 2, 3, 1, 2, 2, 2, 2, 2, 2, 2, 2, 2, 3, 3, 4, 3, 3, 3, 3, 3, 1, 4.
	90 users	3, 2, 2, 2, 1, 1, 2, 2, 1, 2, 3, 2, 2, 3, 2, 2, 2, 2, 2, 2, 3, 2, 2, 2, 3, 2, 2, 3, 3, 2, 3, 3, 2, 3, 3, 3, 5, 3, 3, 3, 3, 2, 2, 3, 1, 3, 2, 2, 2, 2, 3, 3, 5, 3, 3, 3, 3, 3, 3, 3, 3, 1, 2, 2, 3, 2, 3, 2, 2, 2, 2, 1, 2, 2, 2, 2, 2, 2, 2, 2, 2, 3, 3, 1, 3, 3, 5, 3, 3, 3, 4.
	100 users	1, 2, 2, 1, 1, 1, 2, 2, 1, 2, 1, 2, 2, 2, 2, 2, 2, 2, 2, 2, 2, 2, 2, 2, 2, 3, 2, 2, 2, 3, 2, 3, 3, 2, 1, 3, 3, 2, 1, 1, 1, 1, 2, 2, 2, 2, 2, 2, 2, 2, 2, 3, 2, 2, 3, 1, 3, 2, 3, 3, 2, 1, 3, 1, 1, 1, 1, 5, 3, 1, 2, 1, 2, 2, 2, 2, 2, 2, 2, 2, 2, 1, 2, 2, 1, 2, 2, 2, 2, 2, 2, 1, 1, 4, 3, 1, 1, 3, 1, 3, 4.

Table 5.6: PDs ON for the case 2 under consideration

		Two PDs ON
ECQO-AO	20 users	1 3, 1 2, 2 1, 2 1, 1 2, 3 1, 2 1, 2 1, 1 2, 2 1, 3 2, 3 2, 1 2, 3 2, 3 2, 3 1, 1 3, 4 2, 1 3, 1 3.
	30 users	1 3, 1 2, 4 2, 1 3, 2 1, 2 1, 2 3, 3 2, 2 4, 3 1, 2 3, 1 4, 2 1, 1 2, 2 4, 1 3, 2 1, 4 2, 1 3, 3 1, 1 3, 1 2, 2 5, 2 4, 2 1, 2 5, 4 2, 3 1, 1 3, 3 4.
	40 users	2 1, 1 2, 4 2, 2 1, 4 2, 2 1, 3 2, 2 3, 4 2, 2 3, 5 2, 2 1, 3 2, 2 3, 3 1, 2 4, 2 5, 3 1, 2 1, 2 3, 1 3, 3 2, 3 2, 3 2, 2 3, 4 2, 1 5, 1 3, 1 3, 1 5, 1 2, 2 3, 1 2, 1 2, 1 2, 4 2, 3 5, 3 1, 3 5, 3 4.
	50 users	1 2, 2 4, 2 4, 2 1, 1 2, 1 2, 2 4, 4 2, 2 3, 2 3, 1 2, 3 1, 5 3, 2 3, 2 4, 1 2, 3 2, 1 2, 1 2, 2 4, 2 3, 2 4, 5 2, 3 4, 5 1, 2 3, 2 4, 2 3, 2 4, 1 5, 1 3, 3 1, 3 1, 5 3, 5 1, 1 3, 1 2, 3 2, 1 2, 2 5, 2 4, 1 5, 2 1, 2 1, 2 4, 1 3, 3 1, 4 1, 5 3, 3 1.
	60 users	3 2, 2 5, 2 1, 1 2, 3 2, 1 2, 2 4, 3 2, 2 3, 4 2, 1 3, 3 1, 5 2, 1 3, 3 1, 3 5, 2 4, 5 1, 1 3, 3 1, 1 5, 2 3, 5 2, 2 3, 5 2, 1 2, 2 4, 5 2, 2 3, 4 5, 1 3, 2 5, 5 2, 2 3, 1 3, 2 3, 2 4, 3 2, 1 2, 2 4, 1 3, 3 5, 5 1, 1 3, 3 5, 1 3, 3 5, 5 1, 1 3, 3 5, 2 1, 2 1, 2 5, 1 2, 2 5, 2 5, 2 5, 5 2, 1 2, 2 4.
	70 users	1 2, 2 4, 2 1, 2 3, 4 5, 4 2, 1 5, 4 2, 2 1, 2 4, 1 2, 2 3, 4 2, 1 2, 3 2, 4 2, 2 3, 5 3, 2 1, 2 5, 1 5, 1 3, 5 3, 2 5, 3 5, 3 1, 3 5, 5 2, 2 5, 4 5, 2 3, 2 5, 2 1, 4 5, 2 1, 3 2, 2 4, 3 1, 2 1, 4 2, 1 3, 3 5, 5 3, 2 5, 2 5, 1 2, 2 4, 5 1, 1 3, 1 5, 1 3, 3 5, 3 1, 5 3, 3 5, 1 3, 3 5, 2 1, 2 3, 3 5, 1 2, 3 4, 5 1, 2 1, 2 3, 1 2, 2 4, 5 1, 1 3, 4 5.
	80 users	1 2, 3 4, 5 1, 2 3, 4 5, 1 2, 3 4, 5 1, 2 3, 4 5, 1 2, 3 4, 5 1, 2 3, 4 5, 1 2, 3 4, 5 1, 2 3, 4 5, 1 2, 3 4, 5 1, 2 3, 4 5, 1 2, 3 4, 5 1, 2 3, 4 5, 1 2, 3 4, 5 1, 2 3, 4 5, 1 2, 3 4, 5 1, 2 3, 4 5, 1 2, 3 4, 5 1, 2 3, 4 5, 1 2, 3 4, 5 1, 2 3, 4 5, 1 2, 3 4, 5 1, 2 3, 4 5, 1 2, 3 4, 5 1, 2 3, 4 5, 1 2, 3 4, 5 1, 2 3, 4 5, 1 2, 3 4, 5 1, 2 3, 4 5, 1 2, 3 4, 5 1, 2 3, 4 5, 1 2, 3 4, 5 1, 2 3, 4 5.
	90 users	1 2, 3 2, 5 2, 1 3, 1 5, 1 4, 2 5, 5 2, 1 3, 4 2, 1 2, 2 5, 5 2, 2 3, 2 5, 1 2, 2 4, 5 2, 2 3, 4 5, 1 3, 2 3, 2 5, 5 2, 5 3, 1 2, 2 4, 3 2, 1 2, 4 5, 1 5, 3 1, 5 1, 3 4, 1 5, 1 2, 4 2, 5 1, 1 3, 4 5, 1 2, 2 3, 5 2, 2 3, 3 2, 2 3, 2 5, 2 1, 1 2, 2 4, 3 1, 3 5, 5 1, 5 2, 3 5, 1 3, 3 5, 5 3, 1 3, 3 5, 1 3, 3 5, 5 2, 2 5, 2 5, 1 2, 3 4, 5 2, 2 1, 2 4, 1 2, 2 5, 5 2, 2 3, 2 1, 1 2, 1 5, 5 1, 1 2, 2 5, 1 3, 3 5, 5 1, 2 3, 3 5, 1 5, 3 4, 5 1, 1 5, 4 5.
	100 users	1 2, 2 1, 4 1, 1 5, 1 2, 5 2, 2 4, 3 2, 2 3, 2 5, 1 2, 2 5, 4 2, 2 1, 2 5, 1 2, 4 5, 2 1, 1 5, 2 5, 1 2, 2 5, 5 1, 2 3, 3 2, 5 2, 2 4, 3 2, 3 5, 4 5, 1 3, 3 5, 5 2, 1 2, 3 5, 1 3, 2 5, 5 1, 1 2, 3 5, 1 2, 2 1, 5 2, 1 2, 2 5, 1 2, 2 5, 3 1, 1 5, 2 5, 1 3, 2 5, 5 2, 1 3, 5 1, 1 3, 2 5, 4 2, 2 5, 4 2, 1 3, 1 3, 5 1, 1 3, 1 5, 2 3, 3 5, 5 3, 1 5, 3 5, 1 2, 1 3, 5 2, 2 5, 2 5, 5 2, 2 5, 3 1, 3 5, 5 3, 1 5, 3 2, 3 2, 1 3, 3 5, 1 2, 4 5, 1 2, 2 5, 4 5, 1 3, 3 5, 5 1, 3 5, 3 5, 1 3, 3 1, 5 3, 3 1, 5 4.

GENERAL CONCLUSION

Visible light communication (VLC) is a new technology that has gained increasing attention in recent years as a potential solution for high-speed data transfer and wireless communication. VLC uses the visible light spectrum to transmit data and can be easily integrated with existing LED lighting systems.

The study presented in this document focuses on the application of visible light communication (VLC) technology in outdoor and indoor environments. The aim is to evaluate the performance of VLC systems in these different environments, taking into account different factors such as system parameters and environments requirements. The study assumes that the user is equipped with a VLC receiver module, which allows them to communicate with a VLC transmitter based on LEDs. The transmitter is located on a vehicle or traffic light in the case of an outdoor environment and on the ceiling in the case of an indoor environment.

The objective of this thesis is to provide insights into the challenges and opportunities of using VLC technology in outdoor and indoor environments, and to identify potential solutions for improving its performance in these environments. This could involve studying factors that affect VLC signal quality, such as light interference, signal strength, weather conditions, and noise levels. The thesis could also explore different optimization techniques that can be used to solve different problems and thus increase the data transfer rate and reliability of VLC systems. The ultimate goal is to improve the performance of VLC systems and make them more suitable for a wider range of applications.

In the first chapter of the thesis, a general overview of visible light communication (VLC) technology is presented. This chapter provides an introduction to the basic concepts of VLC, including its architecture, principles of communication, and different modulation techniques. The chapter also discusses the different domains of application for VLC, including indoor and outdoor environments, and highlights the advantages and limitations of VLC compared to other communication technologies. The goal of this chapter is to provide a comprehensive understanding of VLC technology, its key components, and

its potential applications. This chapter has been published in [165].

In the second chapter of the thesis, the theoretical foundation of the VLC channel is presented. This includes an analysis of the different link scenarios and the characterization of the VLC channel. The chapter starts with a discussion of the different types of VLC links, such as Light of sight (LoS) and Non ligne of sight (NLoS) links. It then goes on to describe the key channel characteristics of VLC, such as the path loss, channel impulse response, and channel gain. The chapter concludes with a classification of the different channel models based on the environment, including indoor and outdoor environments. This classification helps to identify the specific challenges associated with VLC in different environments and provides a basis for further analysis and optimization of VLC systems. It will be used in later chapters to evaluate the performance of VLC systems and to develop new techniques for improving their performance.

The third chapter describes the use of an angle diversity receiver to enhance the performance of vehicle-to-vehicle and vehicle-to-infrastructure-visible light communication systems. The effects of various system parameters on the performance of the system were studied by considering different positions of the car on the road. A performance comparison was made based on data rates, maximum achievable distance, and packet delivery ratio for different numbers of photodetectors. The results of this chapter have been published in [166, 109].

The study in chapter four aimed to enhance the V2V VLC system by incorporating an imaging receiver that utilized a polar detector in combination with various optical lenses, including Fresnel and Aspherical lenses. The integration of a double-convex lens and a half-Plano-concave lens was proposed as a novel design to correct for optical aberrations such as chromatic and spherical aberration. The proposed design was evaluated using non-sequential ray tracing tools and a realistic channel modeling study that considered the movement between the vehicles in both horizontal and vertical directions. The impact of key system parameters such as the receiver diameter and bandwidth on the overall V2V system performance was also analyzed. The results of this chapter have been published in [167, 168].

In chapter five, an efficient optimization scheme called Enhanced Chaotic Quasi- Opposition -based AO (ECQO-AO) was proposed to address the resource allocation problem in an indoor Multi-user Internet of Things-Visible Light Communication. The proposed ECQO-AO combines chaotic map, QOBL mechanism, FDB selection method, and cosine function into the original Aquila Optimization algorithm. The performance of ECQO-AO was evaluated by considering different numbers of users and photodetectors and compared with various state-of-the-art algorithms.

Perspectives:

In future perspectives, the proposed vehicular VLC system models can be evaluated in terms of their outage performance, with the aim of improving their reliability and robustness. Enhancing the security of the system against cyber threats, such as eavesdropping and jamming, is also important. Another avenue of future work is to explore the hybridization of VLC and millimeter wave (mmWave) technologies to improve system quality and extend the communication distance.

Additionally, the application of multi-objective algorithms can be explored to solve the various optimization problems in indoor VLC systems. These algorithms can help balance conflicting objectives, such as maximizing data rate and minimizing energy consumption, and provide more robust and efficient solutions.

BIBLIOGRAPHY

[1] Mohaiminul Islam and Shangzhu Jin. An overview research on wireless communication network. *Networks*, 5(1):19–28, 2019.

[2] Cem Sahin, Danh Nguyen, Simon Begashaw, Brandon Katz, James Chacko, Logan Henderson, Jennifer Stanford, and Kapil R Dandekar. Wireless communications engineering education via augmented reality. In *2016 IEEE frontiers in education conference (FIE)*, pages 1–7. IEEE, 2016.

[3] `https://www.itu.int/en/ITU-D/Statistics/Documents/facts/FactsFigures2021.pdf`. [Accessed: May 17, 2023].

[4] Zabih Ghassemlooy, Shlomi Arnon, Murat Uysal, Zhengyuan Xu, and Julian Cheng. Emerging optical wireless communications-advances and challenges. *IEEE journal on selected areas in communications*, 33(9):1738–1749, 2015.

[5] Toshihiko Komine and Masao Nakagawa. Fundamental analysis for visible-light communication system using LED lights. *IEEE transactions on Consumer Electronics*, 50(1):100–107, 2004.

[6] Svilen Dimitrov and Harald Haas. *Principles of LED light communications: towards networked Li-Fi*. Cambridge University Press, 2015.

[7] Zahra Nazari Chaleshtori, Zabih Ghassemlooy, Hossien B. Eldeeb, Murat Uysal, and Stanislav Zvanovec. Utilization of an OLED-based VLC system in office, corridor, and semi-open corridor environments. *Sensors*, 20(23), 2020.

[8] Hossien B Eldeeb, Mohamed Al-Nahhal, Hossam AI Selmy, and Fathi E Abd El-Samie. Continuous phase modulation with chaotic interleaving for visible light communication systems based on orthogonal frequency division multiplexing. *Transactions on Emerging Telecommunications Technologies*, 31(10):e4100, 2020.

[9] Lifang Feng, Rose Qingyang Hu, Jianping Wang, Peng Xu, and Yi Qian. Applying VLC in 5G networks: Architectures and key technologies. *IEEE Network*, 30(6):77–83, 2016.

[10] Hossien B. Eldeeb, Hossam A. I. Selmy, Hany M. Elsayed, Ragia I. Badr, and Murat Uysal. Efficient resource allocation scheme for multi-user hybrid VLC/IR networks. In *2019 IEEE Photon. Conf. (IPC)*, pages 1–2, 2019.

[11] Murat Uysal, Zabih Ghassemlooy, Abdelmoula Bekkali, Abdullah Kadri, and Hamid Menouar. Visible light communication for vehicular networking: Performance study of a V2V system using a measured headlamp beam pattern model. *IEEE Veh. Technol. Mag.*, 10(4):45–53, 2015.

[12] David N Amanor, William W Edmonson, and Fatemeh Afghah. Intersatellite communication system based on visible light. *IEEE Transactions on Aerospace and Electronic Systems*, 54(6):2888–2899, 2018.

[13] K Mahalakshmi, K Shantha Kumari, D Yuvaraj, R Keerthika, et al. Healthcare visible light communication. *International Journal of Pure and Applied Mathematics*, 118(11):345–348, 2018.

[14] Mohammed Elamassie, Farshad Miramirkhani, and Murat Uysal. Performance characterization of underwater visible light communication. *IEEE Transactions on Communications*, 67(1):543–552, 2018.

[15] Gerard J Holzmann and William Slattery Lieberman. *Design and validation of computer protocols*, volume 512. Prentice hall Englewood Cliffs, 1991.

[16] Jean-Marie Dilhac. The telegraph of claude chappe-an optical telecommunication network for the xviiith century. *Institut National des Sciences Appliquées de Toulouse*, pages 1–8, 2001.

[17] Yuichi Tanaka, Toshihiko Komine, Shinichiro Haruyama, and Masao Nakagawa. Indoor visible light data transmission system utilizing white LED lights. *IEICE transactions on communications*, 86(8):2440–2454, 2003.

[18] Sang Hyun Lee, Sung-Yoon Jung, and Jae Kyun Kwon. Modulation and coding for dimmable visible light communication. *IEEE Communications Magazine*, 53(2):136–143, 2015.

[19] Javier Sebastián, Diego G Lamar, Daniel G Aller, Juan Rodríguez, and Pablo F Miaja. On the role of power electronics in visible light communication. *IEEE Journal of Emerging and Selected Topics in Power Electronics*, 6(3):1210–1223, 2018.

[20] Luiz Eduardo Mendes Matheus, Alex Borges Vieira, Luiz FM Vieira, Marcos AM Vieira, and Omprakash Gnawali. Visible light communication: concepts, applications and challenges. *IEEE Communications Surveys & Tutorials*, 21(4):3204–3237, 2019.

[21] Dilukshan Karunatilaka, Fahad Zafar, Vineetha Kalavally, and Rajendran Parthiban. LED based indoor visible light communications: State of the art. *IEEE Communications Surveys & Tutorials*, 17(3):1649–1678, 2015.

[22] Zheng-Guo Sun, Hong-Yi Yu, and Yi-Jun Zhu. Superposition constellation design for multi-user multi-chip visible light communication systems. *Optics Communications*, 432:27–31, 2019.

[23] Hossien B Eldeeb, Hossam AI Selmy, Hany M Elsayed, and Ragia I Badr. Co-channel interference cancellation using constraint field of view ADR in VLC channel. In *2017 IEEE Photonics Conference (IPC) Part II*, pages 1–2. IEEE, 2017.

[24] Alain Richard Ndjiongue, Hendrik C Ferreira, and Telex MN Ngatched. Visible light communications (VLC) technology. *Wiley Encyclopedia of Electrical and Electronics Engineering*, pages 1–15, 1999.

[25] Ahmed A Abdulhussain Al-Kinani et al. *Channel modelling for visible light communication systems*. PhD thesis, Heriot-Watt University, 2018.

[26] H Joshi, RJ Green, and MS Leeson. Channel models for optical wireless communication systems. In *11th International Conference on Transparent Optical Networks, ICTON*, volume 9, pages 1–5, 2009.

[27] Zabih Ghassemlooy, Wasiu Popoola, and Sujan Rajbhandari. *Optical wireless communications: system and channel modelling with Matlab®*. CRC press, 2019.

[28] Latif Ullah Khan. Visible light communication: Applications, architecture, standardization and research challenges. *Digital Communications and Networks*, 3(2):78–88, 2017.

[29] Fengyu Che, Liang Wu, Babar Hussain, Xianbo Li, and C Patrick Yue. A fully integrated IEEE 802.15. 7 visible light communication transmitter with on-chip 8-w 85% efficiency boost LED driver. *Journal of Lightwave Technology*, 34(10):2419–2430, 2016.

[30] AM Zaiton, CH Eng, and F Jasman. Pulse position modulation characterization for indoor visible light communication system. In *Journal of Physics: Conference Series*, volume 1502, page 012005. IOP Publishing, 2020.

[31] Cihun-Siyong Alex Gong, Yu-Chen Lee, Jyun-Liang Lai, Chueh-Hao Yu, Li Ren Huang, and Chia-Yen Yang. The high-efficiency LED driver for visible light communication applications. *Scientific reports*, 6(1):1–7, 2016.

[32] Parth H Pathak, Xiaotao Feng, Pengfei Hu, and Prasant Mohapatra. Visible light communication, networking, and sensing: A survey, potential and challenges. *IEEE communications surveys & tutorials*, 17(4):2047–2077, 2015.

[33] Harald Haas, Liang Yin, Yunlu Wang, and Cheng Chen. What is lifi? *Journal of lightwave technology*, 34(6):1533–1544, 2015.

[34] Lamya I Albraheem, Lamia H Alhudaithy, Afnan A Aljaser, Muneerah R Aldhafian, and Ghada M Bahliwah. Toward designing a Li-Fi-based hierarchical IoT architecture. *IEEE access*, 6:40811–40825, 2018.

[35] Se-Hoon Yang, Hyun-Seung Kim, Yong-Hwan Son, and Sang-Kook Han. Three-dimensional visible light indoor localization using aoa and rss with multiple optical receivers. *Journal of Lightwave Technology*, 32(14):2480–2485, 2014.

[36] Marwa M El Gamal, R Maheswar, Heba A Fayed, Moustafa H Aly, Nour Eldin Ismail, and Amr Mokhtar. Dark light visible light communication positioning system with received signal strength technique. *Optical and Quantum Electronics*, 53(9):1–16, 2021.

[37] Agon Memedi and Falko Dressler. Vehicular visible light communications: A survey. *IEEE Commun. Surv. Tutor.*, 23(1):161–181, 2020.

[38] Xuan Li, Rong Zhang, and Lajos Hanzo. Optimization of visible-light optical wireless systems: Network-centric versus user-centric designs. *IEEE Communications Surveys & Tutorials*, 20(3):1878–1904, 2018.

[39] Suseela Vappangi and VV Mani. Concurrent illumination and communication: A survey on visible light communication. *Physical Communication*, 33:90–114, 2019.

[40] Mohanad Obeed, Anas M Salhab, Mohamed-Slim Alouini, and Salam A Zummo. On optimizing vlc networks for downlink multi-user transmission: A survey. *IEEE Communications Surveys & Tutorials*, 21(3):2947–2976, 2019.

[41] Ahmed Al-Kinani, Cheng-Xiang Wang, Li Zhou, and Wensheng Zhang. Optical wireless communication channel measurements and models. *IEEE Communications Surveys & Tutorials*, 20(3):1939–1962, 2018.

[42] D Wu, Z Ghassemlooy, S Rajbhandari, and H Le Minh. Channel characteristics analysis and experimental demonstration of a diffuse cellular indoor visible light

communication system. *The Mediterranean Journal of Electronics and Communications*, 8:1–7, 2012.

[43] Olivier Bouchet. *Wireless Optical Communications*. John Wiley & Sons, 2013.

[44] R Ramirez-Iniguez and RJ Green. Indoor optical wireless communications. 1999.

[45] Yazan A Alqudah and Mohsen Kavehrad. MIMO characterization of indoor wireless optical link using a diffuse-transmission configuration. *IEEE Transactions on Communications*, 51(9):1554–1560, 2003.

[46] Volker Jungnickel, Volker Pohl, Stephan Nonnig, and Clemens Von Helmolt. A physical model of the wireless infrared communication channel. *IEEE Journal on Selected Areas in Communications*, 20(3):631–640, 2002.

[47] David R Wisely. A 1 Gbit/s optical wireless tracked architecture for ATM delivery. 1996.

[48] Philip Mark. *Ethernet over light*. PhD thesis, University of British Columbia, 2014.

[49] Hany Elgala, Raed Mesleh, and Harald Haas. Indoor optical wireless communication: potential and state-of-the-art. *IEEE Communications Magazine*, 49(9):56–62, 2011.

[50] Matthew D Higgins, Roger J Green, and Mark S Leeson. A genetic algorithm method for optical wireless channel control. *Journal of Lightwave Technology*, 27(6):760–772, 2009.

[51] Joseph M Kahn and John R Barry. Wireless infrared communications. *Proceedings of the IEEE*, 85(2):265–298, 1997.

[52] Francisco J Lopez-Hernandez, Rafael Perez-Jimenez, and Asuncion Santamaria. Ray-tracing algorithms for fast calculation of the channel impulse response on diffuse ir wireless indoor channels. *Optical engineering*, 39(10):2775–2781, 2000.

[53] Abdul Salam and Mehmet C Vuran. Em-based wireless underground sensor networks. In *Underground sensing*, pages 247–285. Elsevier, 2018.

[54] Jeffrey B Carruthers and Joseph M Kahn. Modeling of nondirected wireless infrared channels. *IEEE transactions on communications*, 45(10):1260–1268, 1997.

[55] Cheng Chen, Dushyantha A Basnayaka, Xiping Wu, and Harald Haas. Efficient analytical calculation of non-line-of-sight channel impulse response in visible light communications. *Journal of Lightwave Technology*, 36(9):1666–1682, 2017.

[56] Yang Qiu, Hsiao-Hwa Chen, and Wei-Xiao Meng. Channel modeling for visible light communicationsa survey. *Wireless Communications and Mobile Computing*, 16(14):2016–2034, 2016.

[57] John R. Barry, Joseph M. Kahn, William J. Krause, Edward A. Lee, and David G. Messerschmitt. Simulation of multipath impulse response for indoor wireless optical channels. *IEEE journal on selected areas in communications*, 11(3):367–379, 1993.

[58] Ahmed Al-Kinani, Cheng-Xiang Wang, Harald Haas, and Yang Yang. A geometry-based multiple bounce model for visible light communication channels. In *2016 International Wireless Communications and Mobile Computing Conference (IWCMC)*, pages 31–37. IEEE, 2016.

[59] AM Ramirez-Aguilera, JM Luna-Rivera, Victor Guerra, José Rabadán, Rafael Perez-Jimenez, and Francisco J Lopez-Hernandez. A review of indoor channel modeling techniques for visible light communications. In *2018 IEEE 10th Latin-American Conference on Communications (LATINCOM)*, pages 1–6. IEEE, 2018.

[60] Mohamed DA Mohamed and Steve Hranilovic. Optical impulse modulation for indoor diffuse wireless communications. *IEEE transactions on communications*, 57(2):499–508, 2009.

[61] Dehao Wu, Zabih Ghassemlooy, Hoa Le Minh, Sujan Rajbhandari, and Anthony C Boucouvalas. Improvement of the transmission bandwidth for indoor optical wireless communication systems using a diffused gaussian beam. *IEEE communications letters*, 16(8):1316–1319, 2012.

[62] Jupeng Ding, Zhengyuan Xu, and Lajos Hanzo. Accuracy of the point-source model of a multi-LED array in high-speed visible light communication channel characterization. *IEEE Photonics Journal*, 7(4):1–14, 2015.

[63] Shihe Long, Mohammad Ali Khalighi, Mike Wolf, Salah Bourennane, and Zabih Ghassemlooy. Investigating channel frequency selectivity in indoor visible-light communication systems. *Iet Optoelectronics*, 10(3):80–88, 2016.

[64] Jelena Grubor, Sebastian Randel, Klaus-Dieter Langer, and Joachim W Walewski. Broadband information broadcasting using LED-based interior lighting. *Journal of Lightwave technology*, 26(24):3883–3892, 2008.

[65] Harald Haas, Cheng Chen, and Dominic O'Brien. A guide to wireless networking by light. *Progress in Quantum Electronics*, 55:88–111, 2017.

[66] M Ghaddar, L Talbi, and GY Delisle. Coherence bandwidth measurement in indoor broadband propagation channel at unlicensed 60 ghz band. *Electronics letters*, 48(13):795–797, 2012.

[67] Radu Mitran and Mircea Stanic. Delay spread evaluation of hf channels based on ray tracing. In *2016 IEEE International Black Sea Conference on Communications and Networking (BlackSeaCom)*, pages 1–5. IEEE, 2016.

[68] Fritz R Gfeller and Urs Bapst. Wireless in-house data communication via diffuse infrared radiation. *Proceedings of the IEEE*, 67(11):1474–1486, 1979.

[69] Jeffrey B Carruthers and Prasanna Kannan. Iterative site-based modeling for wireless infrared channels. *IEEE Transactions on Antennas and Propagation*, 50(5):759–765, 2002.

[70] Farshad Miramirkhani and Murat Uysal. Channel modelling for indoor visible light communications. *Philosophical Transactions of the Royal Society A*, 378(2169):20190187, 2020.

[71] Xuefeng Yin and Xiang Cheng. *Propagation channel characterization, parameter estimation, and modeling for wireless communications*. John Wiley & Sons, 2016.

[72] Shun-Hsiang Yu, Oliver Shih, Hsin-Mu Tsai, Nawaporn Wisitpongphan, and Richard D Roberts. Smart automotive lighting for vehicle safety. *IEEE Commun. Mag.*, 51(12):50–59, 2013.

[73] Hossien B Eldeeb, Elizabeth Eso, Elnaz Alizadeh Jarchlo, Stanislav Zvanovec, Murat Uysal, Zabih Ghassemlooy, and Juna Sathian. Vehicular VLC: A ray tracing study based on measured radiation patterns of commercial taillights. *IEEE Photonics Technol. Lett.*, 33(16):904–907, 2021.

[74] Bugra Turan, Gokhan Gurbilek, Ali Uyrus, and Sinem Coleri Ergen. Vehicular VLC frequency domain channel sounding and characterization. In *2018 IEEE Veh. Netw. Conf. (VNC)*, pages 1–8. IEEE, 2018.

[75] Hossien B Eldeeb, Farshad Miramirkhani, and Murat Uysal. A path loss model for vehicle-to-vehicle visible light communications. In *2019 15th Int. Conf. Telecommun. (ConTEL)*, pages 1–5. IEEE, 2019.

[76] Mehdi Karbalayghareh, Farshad Miramirkhani, Hossein B Eldeeb, Refik Caglar Kizilirmak, Sadiq M Sait, and Murat Uysal. Channel modelling and performance limits of vehicular visible light communication systems. *IEEE Transactions on Vehicular Technology*, 2020.

[77] Pengfei Luo, Zabih Ghassemlooy, Hoa Le Minh, Edward Bentley, Andrew Burton, and Xuan Tang. Performance analysis of a car-to-car visible light communication system. *Appl. Opt.*, 54(7):1696–1706, 2015.

[78] Hossien B Eldeeb and Murat Uysal. Vehicle-to-vehicle visible light communication: How to select receiver locations for optimal performance? In *2019 11th Int. Conf. Electr. Electron. Eng. (ELECO)*, pages 402–405. IEEE, 2019.

[79] Ahmed Al-Kinani, Cheng-Xiang Wang, Qiuming Zhu, Yu Fu, El-Hadi M Aggoune, Ahmed Talib, and Nidaa A Al-Hasaani. A 3D non-stationary GBSM for vehicular visible light communication MISO channels. *IEEE Access*, 8:140333–140347, 2020.

[80] Bassam Aly, Mohammed Elamassie, Hossien B Eldeeb, and Murat Uysal. Experimental investigation of lens combinations on the performance of vehicular VLC. In *2020 12th Int. Symp. Commun. Syst. Netw. Digit. Signal Process (CSNDSP)*, pages 1–5. IEEE, 2020.

[81] Zongmin Cui, Peng Yue, Xiang Yi, and Jing Li. Research on non-uniform dynamic vehicle-mounted VLC with receiver spatial and angular diversity. In *ICC 2019-2019 IEEE Int. Conf. Commun. (ICC)*, pages 1–7. IEEE, 2019.

[82] Xiaotong Shen and Harald Haas. Vehicle to infrastructure vlc channel models. In *2020 IEEE 91st Vehicular Technology Conference (VTC2020-Spring)*, pages 1–5. IEEE, 2020.

[83] Hyeon-Cheol Kim, Byung-Wook Kim, and Sung-Yoon Jung. Performance of a wavelength hopping mc-vppm scheme for vehicle-to-infrastructure (v2i) vlc. *Photonic Network Communications*, 33(1):60–68, 2017.

[84] Hossien B Eldeeb, Hossam AI Selmy, Hany M Elsayed, and Ragia I Badr. Interference mitigation and capacity enhancement using constraint field of view ADR in downlink VLC channel. *IET Commun.*, 12(16):1968–1978, 2018.

[85] Fuad E Alsaadi and Jaafar MH Elmirghani. Mobile multigigabit indoor optical wireless systems employing multibeam power adaptation and imaging diversity receivers. *J. Opt. Commun. Netw.*, 3(1):27–39, 2011.

[86] Shuai Ma, Zhi-Long Dong, Hang Li, Zhaolin Lu, and Shiyin Li. Optimal and robust secure beamformer for indoor MISO visible light communication. *J. Light. Technol.*, 34(21):4988–4998, 2016.

[87] Hossien B. Eldeeb, Mohammed Elamassie, and Murat Uysal. Vehicle-to-infrastructure visible light communications: Channel modelling and capacity calcu-

lations. In *2020 12th International Symposium on Communication Systems, Networks and Digital Signal Processing (CSNDSP)*, pages 1–6, 2020.

[88] Ayman Mostafa and Lutz Lampe. Physical-layer security for MISO visible light communication channels. *IEEE J. Sel. Areas Commun.*, 33(9):1806–1818, 2015.

[89] Jun-Bo Wang, Qing-Song Hu, Jiangzhou Wang, Ming Chen, and Jin-Yuan Wang. Tight bounds on channel capacity for dimmable visible light communications. *J. Light. Technol.*, 31(23):3771–3779, 2013.

[90] Liang Yin and Harald Haas. Physical-layer security in multiuser visible light communication networks. *IEEE J. Sel. Areas Commun.*, 36(1):162–174, 2017.

[91] Agon Memedi, Hsin-Mu Tsai, and Falko Dressler. Impact of realistic light radiation pattern on vehicular visible light communication. In *GLOBECOM 2017-2017 IEEE Global Communications Conference*, pages 1–6. IEEE, 2017.

[92] Osram BPY 62. `https://dammedia.osram.info/media/resource/hires/osram-dam-5452317/BPY\%2062_EN.pdf/`. [Accessed: May 17, 2023].

[93] SFH 213. `https://www.osram.com/ecat/RadialT134SFH213/com/en/class\_pim\_web\_catalog\_103489\\/prd\_pim\_device\_2219559/`. [Accessed: May 17, 2023].

[94] SFH 213 FA. `https://www.osram.com/ecat/Radial\%20T1\%203-4\%20SFH\%20213\%20FA/com/en/class\_pim\_web\_catalog\_103489/prd\_pim\_device\_2219560/`. [Accessed: May 17, 2023].

[95] Elizabeth Eso, Zabih Ghassemlooy, Stanislav Zvanovec, Juna Sathian, Mojtaba Mansour Abadi, and Othman Isam Younus. Performance of vehicular visible light communications under the effects of atmospheric turbulence with aperture averaging. *Sensors*, 21(8):2751, 2021.

[96] Mohammed Elamassie, Mehdi Karbalayghareh, Farshad Miramirkhani, Refik Caglar Kizilirmak, and Murat Uysal. Effect of fog and rain on the performance of vehicular visible light communications. In *2018 IEEE 87th IEEE Veh. Technol. Conf. (VTC Spring)*, pages 1–6. IEEE, 2018.

[97] Sebastian-Andrei Avătămăniei, Cătălin Beguni, Alin-Mihai Căilean, Mihai Dimian, and Valentin Popa. Evaluation of misalignment effect in vehicle-to-vehicle visible light communications: Experimental demonstration of a 75 meters link. *J. Sens.*, 21(11):3577, 2021.

[98] J-H Yoo, J-S Jang, JK Kwon, H-C Kim, D-W Song, and S-Y Jung. Demonstration of vehicular visible light communication based on LED headlamp. *Int. J. Automot. Technol.*, 17(2):347–352, 2016.

[99] Takaya Yamazato, Masayuki Kinoshita, Shintaro Arai, Eisho Souke, Tomohiro Yendo, Toshiaki Fujii, Koji Kamakura, and Hiraku Okada. Vehicle motion and pixel illumination modeling for image sensor based visible light communication. *IEEE Journal on Selected Areas in Communications*, 33(9):1793–1805, 2015.

[100] Asanka Nuwanpriya, Siu-Wai Ho, and Chung Shue Chen. Indoor MIMO visible light communications: Novel angle diversity receivers for mobile users. *IEEE J. Sel. Areas Commun.*, 33(9):1780–1792, 2015.

[101] Pablo Palacios Játiva, Cesar A Azurdia-Meza, Milton Román Cañizares, Sandra Céspedes, and Samuel Montejo-Sánchez. Performance enhancement of VLC-based systems using diversity combining schemes in the receiver. In *2019 IEEE Latin-American Conference on Communications (LATINCOM)*, pages 1–6. IEEE, 2019.

[102] Zhe Chen, Dobroslav Tsonev, and Harald Haas. Improving SINR in indoor cellular visible light communication networks. In *2014 IEEE International Conference on Communications (ICC)*, pages 3383–3388. IEEE, 2014.

[103] Rui Jiang, Zhaocheng Wang, Qi Wang, and Linglong Dai. A tight upper bound on channel capacity for visible light communications. *IEEE Communications Letters*, 20(1):97–100, 2015.

[104] JB Carruther and Joseph M Kahn. Angle diversity for nondirected wireless infrared communication. *IEEE Trans. Commun.*, 48(6):960–969, 2000.

[105] Hossien B Eldeeb, Mohammed Elamassie, and Murat Uysal. Vehicle-to-infrastructure visible light communications: Channel modelling and capacity calculations. In *2020 12th International Symposium on Communication Systems, Networks and Digital Signal Processing (CSNDSP)*, pages 1–6. IEEE, 2020.

[106] W Adrian and R Jobanputra. Influence of pavement reflectance on lighting for parking lots, 2005.

[107] Audi A8. `https://www.audiusa.com/us/web/en/models/a8/a8-sedan/2021/overview.html`. [Accessed: May 17, 2023].

[108] Maged Fakirah, Supeng Leng, Xiaosha Chen, and Jihua Zhou. Visible light communication-based traffic control of autonomous vehicles at multi-lane roundabouts. *EURASIP Journal on Wireless Communications and Networking*, 2020(1):1–14, 2020.

[109] Selma Yahia, Yassine Meraihi, Asma Benmessaoud Gabis, and Amar Ramdane-Cherif. Multi-directional vehicle-to-vehicle visible light communication with angular diversity technology. In *2020 2nd International Workshop on Human-Centric Smart Environments for Health and Well-being (IHSH)*, pages 160–164. IEEE, 2021.

[110] Máximo Morales-Céspedes, Ahmad Adnan Quidan, and Ana García Armada. Experimental evaluation of the reconfigurable photodetector for blind interference alignment in visible light communications. In *2019 27th Eur. Signal Process. Conf. (EUSIPCO)*, pages 1–5. IEEE, 2019.

[111] Thomas Q Wang, Y Ahmet Sekercioglu, and Jean Armstrong. Analysis of an optical wireless receiver using a hemispherical lens with application in MIMO visible light communications. *J. Light. Technol.*, 31(11):1744–1754, 2013.

[112] KVS Sai Sushanth and A Chockalingam. Performance of imaging receivers using convex lens in indoor MIMO VLC systems. In *2018 IEEE 87th Veh. Technol. Conf. (VTC Spring)*, pages 1–5. IEEE, 2018.

[113] Katrina D Dambul, Dominic C O'Brien, and Grahame Faulkner. Indoor optical wireless MIMO system with an imaging receiver. *IEEE Photonics Technol. Lett.*, 23(2):97–99, 2010.

[114] Thomas Q Wang, Y Ahmet Sekercioglu, and Jean Armstrong. Hemispherical lens based imaging receiver for MIMO optical wireless communications. In *2012 IEEE Globecom Workshops*, pages 1239–1243. IEEE, 2012.

[115] Baolong Li, Xiaoquan Lai, Jiaheng Wang, Xiao Liang, and Chunming Zhao. Performance analysis of the imaging receivers using a hemispherical lens for visible light communications. In *2013 International Conference on Wireless Communications and Signal Processing*, pages 1–5. IEEE, 2013.

[116] Te Chen, Lu Liu, Zhong Zheng, Jie Song, Kai Wu, and Weiwei Hu. Fisheye-lens-based space division multiplexing system for visible light communications. *EURASIP J Wirel Commun Netw*, 2015(1):1–7, 2015.

[117] Te Chen, Lu Liu, Bo Tu, Zhong Zheng, and Weiwei Hu. High-spatial-diversity imaging receiver using fisheye lens for indoor MIMO VLCs. *IEEE Photonics Technol. Lett.*, 26(22):2260–2263, 2014.

[118] Tian Lang, Zening Li, Albert Wang, and Gang Chen. Hemispherical lens featured beehive structure receiver on vehicular massive MIMO visible light communication system. In *International Conference on Internet of Vehicles*, pages 469–477. Springer, 2015.

[119] Sandrine Auriol. https://support.zemax.com/hc/en-us/articles/1500005488861-Understanding-the-Detector-Polar. [Accessed: May 17, 2023].

[120] Fernando Erismann. Design of a plastic aspheric fresnel lens with a spherical shape. *Opt. Eng.*, 36(4):988–991, 1997.

[121] Yong-Hyeon Kim, Willy Anugrah Cahyadi, and Yeon Ho Chung. Experimental demonstration of LED-based vehicle to vehicle communication under atmospheric turbulence. In *2015 Int. Conf. Inf. Commun. Technol. Converg. (ICTC)*, pages 1143–1145. IEEE, 2015.

[122] René Kirrbach, Michael Faulwaßer, and Benjamin Jakob. Non-rotationally symmetric freeform fresnel-lenses for arbitrary shaped Li-Fi communication channels. In *2019 Glob. LIFI Congr. (GLC)*, pages 1–6. IEEE, 2019.

[123] Warren J Smith. Modern optical engineering: the design of optical systems. *Modern optical engineering: the design of optical systems*, 2000.

[124] Weifan Li, Feng Qi, Yelong Wang, Pengxiang Liu, and Zhaoyang Liu. Refractive aspherical lens for terahertz imaging. *Opt. Commun.*, 433:14–17, 2019.

[125] Eugene Hecht. *Optics, 5e.* Pearson Education India, 2002.

[126] Akash Gupta, Parul Garg, and Nikhil Sharma. Hard switching-based hybrid RF/VLC system and its performance evaluation. *Trans. Emerg. Telecommun. Technol.*, 30(2):e3515, 2019.

[127] Zhaocheng Wang, Qi Wang, Wei Huang, and Zhengyuan Xu. *Visible light communications: modulation and signal processing.* John Wiley & Sons, 2017.

[128] Khadija Ashraf, SM Towhidul Islam, Akram Sadat Hosseini, and Ashwin Ashok. Motion characterization for vehicular visible light communications. In *2019 11th Int. Conf. Commun. Syst. Netw. (COMSNETS)*, pages 759–764. IEEE, 2019.

[129] Aspheric Lens. https://www.edmundoptics.fr/f/condenser-lenses-731b9cef/12868/. [Accessed: May 17, 2023].

[130] Fresnel Lens. https://www.edmundoptics.fr/f/aspherically-contoured-fresnel-lenses/12432/. [Accessed: May 17, 2023].

[131] Godfrey Anuga Akpakwu, Bruno J Silva, Gerhard P Hancke, and Adnan M Abu-Mahfouz. A survey on 5G networks for the internet of things: Communication technologies and challenges. *IEEE access*, 6:3619–3647, 2017.

[132] Bassem Khalfi, Bechir Hamdaoui, and Mohsen Guizani. Extracting and exploiting inherent sparsity for efficient IoT support in 5G: Challenges and potential solutions. *IEEE Wireless Communications*, 24(5):68–73, 2017.

[133] Antonio Iera, Christian Floerkemeier, Jin Mitsugi, and Giacomo Morabito. The internet of things [guest editorial]. *IEEE Wireless Communications*, 17(6):8–9, 2010.

[134] Ala Al-Fuqaha, Mohsen Guizani, Mehdi Mohammadi, Mohammed Aledhari, and Moussa Ayyash. Internet of things: A survey on enabling technologies, protocols, and applications. *IEEE communications surveys & tutorials*, 17(4):2347–2376, 2015.

[135] Fan Jin, Xuan Li, Rong Zhang, Chen Dong, and Lajos Hanzo. Resource allocation under delay-guarantee constraints for visible-light communication. *IEEE Access*, 4:7301–7312, 2016.

[136] Fabián Seguel, Ismael Soto, Daniel Iturralde, Pablo Adasme, and Belarmino Nuñez. Enhancement of the QoS in an OFDMA/VLC system. In *2016 10th International Symposium on Communication Systems, Networks and Digital Signal Processing (CSNDSP)*, pages 1–5. IEEE, 2016.

[137] Simeng Feng, Rong Zhang, Xuan Li, Qi Wang, and Lajos Hanzo. Dynamic throughput maximization for the user-centric visible light downlink in the face of practical considerations. *IEEE Transactions on Wireless Communications*, 17(8):5001–5015, 2018.

[138] Muhammet Selim Demir, Sadiq M Sait, and Murat Uysal. Unified resource allocation and mobility management technique using particle swarm optimization for VLC networks. *IEEE Photonics Journal*, 10(6):1–9, 2018.

[139] Muhammet Selim Demir, Ömer Faruk Gemici, and Murat Uysal. Genetic algortihm based resource allocation technique for VLC networks. In *2017 25th Signal processing and communications applications conference (SIU)*, pages 1–4. IEEE, 2017.

[140] Umair F Siddiqi, Sadiq M Sait, M Selim Demir, and Murat Uysal. Resource allocation for visible light communication systems using simulated annealing based on a problem-specific neighbor function. *IEEE Access*, 7:64077–64091, 2019.

[141] Hossien B. Eldeeb, Mona Hosney, Hany M. Elsayed, Ragia I. Badr, Murat Uysal, and Hossam A. I. Selmy. Optimal resource allocation and interference management for multi-user uplink light communication systems with angular diversity technology. *IEEE Access*, 8:203224–203236, 2020.

[142] Helin Yang, Wen-De Zhong, Chen Chen, Arokiaswami Alphones, Pengfei Du, Sheng Zhang, and Xianzhong Xie. Coordinated resource allocation-based integrated visible

light communication and positioning systems for indoor IoT. *IEEE Transactions on Wireless Communications*, 19(7):4671–4684, 2020.

[143] Shiyao Chang, Chen Gong, Nuo Huang, and Zhengyuan Xu. Indoor visible light communication scheduling for IoT scenarios with short blocklength. In *2020 IEEE/CIC International Conference on Communications in China (ICCC Workshops)*, pages 185–190. IEEE, 2020.

[144] Sifat Ibne Mushfique, Akash Dey, Ahmad Alsharoa, and Murat Yuksel. Resource optimization in visible light communication for internet of things. In *2019 IEEE International Symposium on Local and Metropolitan Area Networks (LANMAN)*, pages 1–6. IEEE, 2019.

[145] Murat Uysal, Farshad Miramirkhani, Tuncer Baykas, and Khalid Qaraqe. IEEE 802.11 bb reference channel models for indoor environments. Technical report, 2018.

[146] Yusuf Said Eroglu, Alphan Sahin, Ismail Guvenc, Nezih Pala, and Murat Yuksel. Multi-element transmitter design and performance evaluation for visible light communication. In *2015 IEEE Globecom Workshops (GC Wkshps)*, pages 1–6. IEEE, 2015.

[147] Laith Abualigah, Dalia Yousri, Mohamed Abd Elaziz, Ahmed A Ewees, Mohammed AA Al-qaness, and Amir H Gandomi. Aquila optimizer: A novel meta-heuristic optimization algorithm. *Computers & Industrial Engineering*, 157:107250, 2021.

[148] Shuang Wang, Heming Jia, Laith Abualigah, Qingxin Liu, and Rong Zheng. An improved hybrid aquila optimizer and harris hawks algorithm for solving industrial engineering optimization problems. *Processes*, 9(9):1551, 2021.

[149] Yu-Jun Zhang, Yu-Xin Yan, Juan Zhao, and Zheng-Ming Gao. AOAAO: The hybrid algorithm of arithmetic optimization algorithm with aquila optimizer. *IEEE Access*, 10:10907–10933, 2022.

[150] Juan Zhao, Zheng-Ming Gao, and Hua-Feng Chen. The simplified aquila optimization algorithm. *IEEE Access*, 10:22487–22515, 2022.

[151] D Carrasco-Olivera, C Morales, and H Villavicencio. Stability and expansivity of tent map. *Proceedings of the American Mathematical Society*, 149(2):773–786, 2021.

[152] Hamid R Tizhoosh. Opposition-based learning: a new scheme for machine intelligence. In *International conference on computational intelligence for modelling,*

control and automation and international conference on intelligent agents, web technologies and internet commerce (CIMCA-IAWTIC'06), volume 1, pages 695–701. IEEE, 2005.

[153] Hui Wang, Zhijian Wu, Shahryar Rahnamayan, Yong Liu, and Mario Ventresca. Enhancing particle swarm optimization using generalized opposition-based learning. *Information sciences*, 181(20):4699–4714, 2011.

[154] Huang Ming, Mingxu Wang, and Xu Liang. An improved genetic algorithm using opposition-based learning for flexible job-shop scheduling problem. In *2016 2nd International Conference on Cloud Computing and Internet of Things (CCIOT)*, pages 8–15. IEEE, 2016.

[155] Wen Long, Jianjun Jiao, Ximing Liang, Shaohong Cai, and Ming Xu. A random opposition-based learning grey wolf optimizer. *IEEE Access*, 7:113810–113825, 2019.

[156] Shahryar Rahnamayan, Hamid R Tizhoosh, and Magdy MA Salama. Quasi-oppositional differential evolution. In *2007 IEEE congress on evolutionary computation*, pages 2229–2236. IEEE, 2007.

[157] Hamdi Tolga Kahraman, Sefa Aras, and Eyüp Gedikli. Fitness-distance balance (FDB): a new selection method for meta-heuristic search algorithms. *Knowledge-Based Systems*, 190:105169, 2020.

[158] Sefa Aras, Eyüp Gedikli, and Hamdi Tolga Kahraman. A novel stochastic fractal search algorithm with fitness-distance balance for global numerical optimization. *Swarm and Evolutionary Computation*, 61:100821, 2021.

[159] Serhat Duman, Hamdi T Kahraman, Ugur Guvenc, and Sefa Aras. Development of a lévy flight and FDB-based coyote optimization algorithm for global optimization and real-world ACOPF problems. *Soft Computing*, 25(8):6577–6617, 2021.

[160] Ugur Guvenc, Serhat Duman, Hamdi Tolga Kahraman, Sefa Aras, and Mehmet Katı. Fitness–distance balance based adaptive guided differential evolution algorithm for security-constrained optimal power flow problem incorporating renewable energy sources. *Applied Soft Computing*, 108:107421, 2021.

[161] Chengcheng Chen, Xianchang Wang, Helong Yu, Mingjing Wang, and Huiling Chen. Dealing with multi-modality using synthesis of moth-flame optimizer with sine cosine mechanisms. *Mathematics and Computers in Simulation*, 188:291–318, 2021.

[162] J Zhang and Jie-Sheng Wang. Improved salp swarm algorithm based on levy flight and sine cosine operator. *IEEE Access*, 8:99740–99771, 2020.

[163] Reem Y Abdelghany, Salah Kamel, Hamdy M Sultan, Ahmed Khorasy, Salah K Elsayed, and Mahrous Ahmed. Development of an improved bonobo optimizer and its application for solar cell parameter estimation. *Sustainability*, 13(7):3863, 2021.

[164] Shalini Shekhawat and Akash Saxena. Development and applications of an intelligent crow search algorithm based on opposition based learning. *ISA transactions*, 99:210–230, 2020.

[165] Selma Yahia, Yassine Meraihi, Amar Ramdane-Cherif, Asma Benmessaoud Gabis, Dalila Acheli, and Hongyu Guan. A survey of channel modeling techniques for visible light communications. *J. Netw. Comput. Appl.*, 194:103206, 2021.

[166] Selma Yahia, Yassine Meraihi, Amar Ramdane-Cherif, Asma Benmessaoud Gabis, and Hossien B Eldeeb. Performance evaluation of vehicular visible light communication based on angle-oriented receiver. *Computer Communications*, 191:500–509, 2022.

[167] Selma Yahia, Yassine Meraihi, Amar Ramdane-Cherif, Tu Dac Ho, and Hossien B Eldeeb. Enhancement of vehicular visible light communication using spherical detector and custom lens combinations. *IEEE Access*, 11:21600–21611, 2023.

[168] Selma Yahia, Yassine Meraihi, Tu Dac Ho, and Hossien B Eldeeb. Performance enhancement of vehicular vlc using spherical detector and efficient lens design. In *2023 IEEE Wireless Communications and Networking Conference (WCNC)*, pages 1–6. IEEE, 2023.